A Comparative Study on A-site and B-site Cobalt Substitution in BaTiO$_3$ Ceramics

M.Sc. Thesis

By
KARTIK

DISCIPLINE OF PHYSICS

INDIAN INSTITUTE OF TECHNOLOGY INDORE

MAY 2025

A Comparative Study on A-site and B-site Cobalt Substitution in BaTiO$_3$ Ceramics

A THESIS

Submitted in partial fulfillment of the requirements for the award of the degree
of
Master of Science

by
KARTIK

DISCIPLINE OF PHYSICS

INDIAN INSTITUTE OF TECHNOLOGY INDORE

MAY 2025

INDIAN INSTITUTE OF TECHNOLOGY INDORE

CANDIDATE'S DECLARATION

I hereby certify that the work which is being presented in the thesis entitled **A Comparative Study on A-site and B-site Cobalt Substitution in BaTiO$_3$ Ceramics** in the partial fulfillment of the requirements for the award of the degree of **MASTER OF SCIENCE** and submitted in the **DISCIPLINE OF PHYSICS, Indian Institute of Technology Indore**, is an authentic record of my own work carried out during the time period from July 2023 to May 2025 under the supervision of **Prof. Somaditya Sen,** Professor, Department of Physics, IIT Indore. The matter presented in this thesis has not been submitted by me for the award of any other degree of this or any other institute.

20/05/2025

Signature of the student with date
KARTIK

This is to certify that the above statement made by the candidate is correct to the best of my knowledge.

Signature of the Supervisor
Prof. Somaditya Sen

KARTIK has successfully given his M.Sc. Oral Examination held on **14 May, 2025.**

Convener, DPGC
Date: 20-05-25

Signature of the Supervisor of
M.Sc. thesis
Prof. Somaditya Sen

ACKNOWLEDGEMENTS

DEDICATED

TO

MY PARENTS,

AND

FRIENDS.

Abstract

The study has been presented with importance of choosing $BaTiO_3$ as an ABO_3 perovskite material and investigates the synthesis and characterization of Cobalt-doped barium titanate ($BaTiO_3$) using the sol-gel method, with Cobalt concentrations of 0%, 3.125%, 6.25%,12.5%, and 25% at A-site and B-site doping. The study begins with an introduction to perovskite materials, followed by an in-depth examination of Barium titanate and its ferroelectric properties. The synthesized samples are characterized using X-ray diffraction (XRD), Scanning Electron Microscopy (SEM), and Raman spectroscopy. XRD analysis is used to identify phase transitions and structural modifications with increasing Cobalt concentration. SEM provides insights into the material's morphology, while Raman spectroscopy explores the local changes in vibrational spectra, due to doping. Additionally, a literature survey on doping in $BaTiO_3$ is included, emphasizing the effects of dopants such as Cobalt on the material's properties and performance. Electrical and magnetic properties are investigated through IV (current-voltage) measurements, B-H loop analysis for magnetic hysteresis behavior, and dielectric measurements. Temperature-dependent dielectric analysis is carried out to understand the thermal stability and phase transitions of the doped material. Furthermore, magnetodielectric measurements are performed to examine the coupling between magnetic and dielectric properties under an applied magnetic field. Focusing on the influence of Cobalt and other dopants on the structural, electrical, and magnetic behavior of the material. This comprehensive study aims to provide a better understanding of the multifunctional characteristics of Cobalt-doped $BaTiO_3$.

TABLE OF CONTENTS

LIST OF FIGURES

LIST OF TABLES

Chapter 1: Introduction

1.1 Understanding Perovskite Materials

1.1.1 Defining Perovskites: General Chemical Formula (ABX$_3$) and Structure

A perovskite is recognized as a crystalline material characterized by a specific chemical formula, ABX$_3$, and a crystal structure similar to that of the mineral perovskite, which is composed of calcium titanium oxide (CaTiO$_3$)[1].
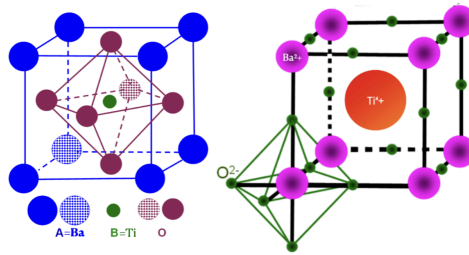
Fig 1.1 ABO$_3$ Crystal Structure

The general chemical formula encompasses two types of positively charged ions, or cations, denoted as A and B, which exhibit a notable difference in their ionic radii. The formula includes a negatively charged ion, or anion, represented by X, which forms chemical bonds with both the A and B cations[2]. While the X anion is most frequently oxygen, it can also consist of other larger ions such as halides, sulfides, or nitrides[4]. Within the broader category of perovskite materials, oxide compounds with the general formula ABO$_3$ constitute a particularly significant class[4].

1.1.2. Historical Context and Discovery

Fig 1.2 a) Mineral Perovskite   b) L. A. Perovski

The journey of understanding perovskite materials began with the discovery of the mineral

perovskite in 1839. This crucial event occurred in the Ural Mountains of Russia, and the mineral was identified by Gustav Rose, who subsequently named it in honor of the distinguished Russian mineralogist, L. A. Perovskia[2]. However, the detailed crystallographic structure that defines this class of materials was not fully explore until much later. In 1926, Victor Goldschmidt provided the first comprehensive description of the perovskite crystal structure[7]. Further significant contributions to the understanding of this structure were made by Helen Dick Megaw, who in 1945 published detailed insights into the atomic arrangements within perovskite materials[8].

1.1.3. Significance and Versatility of Perovskite Materials

Perovskites represent one of the most structurally diverse and abundant families of crystalline materials now[2]. Perovskite oxides have been the subject of extensive research within solid-state physics due to their unique ability to incorporate a significant portion of the metal ions from the periodic table into their crystal lattice[4]. This compositional flexibility is the reason behind their significance in various fields, including electrical ceramics, materials science, particle accelerator technology, and geophysics[4]. Perovskite materials are finding increasing use in advanced technological applications such as random access memories, actuators, tunable microwave devices, displays, piezoelectric devices, transducers, and wireless communication systems[4].

In recent years, halide perovskites have gathered considerable attention, particularly for their exceptional effectiveness in solid-state solar cells[4]. Their potential to revolutionize the photovoltaic industry from their low manufacturing costs, ease of production and remarkably high power conversion efficiencies[5]. Beyond solar energy, perovskite materials are also being utilized in light-emitting diode (LED) technology and showcasing their versatility in optoelectronic applications[5]. Additionally, perovskite quantum dots which are nanocrystalline semiconductors with excellent optical properties have appeared as promising candidates for applications in optoelectronics and nanotechnology, including advanced LED displays and next-generation solar cells[5].

1.2 Fundamental Structure of Perovskites at the Atomic Level

1.2.1 Ideal Cubic Perovskite Structure: A-site, B-site, and X-site Ions

The ideal perovskite structure is usually described as having a cubic symmetry[4]. Within this idealized structure, the larger A cations are positioned at the eight corners of the cubic unit cell[2]. The smaller B cation occupies the center of the unit cell, where it is surrounded by six anions in an

octahedral arrangement exhibiting 6-fold coordination[2]. The X anions, which are typically oxygen atoms in oxide perovskites, are located at the centers of the six faces of the cube[2]. An alternative way to visualize this structure is as a three-dimensional network formed by corner-sharing BX_6 octahedra, with the larger A cations occupy in the interstitial spaces created between these octahedra[2]. In this octahedral representation, the B cation is situated at the center of each octahedron, bonded to the six surrounding X anions[6].

This description of the ideal cubic perovskite structure provides a foundational framework for comprehending the atomic arrangement in these materials. The specific positioning of the A, B, and X ions within the unit cell, along with the resulting coordination environments, plays a crucial role in determining the macroscopic properties of the perovskite material.

1.2.2 Coordination Environments of A and B Cations

In the perovskite structure, the A cation is situated within a cavity formed by the BX_6 octahedra resulting in a 12-fold coordination environment where it is bonded to twelve surrounding anions. This specific arrangement is known as cuboctahedral coordination[2]. Conversely, the B cation located at the center of the BX_6 octahedron exhibits a 6-fold coordination being directly bonded to six anions positioned at the vertices of the octahedron[2].
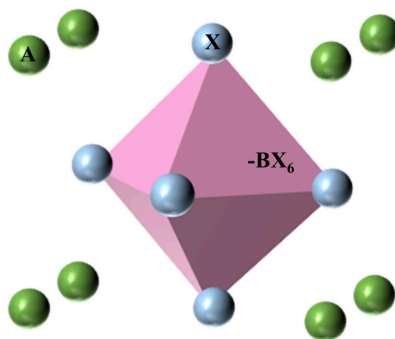
Fig 1.3 Structure of BX_6 Octahedron in ABO_3 Structure

The distinct coordination environments of the A and B cations suggest that these ions fulfill different structural and functional roles within the perovskite lattice. The higher coordination number of the A cation implies that it likely contributes significantly to the overall stability and structural integrity of the perovskite framework. On the other hand, the octahedral coordination of the B cation is associated with the electronic and magnetic properties of the material, particularly when B is a transition metal ion with partially filled d orbitals.

1.2.3 Goldschmidt Tolerance Factor and Structural Stability

The stability of the perovskite crystal structure, especially the ideal cubic form, is highly dependent on the relative sizes of the constituent ions: The A cation, the B cation, and the X anion[2]. An useful empirical parameter for predicting the stability and the likely structural distortions in perovskites is the Goldschmidt tolerance factor (t). It is defined by the relationship

$$t = \frac{r_A + r_X}{\sqrt{2}\left(r_B + r_X\right)}$$

(1.1)

where r_A, r_B, and r_X represent the ionic radii of the A cation, the B cation and the X anion respectively[7]. A wide range of metallic elements can form stable perovskite structures, provided that the calculated Goldschmidt tolerance factor falls within a specific range that lies in 0.75 and 1.0[7]. In an idealized cubic perovskite structure composed of rigid spheres, each cation would ideally be in direct contact with the surrounding oxygen anions, implying a perfect size match and a tolerance factor of 1[10].The Goldschmidt tolerance factor serves as a valuable predictive tool in materials science, allowing researchers to estimate the particular combination of ions forming a perovskite structure and whether that structure is likely to be cubic or distorted. Deviations from the ideal tolerance factor of 1 often indicate that the perovskite structure will exhibit distortions from the perfect cubic symmetry.

1.2.4 Common Structural Distortions: Tetragonal, Orthorhombic, and Rhombohedral Phases

While the ideal cubic perovskite structure provides a fundamental model, it is not the most common form observed in nature or in synthesized materials. In reality, many perovskite materials exhibit structural distortions that result in lower symmetry phases [2]. These deviations from the ideal cubic arrangement frequently lead to the formation of tetragonal, orthorhombic, and rhombohedral crystal structures[2]. Interestingly, even the mineral perovskite ($CaTiO_3$) itself adopts a slightly distorted orthorhombic structure at room temperature [6].

These structural distortions in perovskites can arise from various factors including the relative sizes of the constituent ions, deviations from the ideal stoichiometric ratios and the presence of transition metal ions that exhibit the **Jahn-Teller effect**[6]. One common type of distortion involves the tilting of the BX_6 octahedra within the perovskite lattice. This tilting can occur when the A cation is smaller than the ideal size required for the cubic structure, leading to a reduction in its coordination number

4

from 12 to 8^2. Another significant type of distortion is the off-centering of the B cation within its oxygen octahedron. This phenomenon often occurs when the B cation is smaller than the ideal size for the octahedral site, allowing it to achieve a more stable bonding configuration. The off-center displacement of the B cation results in the creation of an electric dipole moment within the unit cell, which is the fundamental origin of ferroelectric behavior observed in materials like Barium Titanate $(BaTiO_3)^2$. The fact that slight variations in ionic size ratios or other chemical and physical factors can lead to significant structural changes, which can give rise to important functional properties such as ferroelectricity, piezoelectricity, and unique optical behaviors.

1.3 Unique Physical and Chemical Properties Exhibited by Perovskites

1.3.1 Overview of Diverse Properties: Electronic, Optical, Magnetic, Catalytic, etc.

Perovskite materials particularly perovskite oxides are well-known for exhibiting a remarkable diversity of physical and chemical properties[13]. These properties include ferroelectric, dielectric, pyroelectric and piezoelectric behaviors which are crucial for applications in capacitors, sensors and actuators[13]. Furthermore, some perovskites display insulator-metal transitions, ionic conduction characteristics and even superconductivity indicating a wide range of electrical behaviors within this structural family[4]. Beyond these, perovskite materials can also exhibit phenomena such as colossal magnetoresistance where their electrical resistance changes dramatically in the presence of a magnetic field[3].In light-matter interactions, perovskites can possess high optical absorption coefficients, making them excellent candidates for solar energy harvesting. They also exhibit ambipolar charge transfer capabilities, i.e. it can efficiently transport both electrons and holes which is beneficial for various electronic and optoelectronic devices[15]. Lastly, many perovskite oxides possess heterogeneous catalytic activity making them useful in various chemical processes, including environmental remediation and energy conversion[14].

1.3.2 Tunability of Properties through Compositional Variations

The perovskite structure can accommodate significant substitutions at both the A and B cationic sites while generally retaining its fundamental crystal structure[4]. By carefully selecting the specific elements and their ratios at these sites, it is possible to tailor the resulting material's properties to suit a wide range of applications[9]. This compositional flexibility allows for the fine-tuning of magnetic interactions within the perovskite lattice, leading to diverse magnetic phenomena such as ferromagnetism, antiferromagnetism, and magnetoresistance[16]. In two-dimensional perovskites, the optical properties can be effectively controlled by alternating the organic or inorganic layers within

the structure[17]. Even the magnetic properties, including the transition temperatures and the strength of magnetic ordering are highly dependent on the specific elements present at the A and B sites as well as the overall structural ordering within the material[16].

1.3.3 Colossal Magnetoresistance and Superconductivity

The perovskite family of materials exhibits several unique and extraordinary physical phenomena. One such phenomenon is "colossal magnetoresistance", observed in certain perovskites where the material's electrical resistance undergoes an enormous change when exposed to a magnetic field[3]. This property holds significant potential for applications in magnetic storage, sensors and other spintronic devices. Another remarkable phenomenon displayed by some perovskites is superconductivity, the ability to conduct electricity with absolutely no resistance below a critical temperature[3]. The first reported high-temperature superconductor was a perovskite material, Lanthanum Barium Copper Oxide (La-Ba-Cu-O)[15]. Perovskites can exhibit spin-polarized currents and giant magnetoresistance properties that are essential for the development of advanced spintronic devices used in data storage and magnetic sensing[15].

Material	Chemical Formula	Crystal Structure (Room Temp.)	Key Properties	Typical Applications
Calcium Titanate	$CaTiO_3$	Orthorhombic	High dielectric constant, catalytic activity	Dielectrics, catalysts
Strontium Titanate	$SrTiO_3$	Cubic	High dielectric constant, incipient ferroelectric, and photocatalytic	Capacitors, photocatalysts, and substrates for thin films
Lead Titanate	$PbTiO_3$	Tetragonal	Strong ferroelectric, piezoelectric, pyroelectric	Sensors, actuators, transducers, and non-volatile memories
Lanthanum Manganite	$LaMnO_3$	Rhombohedral	Colossal magnetoresistance, magnetic ordering, and catalytic activity	Magnetic sensors, fuel cell cathodes, and catalysts
YBCO	$YBa_2Cu_3O_7$	Orthorhombic	High-temperature superconductor	Superconducting magnets, wires, and electronic devices

Table 1.1: Properties of Common Perovskite Materials

Chapter 2: Project Motivation and Literature survey

Project Motivation

Perovskite materials with their ABX_3 crystal structure are incredibly adaptable. What makes them so interesting is their ability to incorporate a wide range of elements which lets researchers fine-tune their properties for all kinds of applications from electronics to energy systems. Barium Titanate ($BaTiO_3$) is one of the most important materials in this group because of its strong dielectric, ferroelectric, and piezoelectric properties. $BaTiO_3$ is widely used in capacitors because of its high dielectric constant which allows for compact and high-capacity charge storage. Its piezoelectric and pyroelectric responses also make it ideal for sensors and actuators where it detects changes in pressure, temperature, or mechanical motion is crucial. On top of that it's a lead-free material making it a safer and more environmentally friendly alternative to traditional lead-based ferroelectrics. This project looks at one such approach-doping(as a way to enhance its properties). Specifically, Cobalt (Co) is introduced into the $BaTiO_3$ lattice, not just at one site, but at **both the A-site (Ba^{2+})** and the **B-site (Ti^{4+})**. Each site plays a different role in the structure:

A-site doping tends to influence the overall lattice geometry, while B-site doping directly affects the Ti–O octahedra, which are central to the material's ferroelectric behavior. By exploring how Cobalt affects $BaTiO_3$ when substituted at each site, this project aims to draw a clear picture of how dopant location changes the material's structure and functional properties. The broader motivation is to deepen our understanding of how such modifications can lead to improved or even entirely new behaviors in perovskite materials.

2.1 Barium Titanate (BaTiO₃): Structure and Composition

2.1.1 Chemical Formula and Basic Properties of BaTiO₃
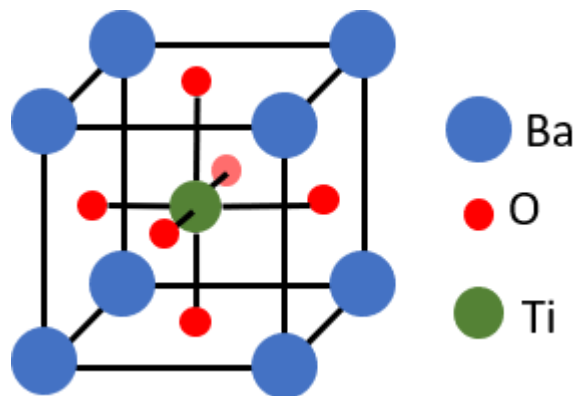
Fig 2.1 Crystal structure of BaTiO₃

Barium Titanate, a widely studied and technologically important material, is chemically represented by the formula $BaTiO_3$[18]. $BaTiO_3$ is classified as an inorganic compound and specifically as the barium salt of metatitanic acid[18]. In its powdered form, Barium Titanate typically appears as a white to gray solid, but it can be processed into large transparent crystals[19]. $BaTiO_3$ exhibits a slight solubility in dilute mineral acids and readily dissolves in concentrated hydrofluoric acid, and it remains insoluble in alkaline solutions and water[18]. In its pure state, Barium Titanate functions as an electrical insulator[19]. However, its electrical conductivity can be significantly altered through doping with specific elements and transforming it into a semiconductor[22]. The material has a density of approximately 6.02 g/cm³ and a high melting point of around 1650 °C[19]. The energy band gap of a Barium Titanate single crystal is about 3.2 eV at room temperature (300 K), but this value can increase to approximately 3.5 eV when the material is in the form of nanoparticles with sizes reduced from about 15 to 7 nm[21].

2.1.2 Crystal Structure of BaTiO₃ Polymorphs

Barium Titanate is known to exist in four distinct crystalline structures, each stable within a specific temperature range: cubic, tetragonal, orthorhombic, and rhombohedral[12]. As the temperature of $BaTiO_3$ decreases, it undergoes a sequence of phase transitions, starting from the high-temperature cubic phase, followed by tetragonal, then orthorhombic, and finally rhombohedral at the lowest temperatures [12]. Ionic radii of Ba^{2+}: 1.35 A, Ti^{4+}: 0.61 A and O_2^{2-}: 1.4 . A respectively from the literature. For BaTiO3, the Ba^{2+} cations are located on the A-sites and Ti^{4+} on the B-sites with eight Ba^{2+} being on the corners at (0 0 0); (0 0 1); (0 1 0); (1 0 0); (1 0 1); (1 1 0); (0 1 1); (1 1 1). In cubic

symmetry, the Ti^{4+} `cations are positioned in the center at` ($\frac{1}{2}$, $\frac{1}{2}$, $\frac{1}{2}$)`, while six` $O-$ anions are at the center of the four faces at (0, $\frac{1}{2}$, $\frac{1}{2}$); ($\frac{1}{2}$, 0,$\frac{1}{2}$); ($\frac{1}{2}$, $\frac{1}{2}$, 0).

The **high-temperature cubic phase** of $BaTiO_3$ is stable above approximately 130 °C (403 K)[12]. In this phase, the crystal structure is based on a regular arrangement of corner-sharing TiO_6 octahedra forming a cubic lattice with the Ba^{2+} ions located at the center of each cube, exhibiting a coordination number of 12 with the surrounding oxygen ions[12]. This cubic phase is centrosymmetric, meaning it lacks a permanent electric dipole moment and it is paraelectric not ferroelectric[12].As the temperature decreases below the Curie temperature (around 120-130 °C), $BaTiO_3$ transitions into the **tetragonal phase** which is stable at room temperature[12]. These phase transitions are generally characterized as discontinuous, or first-order transitions This phase is characterized by a slight distortion of the cubic unit cell along one of its crystallographic axes, resulting in a non-zero electric dipole moment within the unit cell[12]. The tetragonal structure is ferroelectric[12], and belongs to the space group P4mm[21]. The lattice parameters for the tetragonal phase are approximately a = 3.99 nm and c = 4.03 nm[24]. Above the Curie temperature, $BaTiO_3$ loses its spontaneous electric polarization and its ferroelectric properties.
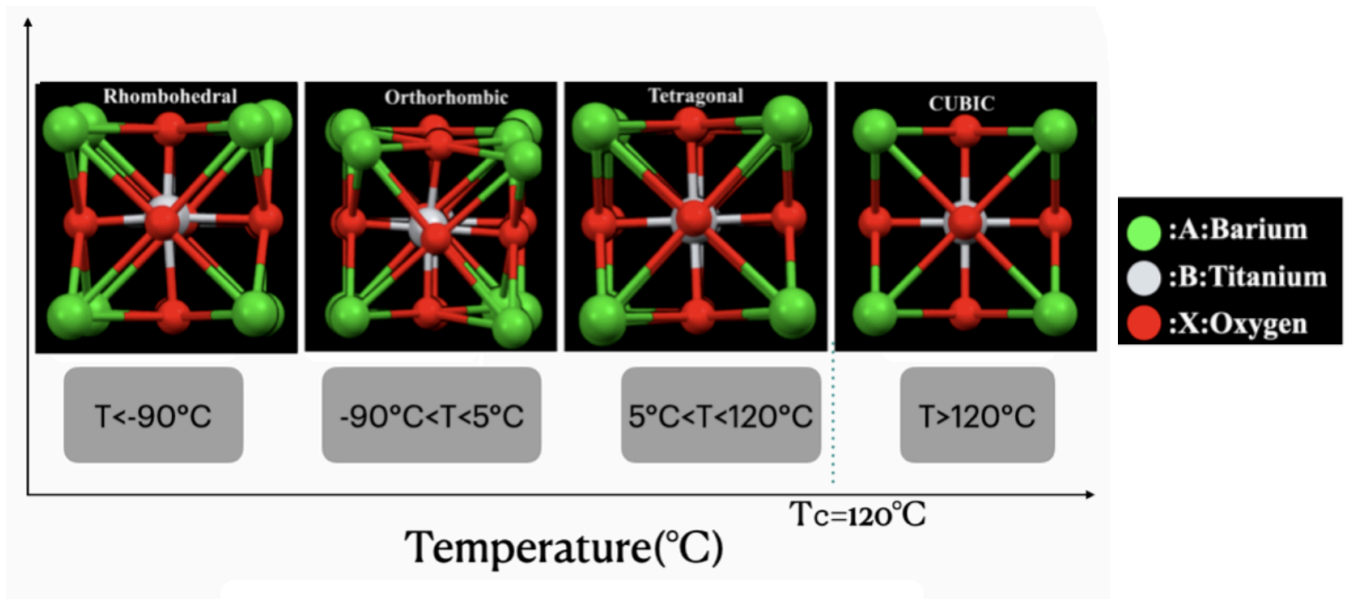
Fig 2.2 Phase transition of $BaTiO_3$ with respect to time

Upon further cooling, Barium Titanate undergoes another phase transition to the **orthorhombic phase**, which is stable below around 5 °C (278 K)[12]. This phase is also ferroelectric but exhibits a more complex arrangement of electric dipoles compared to the tetragonal phase[12]. The orthorhombic phase has a space group of Amm2 [26], with lattice parameters reported as approximately a = 0.6435

nm, b = 0.5306 nm, and c = 0.8854 nm[26]. The **lowest-temperature polymorph** of Barium Titanate is the **rhombohedral phase**, which is stable below approximately -90 °C (183 K)[12]. Similar to the tetragonal and orthorhombic phases, the rhombohedral structure is also ferroelectric and is characterized by a rhombohedral distortion of the unit cell[12]. It belongs to the space group R3m [27], and its cell angle α is approximately 89.87° at 77.4 K[28].The existence of these multiple polymorphs of BaTiO$_3$, each stable within a specific temperature range, is fundamental to its diverse applications. The transitions between these phases involve structural changes at the atomic level that directly impact the material's electrical properties.

Polymorph	Stability Temperature Range (°C)	Crystal Symmetry (Space Group)	Ferroelectric/Paraelectric	Key Structural Features
Cubic	> 130°C	Cubic (Pm3m)	Paraelectric	Regular corner-sharing TiO6 octahedra, Ba at cube center (12-fold coordination)
Tetragonal	5°C to 130°C	Tetragonal (P4mm)	Ferroelectric	Slight distortion of cubic cell along one axis, Ti off-center
Orthorhombic	-90°C to 5°C	Orthorhombic (Amm2)	Ferroelectric	More complex distortion, Ti off-center along face diagonal
Rhombohedral	< -90°C	Rhombohedral (R3m)	Ferroelectric	Rhombohedral distortion of the unit cell, Ti off-center along the body diagonal

Table 2.1: Polymorphs and Transition Temperatures of Barium Titanate (BaTiO$_3$)

In the TiO$_6^{2-}$ octahedron formation, displacement of Ti^{4+} from the center position leads to different phases.In the cubic phase, the Titanium ion is located at the center of oxygen's octahedra. Because of that the crystal field splits the five d-orbitals into two groups (as per crystal field theory):
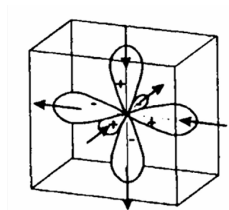
Fig 2.3 d^{2}sp^3 hybridisation of Ti^{4+} ion

Double degenerate e_g (d_{z^2}, $d_{x^2-y^2}$) and triply degenerate t_{2g} (d_{xy}, d_{yz}, and d_{zx}) energy states. E_g having higher energy than t_{2g} because of ligand repulsion through axes. To minimize that energy it hybridizes with 1s and 3p orbitals, forming six equivalent atomic orbitals d^2sp^3 lower than the energy of e_g orbitals. They, together with Oxygen-2p orbitals, form 6σ bonds hence shaping the skeleton of Octahedra [125]. Along with the hybridized orbitals, there are non-bonded t_{2g} orbitals that are available to participate in π-bonding with $2p\pi$ Oxygen orbitals in the direction perpendicular to the O-Ti-O bond. Hence their formation in the structure is favourable and energetically advantageous when Titanium falls off from its centre position. Hence there is a new covalent bond formed in the direction of [001] that leads to the shifting of Titanium along one of the edges and hence transforming the structure from cubic to tetragonal. If there is involvement of two π bonds (any two t_{2g} orbitals), the shifting will be towards one of the face diagonals [011] hence transforming the structure to an orthorhombic phase [124]. Suppose all three orbitals (dxy, dzx, dyz) participate in π bonding. In that case, the titanium starts residing in the energy minima at the body diagonal [111] of the structure, hence transforming the phase into a rhombohedral one.
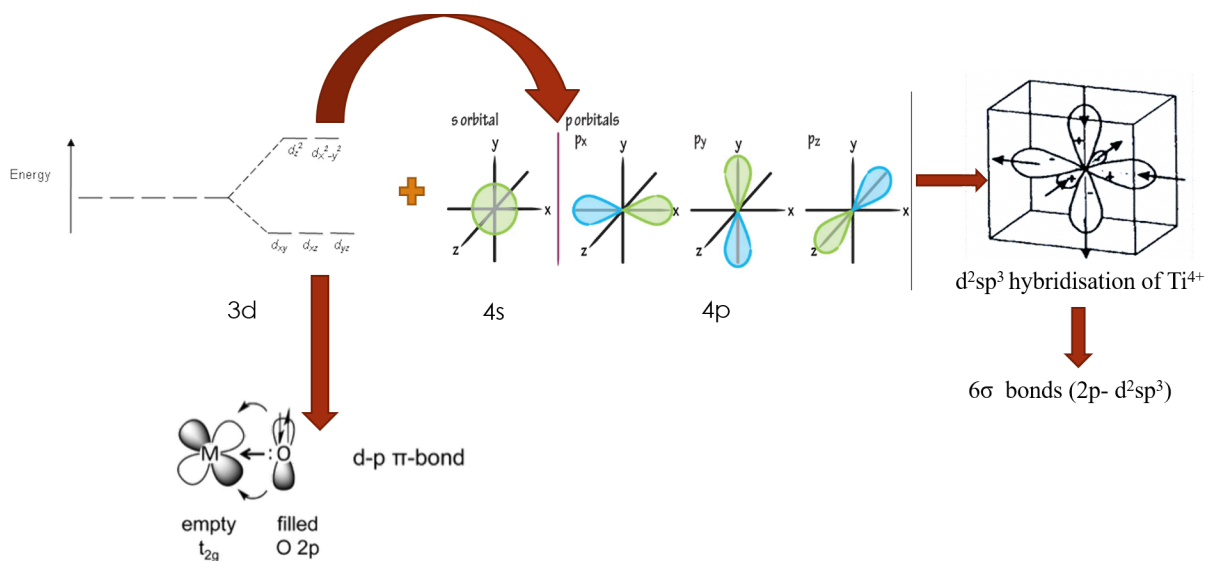
Fig 2.4 Formation of Bond in BaTiO$_3$

dπ-pπ bonding

1π bond → shift towards an edge → tetragonal

2π bonds → shift towards face diagonal → orthorhombic

3π bonds → shift towards body diagonal à rhombohedral

2.1.3 Structural Distortion in Hexagonal BaTiO$_3$

In the hexagonal phase of BaTiO$_3$, which crystallizes in the P6$_3$/mmc space group, the unit cell contains a total of sixteen titanium atoms arranged in two distinct types. Eight of these are corner-sharing Ti atoms and four are edge-sharing Ti atoms referred to as Ti1 (represented in blue), while the remaining four are internal Ti atoms, termed Ti2 (shown in pink). These Ti atoms form two types of TiO$_6$ octahedra, distinguished by their symmetry. The Ti1 atoms form symmetric TiO$_6$ octahedra, characterized by six equivalent Ti–O bond lengths of approximately 1.9905 Å. In contrast, the Ti2 atoms form distorted TiO$_6$ octahedra that are connected by a shared face composed of three oxygen atoms (denoted as O2, shown in red). This face-sharing configuration results in the formation of a dimer, a structural motif commonly found in such hexagonal systems.
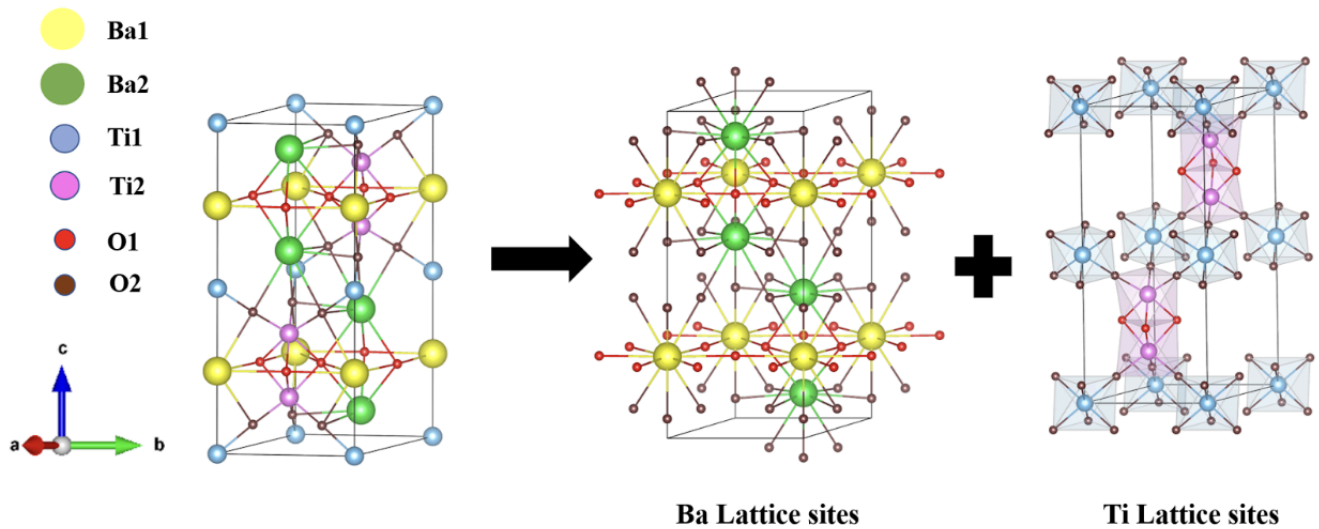
Fig 2.5 Hexagonal Phase of BaTiO$_3$

Within these dimers, the Ti–Ti distance is approximately 2.8 Å, indicative of significant repulsion between the two Ti2 ions. This repulsive interaction causes an elongation of the Ti–O bonds near the shared O3 face of the dimer, leading to a differentiation in bond lengths: each Ti2 atom forms three shorter Ti–O bonds (~1.958 Å) and three longer Ti–O bonds (~1.992 Å). Consequently, the TiO$_6$ octahedra in the dimer are distorted. Moreover, the relative displacement of the Ti2 ions with respect to their surrounding oxygen cages occurs in opposite directions, thereby cancelling out any net dipole moment. As a result, these displacements eliminate the possibility of ferroelectricity in hexagonal BaTiO$_3$ due to Ti ion contributions.

Beyond the octahedral network, the P6₃/mmc structure features a repeating sequence of three Ba–O planes: (Ba2–O1), (Ba1–O2), and again (Ba2–O1). In this arrangement, the Ba2 atoms are displaced from the O1 plane in opposite directions along the c-axis, while Ba1 atoms in two successive Ba1–O2 planes show minimal displacements along the b-axis. The displacement of Ba2 atoms along the c-axis is notably greater than that of Ba1 atoms along the b-axis. Because the displacements of both Ba1 and Ba2 atoms occur in opposing directions across their respective planes, any net polarization is effectively cancelled, thus suppressing the emergence of ferroelectricity from Ba–O layers as well.
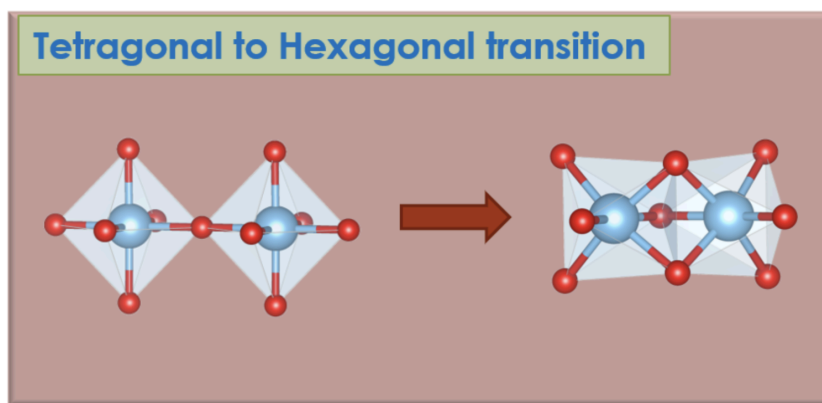
Fig 2.6 Formation of Ti_2O_9 dimer

When cobalt is introduced at the B-site of $BaTiO_3$, it substitutes Ti^{4+} ions with Co^{2+} ions, which have a lower oxidation state. This substitution introduces a charge imbalance within the lattice. To maintain charge neutrality, the crystal responds by forming oxygen vacancies. These vacancies are critical as they disrupt the corner-sharing TiO_6 octahedral framework, which is essential for stabilizing the perovskite phase. The removal of oxygen atoms weakens the three-dimensional connectivity of the TiO_6 network, thereby inducing structural instability.

To compensate for this disruption, the lattice undergoes a local structural rearrangement. In regions with oxygen deficiency, two neighboring Ti-centered octahedra can share a common face, leading to the formation of a Ti_2O_9 dimer. In this dimer, the TiO_6 octahedra are no longer corner-sharing but instead face-sharing, enabling a localized reconstruction that helps counteract the destabilizing effects of oxygen vacancies. Despite the distortions induced by Co doping, this adaptive mechanism allows the crystal to partially preserve its perovskite structure.

2.2 Properties of Barium Titanate (BaTiO$_3$) and Their Origins

2.2.1 Ferroelectric Behavior: Spontaneous Polarization, Curie Temperature, and Domain Structures

The remarkable ferroelectric behavior of Barium Titanate is fundamentally linked to the displacement of the titanium (Ti^{4+}) ion from its central, centrosymmetric position within the oxygen octahedron in its non-cubic crystal structures. This off-center movement of the Ti^{4+} ion creates a permanent electric dipole moment within the unit cell[21]. This spontaneous polarization is a characteristic feature of the tetragonal, orthorhombic, and rhombohedral phases of BaTiO$_3$[21]. Below the Curie temperature, Barium Titanate typically exists in the form of ferroelectric domains. These are microscopic regions within the crystal where the direction of spontaneous polarization is uniform[21]. The arrangement and orientation of these domains can significantly influence the macroscopic properties of the material. By applying a sufficiently strong external electric field, it is possible to align these ferroelectric domains in a preferred direction, a process known as poling[25]. This poling treatment is crucial for enhancing piezoelectric and pyroelectric properties. The magnitude of the spontaneous polarization in BaTiO$_3$ varies depending on the specific crystal phase and can also be affected by factors such as the crystal growth technique and the presence of impurities[21].

Ferroelectric materials particularly those with perovskite structures such as barium titanate (BaTiO$_3$). These materials are characterized by the presence of a spontaneous electric polarization that can be reoriented by an external electric field. This unique feature underpins their usefulness in a wide range of applications, including nonvolatile ferroelectric memories, sensors and actuators. The interest in thin films and ceramics as opposed to single crystals from their ease of fabrication and the possibility of tailoring properties through compositional and structural modifications. The ferroelectric behavior of these materials arises from their intrinsic crystal symmetry and the ability to undergo phase transitions.

Typically, they exhibit a transition from a high-temperature, nonpolar (paraelectric) phase to a low-temperature, polar (ferroelectric) phase. This phase transition is often associated with a change in crystal symmetry, spontaneous strain, and an anomaly in dielectric permittivity, described by the Curie Weiss law (above the Curie temperature). The spontaneous polarization in the ferroelectric phase results in the formation of domain regions within the material where the polarization is uniformly aligned. These domains are separated by domain walls, which may be classified as 180° or non-180° (such as 90°) depending on the relative orientation of polarization vectors across them.

Domain-wall dynamics play a crucial role in determining the macroscopic properties of ferroelectric materials. Under the influence of external electric fields, domain walls can move, contributing to polarization switching and resulting in the characteristic ferroelectric hysteresis loop. This loop illustrates key parameters such as remanent polarization (P_r) and coercive field (E_c), which reflect the material's ability to retain polarization and resist depolarization respectively. In addition to electric fields, domain formation and wall motion are influenced by mechanical stresses and boundary conditions. These factors can induce complex domain structures that optimize the material's electrostatic and elastic energy.The contribution of domain-wall motion to the dielectric and piezoelectric properties is considered an extrinsic effect, distinguishable from the intrinsic response of the lattice. At sub switching field strengths, domain walls can oscillate around their equilibrium positions significantly enhancing the dielectric and piezoelectric responses. However, the presence of defects, such as oxygen vacancies or impurity atoms can resist domain-wall motion, a phenomenon known as pinning. This defect interaction modifies the hysteresis behavior and may lead to phenomena such as aging and internal bias fields in the material. Theoretical modeling of ferroelectric behavior often relies on thermodynamic frameworks like the Landau Ginzburg Devonshire (LGD) theory. This approach uses free energy expansions in terms of polarization and other variables to describe phase transitions, stability conditions, and nonlinear responses under electric, thermal and mechanical loading. For instance the elastic Gibbs free energy formulation is particularly useful for capturing the coupling among polarization, stress, and temperature, an essential aspect for understanding the multifunctional nature of ferroelectric materials.

Moreover, symmetry considerations are fundamental in determining the existence and orientation of polarization and the material's response tensors. Only non centrosymmetric crystal structures can exhibit piezoelectricity and only a subset of these, those with a unique polar axis can display ferroelectric and pyroelectric properties. In ceramics and thin films, grain orientation, texture, and poling processes significantly affect symmetry and macroscopic properties. Ferroelectric materials like $BaTiO_3$ are complex systems whose behavior is governed by a delicate interplay of crystallography, domain physics and defect chemistry. Understanding and manipulating these factors are essential for optimizing their performance in diverse applications and for developing next-generation functional materials.

2.2.2 Piezoelectric Behavior: Piezoelectric Coefficients and Applications

Barium Titanate exhibits piezoelectric behavior in its non-centrosymmetric, ferroelectric phases, namely the tetragonal, orthorhombic, and rhombohedral structures[21]. This property signifies the

material's ability to generate an electrical charge in response to applied mechanical stress and conversely, to produce a mechanical strain when subjected to an electric field[21]. The piezoelectric effect is most pronounced in the tetragonal phase of BaTiO$_3$, which is stable at room temperature[21]. The strength of the piezoelectric effect in a material is quantified by piezoelectric coefficients such as d33, which relates the electrical charge generated per unit of applied mechanical force[30]. For pure polycrystalline BaTiO$_3$, the d33 coefficient is relatively low around 191 pC/N[30]. However, the piezoelectric properties of BaTiO$_3$ can be significantly enhanced through various techniques, including hot isostatic pressing (HIP) which has yielded d33 values up to 172 pC/N, and by doping the material with specific elements like lead (Pb), which can increase the d33 coefficient to 220 pC/N[30]. The piezoelectric properties of Barium Titanate make it suitable for a wide range of applications, including microphones, acoustic emitters, ultrasonic sensors, and various types of actuators[21].

2.2.3 Dielectric Behavior (High Dielectric Constant, Loss Tangent, and Frequency Dependence)

Barium Titanate is particularly well-known for its exceptionally high dielectric constant, which is a measure of its ability to store electrical energy under the influence of an electric field. The dielectric constant of BaTiO$_3$ typically ranges from 1200 to 10,000 at temperatures between 20 and 120°C.[21] Over a narrow temperature range, particularly near its Curie temperature, the dielectric constant can reach even higher values up to 15,000[21]. The dielectric constant of BaTiO$_3$ is not a fixed value but is influenced by several factors, including temperature, the frequency of the applied electric field, the size of the material's particles, the average grain size in polycrystalline samples, and the presence of dopant atoms within its crystal lattice[14]. Another important parameter related to dielectric behavior is the dielectric loss tangent, which represents the energy dissipated as heat in the material when subjected to an alternating electric field. For BaTiO$_3$, the dielectric loss tangent is generally low, especially at temperatures below its Curie temperature. [23]

2.3 Applications of Barium Titanate (BaTiO$_3$)

A.Capacitors

Barium Titanate is an important material in the capacitor industry, primarily due to its remarkably high dielectric constant[20]. This exceptional property allows for the fabrication of capacitors that can store a significant amount of electrical charge in a small volume, a crucial factor in the ongoing trend of miniaturizing electronic devices[20]. BaTiO$_3$ is particularly vital in the production of Multilayer Ceramic Capacitors (MLCCs), which are everywhere in modern electronics.

Material	Dielectric Constant (approximate)	Notes
Air	1	
Polymers (e.g., Teflon)	2 - 3	
Silicon Dioxide	3.9	
Barium Titanate (BaTiO3)	1200 - 10000	Peaks at Curie Temperature
Strontium Titanate (SrTiO3)	~300	
Lead Zirconate Titanate (PZT)	500 - 6000	High performance, but it contains lead

Table 2.2: Comparison of Dielectric Constants of Capacitor Materials

When compared to other dielectric materials commonly used in capacitors, Barium Titanate stands out due to its superior dielectric constant. While polymers and silicon dioxide have relatively low dielectric constants [21], $BaTiO_3$ offers values that are orders of magnitude higher. The increasing demand for lead-free electronics positions Barium Titanate as a critical material for capacitor technology.

B. Sensors

Barium Titanate finds extensive use in various types of sensors, primarily due to its inherent piezoelectric and pyroelectric properties[21]. Its piezoelectric nature, the ability to generate an electrical charge in response to mechanical stress makes it ideal for pressure sensors, acoustic sensors like microphones, and ultrasonic transducers used in applications such as medical imaging and fish finders[21]. Its pyroelectric property, the ability to generate a charge in response to temperature changes makes it suitable for temperature sensors particularly in applications like infrared detectors for thermal imaging[21]. Compared to other materials used in sensor applications, $BaTiO_3$ offers several advantages. For pressure sensing, it provides good sensitivity and a wide operational range[33]. Its

potential for low energy consumption and even self-powered operation, thanks to its photovoltaic effect.

Material	Key Piezoelectric Coefficient (d33, pC/N)	Typical Sensor Applications
Quartz	~2	Pressure sensors, accelerometers
Lead Zirconate Titanate (PZT)	200 - 600	High sensitivity sensors, medical ultrasound
Barium Titanate (BaTiO3)	~190 (pure polycrystalline) up to 220 (doped)	Pressure sensors, acoustic sensors, ultrasonic transducers, and IR detectors
PVDF (Polyvinylidene Fluoride)	-33	Flexible sensors, tactile sensors

Table 2.3: Comparison of Piezoelectric Coefficients of Sensor Materials

C. Actuators

The piezoelectric effect in Barium Titanate is also the key reason for its use in various actuator applications, where electrical energy is converted into precise mechanical motion[21]. These actuators find use in a wide array of devices, including micro-actuators for applications requiring high precision, robotics and automated control systems used in industrial automation[20]. $BaTiO_3$ is also employed in more consumer-oriented applications such as loudspeakers, camera lens autofocus motors, and power windows in automobiles[31]. $BaTiO_3$-based materials can exhibit high strain output under relatively low electric fields, which is a significant advantage for many actuator designs.[31] Certain modified compositions of $BaTiO_3$, such as Barium Calcium Zirconium Titanate (BCZT), have demonstrated piezoelectric properties that are comparable to or even superior to those of soft PZT (Lead Zirconate Titanate), a limitation of $BaTiO_3$ compared to PZT is its lower Curie temperature, which restricts its use in applications that require high-temperature operation.[32]

Material	Key Performance Metric (e.g., d33, strain)	Curie Temperature (°C)	Typical Actuator Applications
Lead Zirconate Titanate (PZT)	High d33, high strain	200 - 490	High force actuators, ultrasonic motors
Barium Titanate (BaTiO3)	Moderate d33 (~190), high strain (modified)	~120-130	Micro-actuators, autofocus motors, and power windows
BCZT	d33 > 600	~100	Promising lead-free alternative to PZT
PMN-PT	Very high d33, giant strain	~150	High-displacement actuators, medical ultrasound transducers

Table 2.4: Performance Comparison of Actuator Material

Chapter 3: Instrumentation and Characterization Techniques

3.1 XRD (X-Ray Diffraction)

System specifications:

Model: Bruker D2 Phaser x-ray diffractometer   **X-ray target:** Cu anode ($K\alpha$ =1.5406 Å)

Max Power: 3 kW **Operating voltage:** 30 kV   **Optics:** Bragg Brentano, Parallel beam

Fig 3.1 XRD (X-Ray Diffractometer) Lab facility

3.1.1 The Basic Principle of X-Ray Diffraction

The phenomenon of X-ray Diffraction is rooted in the interaction of X-rays with the ordered arrangement of atoms in crystalline materials. The process begins with the generation of X-rays, typically within an X-ray tube. In this device, a heated filament emits electrons that are then accelerated under a high voltage towards a target material, often made of copper, molybdenum, chromium, or iron[37]. The impact of these high-energy electrons on the target causes the ejection of core electrons from the target atoms, leading to the emission of X-ray photons with characteristic energies and wavelengths, known as characteristic radiation, such as the Kα and Kβ lines[37]. For XRD experiments, it is crucial to use a monochromatic beam of X-rays, which is usually achieved by employing filters or crystal monochromators to select the Kα radiation[36]. The wavelength of these X-rays on the order of Angstroms (Å), is comparable to the distances between atoms in most crystalline solids[40]. When this monochromatic X-ray beam is directed towards a material, it interacts with the electrons surrounding the atoms in the sample causing them to scatter the X-rays in all

directions through a process known as elastic scattering[41]. Within a crystalline material, the atoms are arranged in a regular, repeating three-dimensional pattern called a crystal lattice. As the incident X-rays penetrate the crystal, they encounter these periodically arranged atoms, which are forced into oscillatory motion by the electromagnetic field of the X-rays. This oscillation results in the emission of secondary X-ray waves that have the same frequency as the incident waves.

The scattered X-rays from the numerous atoms within the crystal then interact with each other. In most directions, these scattered waves are out of phase, leading to destructive interference where the waves cancel each other out. However, in certain specific directions the scattered waves are in phase resulting in constructive interference where the amplitudes of the waves add together producing a strong diffracted beam[41]. The collection of these diffracted beams, as their intensity varies with the scattering angle (2θ), forms the diffraction pattern, which is characteristic of the crystalline structure of the material[40]. The phenomenon of diffraction is fundamentally dependent on the long-range, ordered arrangement of atoms present in crystalline materials. Amorphous materials, which lack this periodic structure, will not produce a well-defined diffraction pattern with sharp peaks. The wavelength of the incident X-rays must be on the same order of magnitude as the interatomic distances within the crystal lattice. This ensures that the X-rays interact strongly with the atoms and are diffracted at angles that can be readily measured by the instrument[40].

3.1.2 Bragg's Law and its Significance in XRD

The condition for constructive interference of X-rays scattered from a crystal lattice is elegantly described by Bragg's Law, which is expressed mathematically as:

$$n\lambda \ = \ 2d\sin\theta \tag{3.1}$$

In this equation, 'n' represents the order of reflection (an integer, typically 1), 'λ' is the wavelength of the incident X-rays, 'd' is the spacing between parallel planes of atoms in the crystal lattice (known as the d-spacing), and 'θ' is the angle of incidence of the X-ray beam with respect to these atomic planes (which is also equal to the angle of reflection).
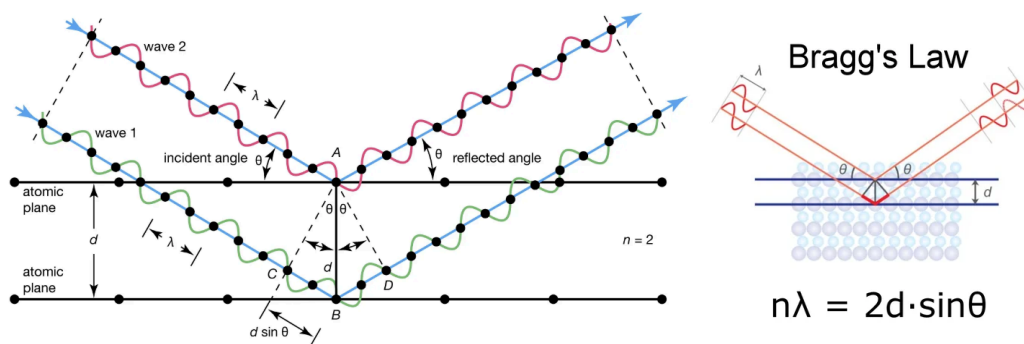
Fig 3.2 Bragg's Law

Bragg's Law establishes a crucial relationship between the wavelength of the incident radiation, the characteristic spacing of the atomic planes within a crystal, and the angles at which the diffracted X-rays are observed. For a given X-ray wavelength, different sets of crystal lattice planes with varying d-spacings will satisfy Bragg's Law at different angles (θ), resulting in a series of diffraction peaks at specific 2θ values (where 2θ is the angle between the incident and diffracted beams)[38].

The significance of Bragg's Law in XRD lies in its fundamental role in determining the crystal structure of materials. Every crystalline material has a unique arrangement of atoms in its lattice, which translates to a unique set of interplanar distances (d-spacings). According to Bragg's Law, this unique set of d-spacings will produce a unique diffraction pattern, with peaks appearing at specific angles. By analyzing the positions (2θ values) of these diffraction peaks, and knowing the wavelength of the X-rays, the d-spacings of the crystal lattice can be calculated using Bragg's Law.

3.1.3 Key Components of an XRD Instrument and Their Functions
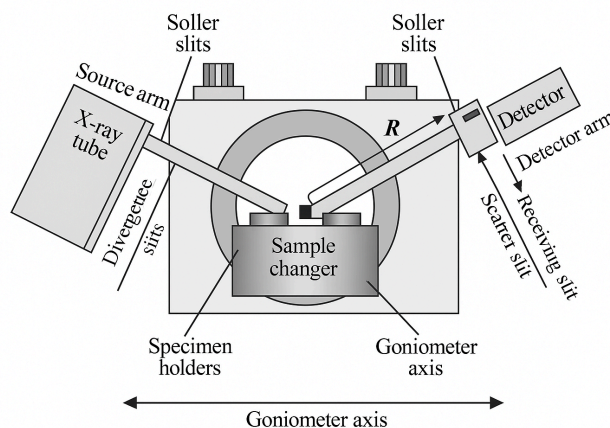
Fig 3.3 Schematic Diagram of XRD Instrument

An X-ray Diffraction (XRD) instrument, also known as an X-ray diffractometer, comprises several key components that work in concert to generate, direct, detect, and analyze the diffracted X-rays from a sample. The three main components are the X-ray source, the sample holder and the X-ray detector[35]. Additionally, ancillary components such as a goniometer, filters, and slits play crucial roles in the process[37].

The X-ray source, typically an X-ray tube, is responsible for generating the X-rays needed for the diffraction experiment[37]. Inside the vacuum tube, electrons produced by heating a filament are accelerated towards a target material. Common target materials include copper (Cu), which is widely used and produces a characteristic X-ray wavelength of 1.5418 Å (Cu Kα radiation). The sample holder provides a stable platform to position the material being analyzed in the path of the X-ray beam[42].

Many sample holders include a mechanism for rotating the sample during the measurement. For powder samples, rotation helps to ensure that all possible orientations of the crystallites are exposed to the X-ray beam, leading to a diffraction pattern that is representative of the entire sample[39]. The goniometer is a precision instrument that controls the angular relationship between the X-ray source, the sample, and the detector[37]. It allows for the accurate measurement of the incident angle (θ) of the X-rays on the sample and the scattering angle (2θ) at which the diffracted X-rays are detected. Two common goniometer geometries are the θ–2θ configuration, where the X-ray source is fixed, the sample rotates by an angle θ, and the detector rotates by 2θ, and the θ–θ configuration where the sample is stationary and both the X-ray source and the detector rotate by an angle θ relative to the sample[37]. The detectors are crucial for recording the intensity of the diffracted X-rays. As the detector moves along the arc corresponding to the diffraction angles (2θ), it measures the number of X-ray photons that constructively interfere at each angle. This data is then processed to generate the diffraction pattern[42].

Component Name	Function	Typical Materials/Types
X-ray Source	Generates X-rays for diffraction.	X-ray tubes with target materials like Copper (Cu), Molybdenum (Mo), Chromium (Cr), Iron (Fe).
Sample Holder	Supports the sample in the X-ray beam's path. May include rotation capabilities.	Various configurations for powders, solids, liquids, thin films.
Goniometer	Controls and measures the angles between the X-ray source, sample, and detector.	θ–2θ geometry (fixed source, rotating sample and detector), θ–θ geometry (fixed sample, rotating source and detector).
Detector	Records the intensity of diffracted X-rays as a function of the diffraction angle.	Proportional counters, Scintillation detectors, Solid-state detectors (Silicon Drift Detectors, pixel detectors).
Filters	Produce monochromatic X-rays by absorbing unwanted wavelengths (e.g., Kβ radiation).	Thin foils (e.g., Nickel filter for Copper radiation).
Slits	Collimate the X-ray beam, reducing divergence and improving resolution.	Metal plates with precisely sized apertures.

Table 3.1: Components of the XRD instrument.

Ancillary components such as filters and slits play important roles in optimizing the quality of the X-ray beam.Filters are used to produce a more monochromatic X-ray beam by absorbing unwanted wavelengths emitted by the X-ray tube[36]. Slits are used to collimate the X-ray beam, reducing its divergence and ensuring that a well-defined, parallel beam strikes the sample. Slits placed before the detector can also help to improve the resolution of the diffraction pattern by limiting the acceptance angle of the detector and reducing the amount of scattered radiation that reaches it[36].

The selection of the X-ray tube's target material is a critical decision that determines the wavelength of the incident X-rays. Different wavelengths are suitable for different types of samples and can provide varying levels of penetration and resolution. For instance, copper radiation is often preferred for general-purpose XRD due to its balance of intensity and wavelength. However, for samples that strongly absorb copper radiation, such as those containing iron using a target material that produces a shorter wavelength like Cobalt or molybdenum might be more advantageous as these wavelengths have higher penetration power[37]. The choice of wavelength also affects the diffraction angles at which peaks appear according to Bragg's Law.

3.1.4 The Process of Generating an XRD Pattern from a Crystalline Material

The generation of an X-ray Diffraction (XRD) pattern from a crystalline material involves a series of steps, starting with the irradiation of the sample with X-rays and culminating in the recording of the diffracted intensities as a function of angle. For polycrystalline materials, which include powders, ceramics, and thin films with a multitude of randomly oriented crystallites, Powder X-ray Diffraction (PXRD) is the most commonly employed technique[37]. The foundation of X-ray diffraction lies in the interaction of X-rays with the crystal lattice. The crystal lattice, with its regular and repeating three-dimensional arrangement of atoms, acts as a diffraction grating for the incident X-rays[38]. Diffraction occurs from the various sets of crystallographic planes that exist within this lattice. These planes are defined by their Miller indices (hkl), a system of notation used to identify the orientation of crystal planes, and each set of planes has a specific interplanar spacing, or d-spacing, which is characteristic of the crystal structure and the orientation of the planes[38].

To obtain the XRD pattern, the detector systematically measures the intensity of the diffracted X-rays as the scattering angle (2θ) is varied. This is typically achieved by rotating the sample and the detector through a defined range of angles while the X-ray source remains fixed or by moving both the source and detector relative to a stationary sample depending on the instrument geometry[37]. The result is an XRD pattern, which is essentially a plot of the intensity of the diffracted X-rays against the scattering

angle (2θ). In this pattern, peaks in intensity occur at specific 2θ angles. Each peak corresponds to the constructive interference of X-rays that have been diffracted by a particular set of crystal lattice planes satisfying Bragg's Law at that angle[37]. The position of the peak (the 2θ value) is related to the d-spacing of the lattice planes, while the intensity of the peak is related to the number of planes contributing to the diffraction and the efficiency of scattering from the atoms in those planes.

The width of the diffraction peaks observed in an XRD pattern provides additional information about the microstructure of the crystalline material. Specifically, the broadening of the peaks is inversely proportional to the average size of the crystallites within the sample. This relationship is mathematically described by the Scherrer equation:

$$ D = \frac{K\lambda}{\beta cos\theta} \tag{3.2} $$

where K is a shape factor (usually around 0.89), λ is the X-ray wavelength, β is the full width at half maximum (FWHM) of the diffraction peak, and θ is the Bragg angle.

3.1.5 Information Obtainable from an XRD Pattern

Phase Identification is one of the most common applications of XRD. Each crystalline phase of a material has a unique arrangement of atoms in its unit cell, which results in a unique set of d-spacings and thus a unique diffraction pattern. This pattern, characterized by the specific angles (2θ values) at which the peaks occur and their relative intensities, serves as a "fingerprint" for that phase. The Lattice Parameters, which are the dimensions of the unit cell, can be calculated with high precision from the XRD peak positions using Bragg's Law and appropriate crystallographic formulas. XRD can be used to estimate the Crystallite Size and Strain in polycrystalline materials. The broadening of the diffraction peaks, beyond that expected from the instrument itself, is related to the size of the individual crystalline domains, or crystallites, within the sample.

3.1.6 Different Types of XRD Techniques and Their Applications

While the fundamental principles of X-ray Diffraction remain the same, various experimental techniques have been developed to cater to different types of samples and specific analytical needs.

Powder XRD (PXRD) is the most common and widely used technique. It is employed for analyzing polycrystalline materials, which include powders, ceramics, and thin films where the individual crystallites are randomly oriented[37]. PXRD provides a comprehensive characterization of the sample,

information about its phase composition, crystal structure, lattice parameters, average crystallite size, and residual strain[37].

Single-Crystal XRD is a more specialized technique designed to determine the complete three-dimensional arrangement of atoms within a single, high-quality crystal[36]. This method requires a crystal of sufficient size and quality to produce a well-resolved diffraction pattern. The crystal is mounted on a goniometer and rotated through various angles to collect a large dataset of diffraction intensities. Analysis of this data allows for the precise determination of bond lengths, bond angles, and the coordinates of all atoms within the unit cell, providing a detailed understanding of the material's atomic structure[36].

Grazing Incidence XRD (GIXRD) is a surface-sensitive technique particularly useful for analyzing thin films, coatings, and near-surface regions of materials. In GIXRD, the incident X-ray beam strikes the sample surface at a very shallow angle, typically less than 1 degree. This grazing incidence geometry enhances the signal obtained from the thin film or surface layer while minimizing the penetration depth of the X-rays into the bulk of the material or the substrate[36]. GIXRD is widely used for characterizing the phase composition, structure, and texture of thin films, as well as for studying surface modifications, interfaces in multilayer structures, and the effects of processing on surface layers[37].

X-Ray Reflectivity (XRR) is another surface-sensitive technique that is employed to determine the thickness, roughness, and electron density of thin films and layered materials. XRR measurements are performed at very low angles of incidence, including the region of total external reflection[36].

The choice of the appropriate XRD technique is fundamentally determined by the nature of the sample under investigation and the specific structural information that is required. Powder XRD serves as a versatile tool for bulk characterization of polycrystalline materials, while single-crystal XRD is essential for unraveling the intricate atomic arrangements in individual crystals. For studying the unique properties of thin films and surfaces, GIXRD and XRR offer specialized capabilities.

Technique Name	Sample Type	Primary Information Obtained	Common Applications
Powder XRD (PXRD)	Polycrystalline powders, ceramics, thin films with random orientation	Phase identification, crystal structure, lattice parameters, crystallite size, strain	Mineral identification, quality control, thin film characterization
Single-Crystal XRD	Single crystals	Detailed atomic arrangement, bond lengths, bond angles, atomic coordinates	Structure determination of new materials, protein crystallography
Grazing Incidence XRD (GIXRD)	Thin films, surface layers	Phase composition, structure, texture of thin films, surface modifications	Characterization of thin film growth, surface analysis
X-ray Reflectivity (XRR)	Thin films, layered structures	Thickness, roughness, density of thin films and layers	Analysis of semiconductor films, coatings, interfaces

Table 3.2: Types of the XRD Techniques.

3.2 Raman Spectroscopy

System specifications:

Model: Horiba-made LabRAM HR Raman spectrometer

Spectral Resolution: 0.9 cm-1

Illumination Source: He-Ne LASER of wavelength 632.8 nm

Detector: CCD detector is used in backscattered mode along with 600 grating

3.2.1 Introduction: Raman Spectroscopy

The fundamental principle underpinning Raman spectroscopy involves the inelastic scattering of monochromatic light, typically originating from a laser source, as it interacts with a sample[43]. When this laser light illuminates a sample the vast majority of the incident photons undergo elastic scattering, a process wherein they retain their original energy and wavelength. This type of scattering is known as Rayleigh scattering[44].
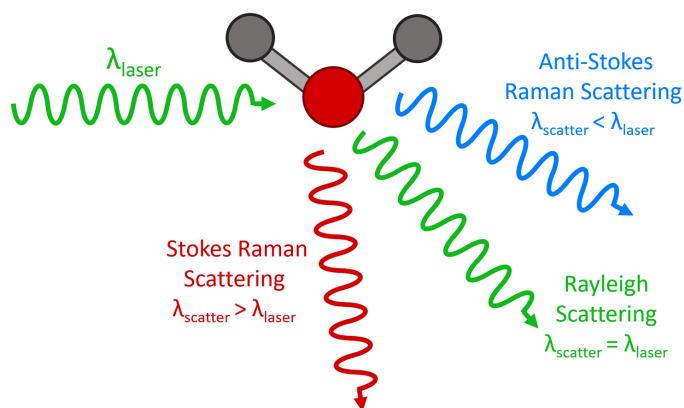
Fig 3.4 Raman Scattering Diagram

However, a very small fraction of the incident photons, typically on the order of one in ten million, experience inelastic scattering. In this interaction, the photons exchange energy with the vibrational energy levels of the molecules within the sample, resulting in a shift in the frequency, and consequently the wavelength and energy, of the scattered light. This phenomenon is termed Raman scattering or the Raman effect[43]. The magnitude of this energy shift is directly correlated with the specific vibrational modes of the molecules present in the sample[43]. A Raman spectrometer is designed to detect this inelastically scattered light and precisely measure its intensity as a function of the frequency shift relative to the incident laser light. The resulting data is then processed and presented as a Raman spectrum, where the appearance of peaks at specific frequency shifts corresponds to the excitation of particular molecular vibrations[44].

3.2.2 The Physics of Light Scattering: Rayleigh vs. Raman

When a beam of light encounters a material, its interaction can manifest in several ways. It might be absorbed by the substance, converting its energy into other forms such as heat. If the material is transparent at the specific wavelength of the light it can be transmitted through it. Alternatively, light can be reflected from the material's surface, or it can be scattered in various directions as it interacts with the constituent atoms and molecules.[8] Raman spectroscopy specifically focuses on the analysis of scattered light, particularly the very weak signals that are scattered at wavelengths that differ from the incident light source[58]. Rayleigh scattering, also known as elastic scattering, represents the most

prevalent mode of light scattering. This phenomenon occurs when an incident photon interacts with a molecule, leading to a temporary polarization of the molecule's electron cloud[49]. In Rayleigh scattering, the molecule almost immediately returns to its original energy state, typically its ground vibrational state, following this brief interaction. The scattered photon is re-emitted with the same energy, and therefore the same frequency and wavelength, as the incident photon[46]. The intensity of Rayleigh scattering exhibits a strong inverse relationship with the fourth power of the incident light's wavelength ($I \propto 1/\lambda^4$).

Raman scattering is an inelastic process[43]. This implies that during the interaction between the incident photon and the molecule, there is an actual transfer of energy between the two entities[43]. The scattered photon emerges with an energy level that is different from that of the incident photon[43]. This difference in energy manifests as a shift in the frequency, and therefore the wavelength and color, of the scattered light when compared to the original laser beam[43]. Raman scattering is a considerably rarer event than Rayleigh scattering, occurring for only a minute fraction of the incident photons, typically around one in ten million[45]. Raman scattering is that the amount of energy gained or lost by the photon corresponds precisely to the energy difference between the vibrational energy levels of the molecule[48]. Raman scattering arises from the interaction of light with the vibrational modes of the molecules present in the sample[56]. The fundamental distinction between Rayleigh and Raman scattering lies in the inelastic nature of the Raman interaction, where energy is exchanged leading to a change in the photon's energy. This energy change is directly linked to the molecule's quantized vibrational energy levels. The phenomenon of Raman scattering is intrinsically linked to the change in the polarizability of a molecule that occurs during its vibrations. When a photon interacts with a molecule, the oscillating electromagnetic field of the photon induces a temporary polarization of the molecule's electron cloud[49]. This polarization results in the creation of a transient induced dipole moment within the molecule[52]. For a specific vibrational mode to be Raman active, meaning it can produce Raman scattering, the molecular polarizability must change as the molecule undergoes that vibration[48]. A Raman transition between two energy states is only permitted if the molecule's polarizability differs between those states[52]. Vibrations that lead to a significant change in the polarizability of the molecule will generally produce stronger Raman signals[57].

Feature	Rayleigh Scattering	Raman Scattering
Energy of Scattered Photon	Same as incident photon	Different from incident photon (higher or lower)
Energy Transfer	No energy transfer to/from the molecule	Energy exchanged with the molecule's vibrational modes
Wavelength	Same as incident light	Different from incident light
Frequency	Same as incident light	Different from incident light
Intensity	Much higher (dominant process)	Much lower (approximately 1 in 10 million photons)
Information	No information about molecular vibrations	Provides information about molecular vibrational energy levels
Mechanism	Elastic scattering, polarization of electron cloud	Inelastic scattering, change in molecular polarizability

Table 3.3: Comparison of Rayleigh and Raman Scattering

3.2.3 Energy Level Transitions and Raman Shift

The atoms within a molecule are in constant motion, vibrating around their equilibrium positions. These vibrations arise from the elastic nature of the chemical bonds that link the atoms, which can be conceptually visualized as springs[43]. Each type of bond within a molecule, and the molecule as a whole, vibrates at specific frequencies that are unique to its composition and structure[43]. These vibrational frequencies are typically expressed in terms of wavenumbers, which are inversely proportional to the wavelength of light and directly proportional to energy[43]. From a quantum mechanical perspective, these molecular vibrations are quantized, meaning they can only exist at specific, discrete energy levels. A molecule cannot possess a continuous range of vibrational energies but can only occupy these allowed energy states[51]. The lowest vibrational energy level is known as the zero-point energy.[24] Raman spectroscopy provides a method to measure the energy difference between

these quantized vibrational energy levels of a molecule[51]. The number of fundamental vibrational modes for a molecule is determined by the number of atoms (N) it contains. For non-linear molecules, the number of vibrational modes is given by the formula (**3N - 6**). For linear molecules, there is one less rotational degree of freedom, resulting in (**3N - 5**) vibrational modes[51].

The process of Raman scattering is often described using the concept of a virtual energy state[50]. When an incident photon interacts with a molecule, it momentarily excites the molecule to a very short-lived, unstable quantum state that is not a true electronic energy level of the molecule. This intermediate state is termed a virtual state[50]. The energy of this virtual state corresponds to the energy of the incident photon plus the initial energy of the molecule, typically in its ground vibrational state. From this virtual state, the molecule almost instantaneously relaxes back to a real vibrational energy level of its ground electronic state, emitting a photon in the process[50]. If the molecule returns to a vibrational level with higher energy than its initial state, the emitted photon will have lower energy (Stokes scattering). Conversely, if the molecule relaxes to a vibrational level with lower energy than its initial state, the emitted photon will have higher energy (anti-Stokes scattering). If the molecule returns to the same vibrational level it started from, the emitted photon will have the same energy (Rayleigh scattering)[50]. The lifetime of the virtual state is extremely short, on the order of 10^{-14} seconds[50]. The concept of the virtual state provides a useful model for understanding how Raman scattering occurs without requiring the incident photon's energy to match a specific electronic transition of the molecule.
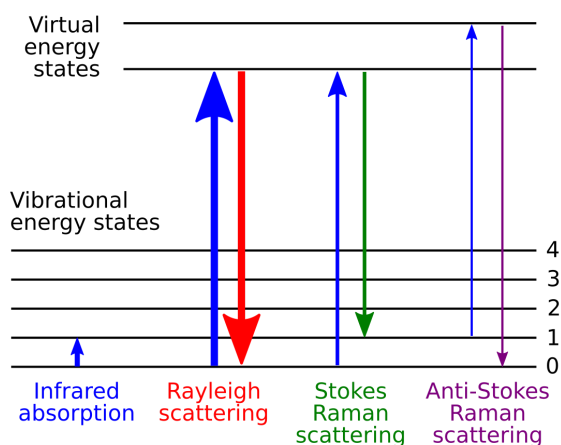
Fig 3.5 Schematic diagram of Raman Scattering

Stokes scattering is the most commonly observed type of Raman scattering[50]. It occurs when the molecule, initially in a lower vibrational energy level (typically the ground state), absorbs energy from the incident photon and is excited to a higher vibrational energy level[48]. In this process, the incident photon loses a portion of its energy, which is transferred to the molecule to induce the vibrational excitation. As a result, the scattered photon has lower energy than the incident photon. According to the relationship.

$$E = \frac{hc}{\lambda} \qquad\qquad (3.3)$$

A lower energy corresponds to a longer wavelength and a lower frequency[48]. This shift to lower energy (longer wavelength) is known as a Stokes shift. Stokes scattering provides direct information about the energy spacing between the ground vibrational state and higher excited vibrational states of the molecule.

Anti-Stokes scattering is a less common type of Raman scattering that occurs when the molecule is initially in a vibrationally excited state and interacts with an incident photon[48]. In this process, the molecule loses energy by relaxing to a lower vibrational energy level (typically the ground state), and this energy is transferred to the incident photon. As a result, the scattered photon has higher energy than the incident photon, corresponding to a shorter wavelength and a higher frequency[48]. This shift to higher energy (shorter wavelength) is known as an anti-Stokes shift.

The Raman shift is the critical parameter in Raman spectroscopy, representing the difference in energy (or frequency/wavenumber) between the incident photon and the Raman scattered photon (whether Stokes or anti-Stokes)[43]. This energy difference is typically expressed in units of wavenumbers, which are directly proportional to the energy difference between the vibrational energy levels involved in the scattering process[51]. The Raman shift ($\Delta\tilde{v}$) can be calculated using the formula:

$$\Delta\tilde{\nu}(\mathrm{cm}^{-1}) = \left(\frac{1}{\lambda_0\,(\mathrm{nm})} - \frac{1}{\lambda_1\,(\mathrm{nm})}\right) \times \frac{(10^7\,\mathrm{nm})}{(\mathrm{cm})}.$$

$$(3.4)$$

where λ_0 is the wavelength of the excitation laser in nm and λ_1 is the wavelength of the Raman scattered light in nm[51]. Alternatively, it can be expressed as the difference in wavenumbers:

$$\Delta\tilde{\nu} = \tilde{\nu}_{laser} - \tilde{\nu}_{scattered} \qquad (3.5)$$

The Rayleigh scattering peak, which has a Raman shift of 0 cm^{-1} (no energy change), is usually very intense and is often filtered out for clarity[44]. Stokes lines appear at positive Raman shifts (lower energy), while anti-Stokes lines appear at negative Raman shifts (higher energy) relative to the laser line[44].

At thermal equilibrium, lower energy levels are more populated than higher energy levels. At typical room temperatures, the vast majority of molecules reside in their ground vibrational state, the lowest energy vibrational level[55]. A smaller fraction of molecules will occupy higher, vibrationally excited states. Since Stokes scattering originates from molecules in the ground vibrational state transitioning to a higher vibrational state, and anti-Stokes scattering originates from molecules already in an excited vibrational state transitioning to a lower state, the intensity of Stokes lines is generally much greater than that of anti-Stokes lines[50]. As temperature increases, the population of higher vibrational energy levels increases, leading to a stronger anti-Stokes signal relative to the Stokes signal. Furthermore, the intensity of the Raman signal for a particular vibrational mode is also directly proportional to the number of those specific chemical bonds or bond types present in the sample[47].

3.2.4 Instrumentation: Components of a Raman Spectrometer
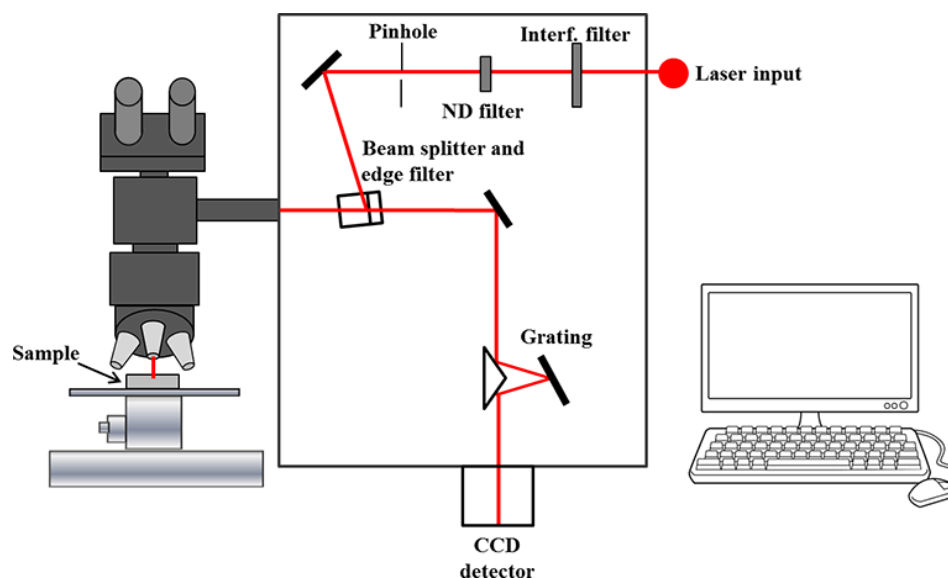
Fig 3.6 Component of Raman Spectroscopy

A Raman spectrometer fundamentally relies on a monochromatic light source with high intensity to initiate Raman scattering.Raman spectroscopy utilizes a range of laser wavelengths across the electromagnetic spectrum, from the ultraviolet (UV) region (e.g., 244 nm) through the visible spectrum (e.g., 532 nm) and into the near-infrared (NIR) region (e.g., 785 nm, 830 nm, 1064 nm)[43]. The intensity of Raman scattering is significantly influenced by the excitation wavelength, exhibiting an inverse fourth power relationship (λ^{-4})[52]. This implies that shorter laser wavelengths, possessing higher photon energies, generally lead to a more intense Raman signal.

A sophisticated system of optics is fundamental to a Raman spectrometer, enabling the precise direction and focusing of the high-intensity laser beam onto the sample and the efficient collection of the relatively weak Raman scattered light for subsequent analysis[53]. A key optical component frequently utilized is a longpass dichroic filter. This specialized filter is designed to reflect the shortwave laser light towards the sample while simultaneously transmitting the longer wavelength Raman scattered light through to the analytical components of the spectrometer[54]. A Raman microscope is employed. This instrument integrates a Raman spectrometer with a conventional optical microscope, enabling high magnification visualization of the sample and subsequent Raman analysis

using a tightly focused, microscopic laser spot[43]. This allows for the analysis of extremely small sample volumes, often in the sub-micron range, and the creation of detailed chemical maps of heterogeneous samples[44]. Raman microscopes utilize high-quality objective lenses to achieve the necessary tight focusing of the laser onto the sample.

The interaction of the laser light with the sample and the generation of scattered light, the collected light stream contains not only the weak Raman scattered light but also the much more intense Rayleigh scattered light, which shares the same wavelength as the excitation laser, and potentially other unwanted light, such as reflected laser light[50]. The most critical component in this stage is a Rayleigh rejection filter, which is specifically designed to block the intense light at the laser wavelength while allowing the Raman scattered light, which has undergone a shift in wavelength, to pass through to the subsequent stages of the spectrometer[50]. These filters typically take the form of notch filters or edge filters. Notch filters exhibit a narrow rejection band centered precisely at the laser wavelength, whereas edge filters possess a sharp spectral cut-off that effectively blocks light below or above a specific wavelength threshold. High-performance filters are essential to achieve high blocking of the Rayleigh line.Once the Raman scattered light has been effectively separated from the dominant Rayleigh scattered light, it needs to undergo further analysis to determine the constituent wavelengths or frequencies, present and their corresponding intensities. This is the primary function of the spectrograph, which acts as a sophisticated wavelength sorting mechanism[49]. The spectrograph lies a dispersion element, which is typically a diffraction grating. A diffraction grating is an optical component featuring a periodic structure that causes incident light to diffract, or bend, at different angles depending on its specific wavelength[50].

The final essential component of a Raman spectrometer is the detector, which is responsible for accurately measuring the intensity of the dispersed Raman scattered light at each specific wavelength[50]. This measurement is then converted into an electrical signal that can be processed and ultimately displayed as the Raman spectrum. Commonly used detectors in Raman spectroscopy include charge-coupled devices (CCDs) and photomultiplier tubes (PMTs)[50]. CCD detectors are particularly favored due to their combination of high sensitivity, low noise characteristics, and the

ability to simultaneously detect a broad range of wavelengths. The detector serves as the crucial interface that transforms the optical signal of the Raman scattered light into a quantifiable electrical signal, which is the fundamental data used to construct the Raman spectrum. High sensitivity and minimal noise are paramount for effectively capturing the weak Raman effect and obtaining high-quality, informative spectra.

Component	Function
Laser Source	Provides a monochromatic, high-intensity light beam to excite the sample.
Sample Illumination Optics	Focuses the laser beam onto the sample.
Collection Optics	Collects the scattered light from the sample.
Rayleigh Rejection Filter	Blocks the intense Rayleigh scattered light while transmitting the Raman scattered light.
Spectrograph	Separates the scattered light into its component wavelengths.
Dispersion Element (Grating)	Disperses the separated light based on wavelength.
Detector	Measures the intensity of the dispersed light at different wavelengths to generate the Raman spectrum.

Table 3.4: Components of a Raman Spectrometer and Their Function

3.3 FE-SEM(Field Effect Scanning Electron Microscopy)

System specifications:

Make: Zeiss   **Model:** Supra 55   **Operating voltage:** $0.02-30$ kV

Working distance: up to 100 nA   **Variable pressure mode:** up to 133 Pa
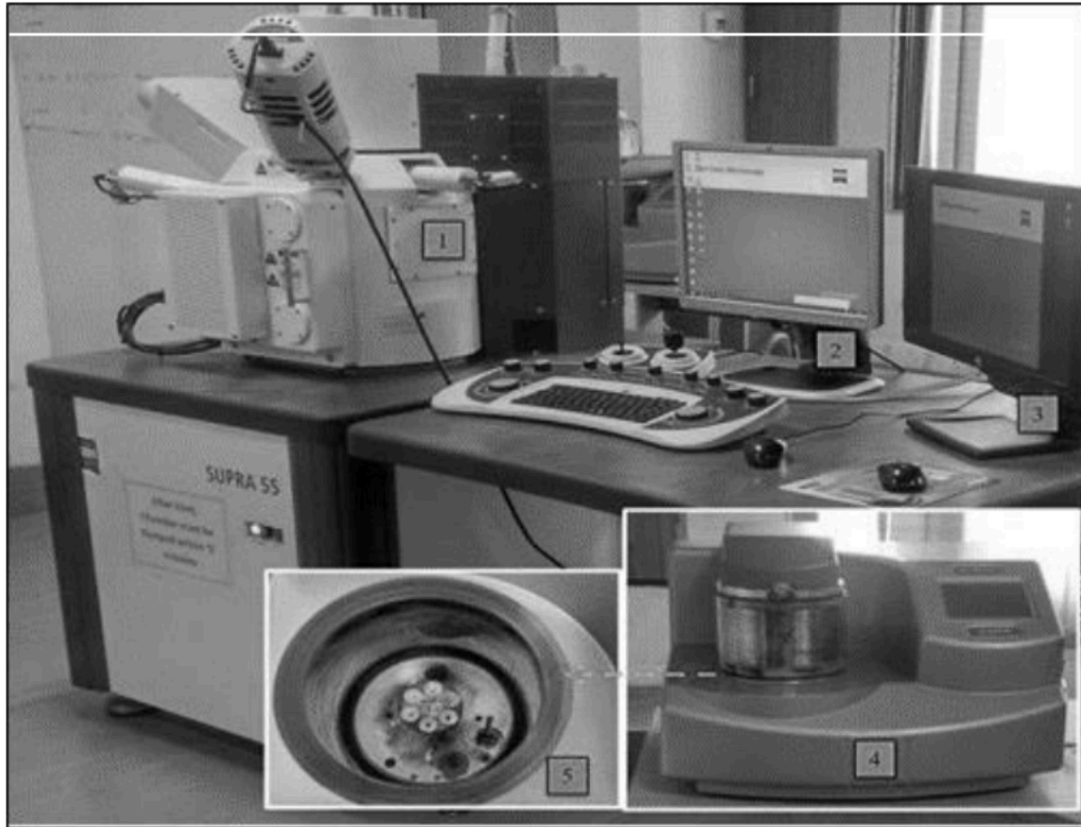
Fig 3.7 FESEM Lab facility

In the Fig.12 **#1** Complete arrangement of the FESEM. **#2** Connected computer systems running user-friendly software. **#3** EDX measurement system. **#4** It is a complete set of gold sputtering. **#5** Enlarged part of the sample holder of the gold sputtering system.

3.3.1 Introduction: What is Field Emission Scanning Electron Microscopy (FESEM)

Scanning Electron Microscopy (SEM) is a powerful and versatile technique employed for obtaining high-resolution, three-dimensional images of the surfaces of solid samples[62]. This is achieved by scanning the sample with a focused beam of electrons. SEM is a non-destructive imaging technique and can be applied to a wide array of materials, including metals, ceramics, polymers, and biological

specimens[62]. Field Emission Scanning Electron Microscopy (FESEM) represents an advanced evolution of the SEM technique, offering significantly higher resolution imaging capabilities[62]. FESEM provides both topographical and elemental information at high magnifications, making it an invaluable tool for detailed surface analysis[66]. The primary distinction between FESEM and conventional SEM lies in the type of electron source used[62]. While conventional SEM typically employs a thermionic electron source, such as a tungsten filament or a lanthanum hexaboride (LaB$_6$) crystal, FESEM utilizes a Field Emission Gun (FEG)[62].

3.3.2 The Principle of Field Emission for Electron Beam Generation in FESEM.
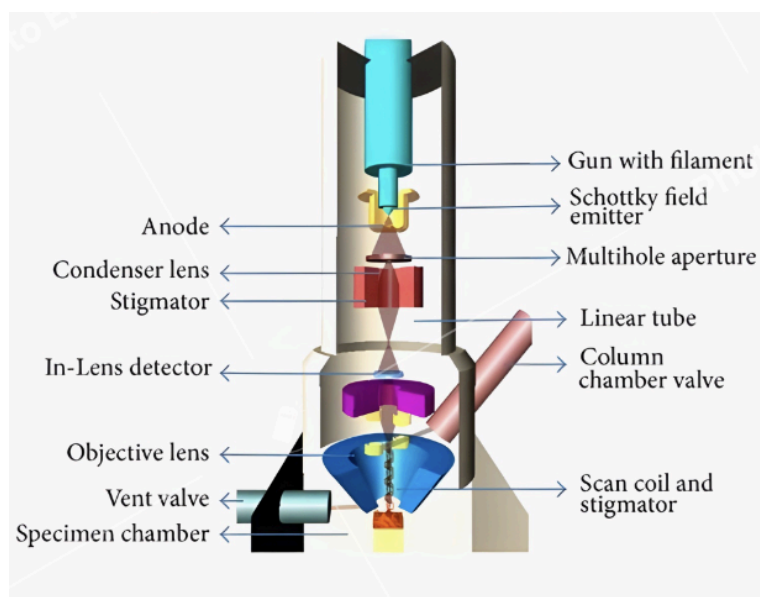
Fig 3.8 Schematic Diagram of a FESEM

In Field Emission Scanning Electron Microscopy (FESEM), electrons are extracted from a typically single-crystal tungsten tip, which serves as the cathode. This process, known as field emission, is driven by the application of a strong electrostatic field at the surface of the emitter tip[65]. Unlike conventional SEMs that rely on thermionic emission, where electrons are released by heating a filament to high temperatures, field emission occurs at or near room temperature. The intense electric field, typically in the order of 2-7 x 10^9 V/m, significantly reduces the width of the potential energy barrier that normally confines electrons within the metal. This quantum mechanical effect allows electrons to tunnel through the narrowed barrier and escape into the vacuum[65]. Different types of FEGs are employed in FESEM, each with its own specific operational characteristics and performance trade-offs. These include Cold Field Emission (CFE) sources, Schottky Emission (SC) sources (also known as Thermal Field Emission - TFE), and Thermal Field Emission (TFE) sources. Cold Field Emission (CFE) sources operate at room

temperature, relying solely on the strong electric field to extract electrons from an extremely sharp tungsten single-crystal tip[67]. Schottky Emission (SC) sources, enhance thermionic emission by applying a strong electric field to a tungsten tip that is coated with a thin layer of zirconium oxide $(ZrO2)$[67]. This coating lowers the work function of the tungsten, allowing for electron emission at lower operating temperatures (around 1800K) compared to conventional thermionic emitters. Thermal Field Emission (TFE) sources also operate at elevated temperatures (around 1800K) to further enhance the stability of electron emission, even under lower vacuum conditions than required by CFEs[67].

3.3.3 Key Components of a FESEM Instrument.
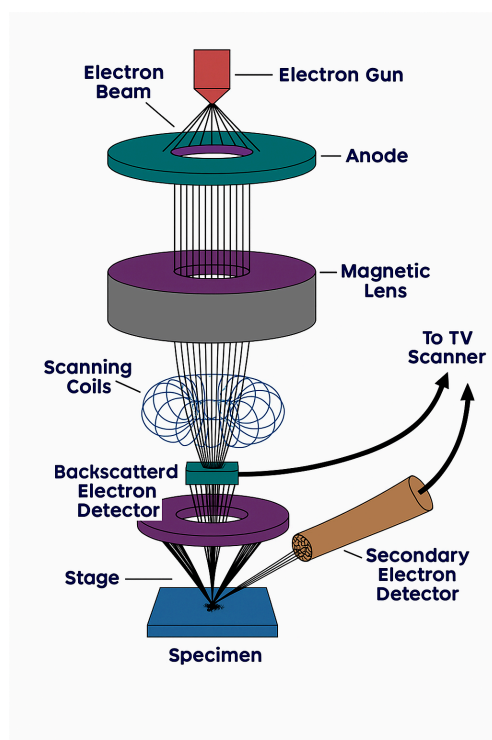
Fig 3.9 Component of FESEM Instrument

A Field Emission Scanning Electron Microscope (FESEM) is a complex instrument comprising several key components that work in concert to produce high-resolution images and analytical data. The heart of the FESEM is the Field Emission Gun (FEG), which serves as the electron source[64]. The FEG generates a stable, high-brightness electron beam by utilizing the principle of field emission[64]. FEG includes an extremely sharp emitter tip, usually made of single-crystal tungsten, an anode positioned close to the tip to create the strong electric field necessary for electron emission, and an acceleration anode that further energizes the emitted electrons to the desired kinetic energy[68]. The entire FEG assembly operates under ultra-high vacuum conditions to maintain the stability and cleanliness of the emitter tip, which is crucial

for ensuring consistent and reliable electron emission[69].

The electron beam generated by the FEG then travels down the Electron Optics Column, a vertical structure that houses a series of electromagnetic lenses and apertures designed to shape, focus, and direct the beam towards the sample[64]. Condenser Lenses, typically electromagnetic coils, are used to initially reduce the diameter of the electron beam and control the amount of electron current (probe current) that reaches the sample[64]. The Objective Lens, located at the bottom of the electron optics column, is the final and most critical lens. It is responsible for focusing the highly demagnified electron beam to an extremely fine spot on the sample surface, which ultimately determines the microscope's resolution.[3] Sample is positioned within the strong magnetic field of the objective lens to minimize optical aberrations and achieve the highest possible resolution[68]. Scan Coils, another set of electromagnetic coils positioned above the objective lens, are used to precisely deflect the electron beam in a raster pattern across the sample surface. This controlled scanning motion enables the point-by-point acquisition of data necessary for forming an image[64]. The Stigmator, consisting of a set of electromagnetic coils, is used to correct for astigmatism, an optical aberration that can cause the electron beam to become elliptical, resulting in a blurred or distorted image[71].

Specimen Chamber, located at the bottom of the electron optics column, is a sealed, high-vacuum enclosure where the sample is placed for examination. Inside the chamber, the specimen is mounted on a Sample Stage, which provides a stable platform and incorporates mechanisms for precise manipulation of the sample in multiple degrees of freedom, including X, Y, and Z translation, as well as rotation and tilt.[3] This allows the user to position the sample optimally relative to the electron beam and detectors and to analyze different areas of interest or view the sample from various angles.Electron Detectors are crucial for capturing the signals generated when the electron beam interacts with the sample[64]. Various types of detectors are strategically positioned within the specimen chamber to collect different types of emitted electrons, providing complementary information about the sample. Secondary Electron Detectors (SED) are used to collect low-energy secondary electrons ejected from the sample surface. These electrons are highly sensitive to surface topography, providing high-resolution images with excellent surface detail and a large depth of field[63]. Backscattered Electron Detectors (BSD) capture high-energy electrons that have been elastically scattered back from the sample. The efficiency of backscattering is strongly dependent on the atomic number of the elements present in the sample. Solid-state detectors, often with a multi-segment design, are commonly used for BSE detection, allowing for the simultaneous acquisition of both compositional and topographical contrast information[72]. FESEMs can be equipped with other specialized detectors, such as Energy Dispersive X-ray

Spectroscopy (EDS) detectors for elemental analysis, which identify and quantify the elemental composition of the sample by detecting the characteristic X-rays emitted when the electron beam bombards the specimen[62].

Vacuum System in a FESEM typically employs a combination of different types of pumps, including rotary pumps for the initial evacuation of the system, turbomolecular pumps for achieving high vacuum levels, and ion getter pumps to maintain the ultra-high vacuum required for the field emission gun to operate effectively[70]. The software receives and processes the signals from the detectors to generate high-resolution digital images, which are displayed on a monitor in real-time. The control and imaging system also provides tools for image analysis, processing, and storage, allowing researchers to extract quantitative data and manage their imaging results.

3.3.4 The Process of Image Formation in FESEM.

Image formation in a Field Emission Scanning Electron Microscope (FESEM) is a sophisticated process that involves a precise sequence of steps. First, a highly focused electron beam, characterized by its small probe size, is generated by the FEG and systematically scanned across the surface of the sample in a controlled raster pattern. This scanning motion is orchestrated by electromagnetic scan coils, which are strategically positioned within the electron optics column to deflect the beam in both the X and Y directions. Finely focused primary electron beam strikes the atoms on the sample's surface, initiating a series of interactions, both elastic and inelastic, leading to the generation of various types of signals[64]. Among these signals, the most commonly detected for the purpose of image formation in FESEM are secondary electrons (SE) and backscattered electrons (BSE).

Secondary Electrons (SE), which are low-energy electrons, are ejected from the sample's surface atoms as a result of inelastic scattering events involving the primary electron beam. FESEMs often incorporate in-lens secondary electron detectors, which are positioned within the objective lens assembly, to maximize the collection efficiency of these low-energy electrons. This arrangement leads to improved image resolution and a better signal-to-noise ratio, particularly when operating the microscope at low accelerating voltages [66]. Backscattered Electrons (BSE), are high-energy electrons that are elastically scattered back from the sample after interacting with the atomic nuclei. The probability of an incident electron being backscattered is strongly dependent on the atomic number (Z) of the elements present in the sample, with heavier elements exhibiting a higher probability of backscattering[72].BSEs are typically detected using solid-state detectors that are positioned above the sample within the specimen chamber. Once the secondary and backscattered electrons are collected by their respective detectors, these

detectors convert the electron signal into an electrical signal[64]. The intensity of the electrical signal at each point scanned on the sample is directly proportional to the number of electrons detected from that specific location. The resulting image is typically rendered in grayscale, where brighter areas correspond to a higher number of detected electrons (indicating a greater signal intensity), and darker areas represent a lower number of detected electrons (indicating a weaker signal intensity).

3.4 Fundamentals of Dielectric Material

3.4.1 Introduction to Dielectric Materials

Dielectric materials constitute a class of electrical insulators distinguished by their capacity to undergo polarization when subjected to an applied electric field[75]. Unlike electrical conductors, where electrons move freely under the influence of an electric field, dielectric materials lack a significant concentration of mobile charge carriers[75]. Their primary function lies in their ability to store electrical energy through the mechanism of electric polarization[77]. This polarization involves a slight shift in the positions of the positive and negative charges within the constituent atoms or molecules of the material in response to the external electric field[76].

The term "dielectric" was first introduced by William Whewell at the behest of Michael Faraday, highlighting its early association with fundamental investigations into electrical phenomena[75]. While the term "insulator" generally denotes a material's capacity to impede the flow of electric current, "dielectric" specifically emphasizes the material's ability to become polarized and thereby store energy within the electric field[75]. The perfect dielectric, is a material possessing zero electrical conductivity, behaving to an ideal capacitor by purely storing and returning electrical energy without any dissipation[75].

3.4.2 Mechanisms of Polarization in Dielectric Materials

When a dielectric material is subjected to an electric field, several microscopic mechanisms can contribute to its overall polarization. These mechanisms, which describe how the internal charge distribution of the material is altered, include electronic polarization, ionic polarization, orientational polarization, and space charge polarization[82]
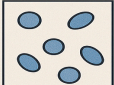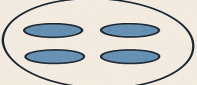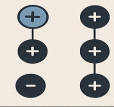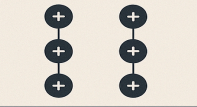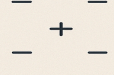
Fig 3.10 Polarization Mechanism

Electronic Polarization

Electronic polarization, also referred to as atomic polarization, is a fundamental phenomenon that occurs in all materials, whether conductive or insulating[78]. This process involves the displacement of the negatively charged electron cloud surrounding an atom relative to its positively charged nucleus under the influence of an external electric field[82]. The applied electric field exerts a force on the electrons and the nucleus in opposite directions due to their opposite charges. This results in a slight separation of the charge centers, creating a tiny induced dipole moment within the atom[80].

Due to the very small mass of electrons, this type of polarization is extremely rapid and can respond to very high frequencies of the applied electric field, typically in the range of 10^{13} to 10^{15} Hz, which corresponds to the frequencies of visible and ultraviolet light[83]. For non-magnetic dielectric materials, Maxwell's electromagnetic theory predicts a relationship between the dielectric constant arising from electronic polarization (ε_r) and the refractive index (n) of the material at very high frequencies, given by $\varepsilon_r = n^2$ [83]. This relationship highlights the connection between the electrical and optical properties of materials. The polarization (P) of a material due to electronic polarization can be quantitatively described by the equation:

$$P = N\alpha_e E = \chi_e \epsilon_0 E \qquad (3.6)$$

where N is the number density of atoms, α_e is the electronic polarizability (a measure of how easily the electron cloud is distorted), E is the applied electric field, χ_e is the electric susceptibility (a measure of how easily the material is polarized), and ε_0 is the permittivity of free space [84].

Ionic Polarization

Ionic polarization is a mechanism that occurs in materials characterized by ionic bonding, such as ionic crystals like sodium chloride (NaCl), potassium chloride (KCl), and lithium bromide (LiBr)[83]. These materials are composed of positively charged cations and negatively charged anions held together by electrostatic forces. In the absence of an external electric field, these ionic structures inherently possess local dipole moments due to the separation of charges between the ions. However, in many ionic crystals, the overall symmetry of the crystal lattice results in a cancellation of these individual dipole moments, leading to no net polarization at the macroscopic level [83]. When an external electric field is applied to an ionic solid, it exerts a force on the ions, causing a slight displacement from their equilibrium positions within the crystal lattice [82]. The cations, being positively charged, are displaced slightly in the direction of the electric field, while the anions, being negatively charged, are displaced in the opposite direction [82]. This relative displacement of the ions, even though small, induces a net dipole moment within the material, leading to ionic polarization. Ionic polarization is generally considered a slower process compared to electronic polarization because it involves the movement of heavier ions rather than just electrons. It typically occurs at frequencies ranging from approximately 10^9 to 10^{13} Hz [83]. The ionic polarizability (α_i), which represents the degree to which the ions are displaced by the electric field. The total polarization (P) due to ionic polarization can be expressed as

$$P = N_i P_{av} = N_i \alpha_i E_{loc} \tag{3.7}$$

where N_i is the number of ion pairs per unit volume, P_{av} is the average dipole moment per ion pair, α_i is the ionic polarizability, and E_{loc} is the local electric field experienced by the ions [84]. Sodium chloride (NaCl) is a classic example of a material that exhibits both electronic and ionic polarization.

Orientational Polarization

Orientational polarization, also known as dipolar polarization, arises in dielectric materials composed of molecules that possess a permanent dipole moment [83]. A permanent dipole moment exists in molecules where there is an inherent asymmetry in the distribution of electric charge, resulting in one end of the

molecule being slightly positive and the other slightly negative, even in the absence of an external electric field [84]. Examples of molecules with permanent dipole moments include water (H_2O), hydrogen chloride (HCl), and ammonia (NH_3).

In a material containing many such polar molecules, these permanent dipoles are typically oriented randomly due to the thermal energy of the molecules, which causes constant random motion [83]. As a result of this random orientation, the individual dipole moments of the molecules cancel each other out, leading to a net polarization of zero in the absence of an external electric field. When an external electric field is applied to the material, these permanent dipoles experience a torque that tends to align them with the direction of the applied field [84]. This alignment is not perfect, as it is constantly disrupted by the thermal agitation of the molecules. The degree of alignment, and therefore the magnitude of the orientational polarization, increases with the strength of the applied electric field and decreases with increasing temperature, as higher temperatures lead to more vigorous thermal motion and greater disorder. Orientational polarization is a relatively slow process compared to electronic and ionic polarization, typically occurring at frequencies below 10^9 Hz. The orientational polarizability (α_o) is inversely proportional to the absolute temperature (T), reflecting the influence of thermal energy on the alignment of dipoles [84].

Space Charge Polarization

Space charge polarization, also known as interfacial polarization or Maxwell-Wagner-Sillars polarization, is a mechanism that arises due to the accumulation of electric charges at interfaces within a dielectric material [82]. These interfaces can occur between different materials in a composite, between crystalline and amorphous regions in a polycrystalline solid, at grain boundaries, at the interface between the dielectric and the electrodes, or even due to the presence of impurities or defects within the material.

When an external electric field is applied, mobile charge carriers (such as ions or electrons) present within the dielectric material can migrate through the bulk. Their movement is often impeded or blocked at these interfaces due to differences in conductivity or the presence of energy barriers[83]. This obstruction leads to a buildup of positive charges on one side of the interface and negative charges on the other side, resulting in the formation of a macroscopic dipole moment and hence, polarization of the material. Unlike electronic, ionic, and orientational polarization, which primarily involve the displacement or reorientation of bound charges, space charge polarization can also involve the movement and accumulation of free charges within the material [84]. Space charge polarization is a very slow process, occurring at extremely low frequencies, typically below 10 Hz [83].

3.4.3 Frequency Dependence of Polarization Mechanisms
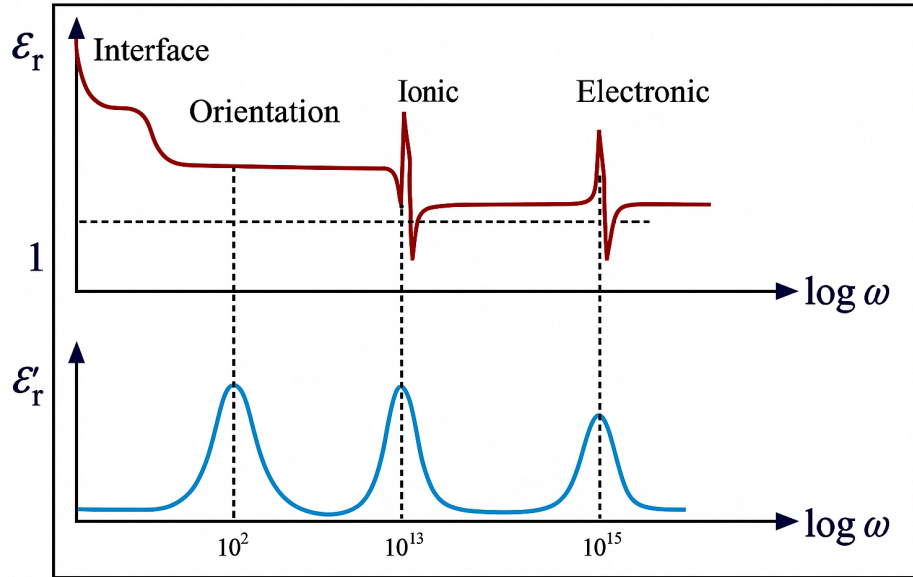
Fig 3.11 Frequency Dependence of Polarization Mechanisms

The contribution of each polarization mechanism to the overall dielectric behavior of a material is strongly dependent on the frequency of the applied electric field [82]. This frequency dependence arises from the fact that each mechanism involves the movement or reorientation of charged entities with different masses and mobilities, and thus different response times.

Electronic polarization, involving the very light electrons, is the fastest mechanism and can follow the oscillations of the electric field up to very high frequencies (10^{13}-10^{15} Hz) [83]. Ionic polarization, which involves the movement of heavier ions, is slower and typically active in the intermediate frequency range (10^9-10^{13} Hz). Orientational polarization, requiring the physical rotation of molecules, is even slower and usually occurs at frequencies below 10^9 Hz. Space charge polarization, involving the relatively long-range migration and accumulation of charges at interfaces, is the slowest mechanism and is significant only at very low frequencies (below 10 Hz)[83].

This frequency dependence allows for the selective excitation and probing of different polarization mechanisms by varying the frequency of the applied electric field. At very high frequencies, only electronic polarization contributes significantly to the dielectric constant. As the frequency is lowered, ionic polarization becomes active, followed by orientational polarization at even lower frequencies. Space charge polarization contributes only at the lowest frequencies.

3.4.4 Dielectric Constant (Relative Permittivity) and Capacitance

The dielectric constant, often denoted by the Greek letter kappa (k) or epsilon with a subscript r (ε_r), is a fundamental property of a dielectric material that quantifies its ability to store electrical energy in an electric field [85]. It is also commonly referred to as the relative permittivity of the material [75].

Defining the Dielectric Constant and its Physical Significance

The dielectric constant can be defined in several equivalent ways. One common definition is the ratio of the capacitance (C) of a capacitor containing the dielectric material between its plates to the capacitance (C_0) of an identical capacitor where the space between the plates is a vacuum [78]. Mathematically, this is expressed as

$$\varepsilon_r = \frac{C}{C_0} \tag{3.8}$$

Permittivity (ε) is a measure of how a material affects an electric field. A higher permittivity indicates that the material more effectively reduces the electric field within it. The dielectric constant (ε_r) is the ratio of the permittivity (ε) of the dielectric material to the permittivity of free space (vacuum), denoted by ε_0 ($\varepsilon_r = \varepsilon/\varepsilon_0$)[78]. The permittivity of free space has a value of approximately 8.854×10^{-12} Farads per meter (F/m). The dielectric constant provides a measure of how much the electric field is reduced inside the dielectric material compared to the field in a vacuum when the same voltage is applied. This reduction in the electric field is due to the polarization of the dielectric material. A higher dielectric constant indicates that the material can become more polarized in response to an applied electric field, leading to a greater reduction in the internal electric field and thus a greater ability to store electrical energy. The dielectric constant is a dimensionless quantity [86].

Mathematical Relationship between Dielectric Constant and Capacitance

The dielectric constant has a direct relationship with the capacitance of a capacitor.

$$C = \varepsilon_r C_o \tag{3.9}$$

where:

- C is the capacitance of the capacitor with the dielectric material.
- ε_r is the dielectric constant (relative permittivity) of the material.

- C_0 is the capacitance of the same capacitor with a vacuum (or air, for practical purposes) between its plates.

For a parallel-plate capacitor, the capacitance without a dielectric is given by

$$C_o = \varepsilon_r \frac{A}{d} \tag{3.10}$$

where A is the area of each plate and d is the distance between the plates. When a dielectric material with a dielectric constant ε_r is inserted to completely fill the space between the plates, the capacitance becomes:

$$C_o = \varepsilon_o \varepsilon_r \frac{A}{d} \tag{3.11}$$

This equation clearly shows that the capacitance of a parallel-plate capacitor is directly proportional to the dielectric constant of the material between the plates, as well as the area of the plates and inversely proportional to the separation distance between them[85].

3.4.5 Dielectric Strength and Voltage Withstanding Capability

Dielectric strength is a critical property of an insulating material that defines its ability to withstand an electric field without experiencing electrical breakdown and becoming conductive. It represents the maximum electric field that the material can endure before its insulating properties are compromised [88]. This property is also known as the breakdown strength of the material.

Defining Dielectric Strength and its Units

Dielectric strength can be defined as the maximum voltage gradient that a material can withstand before electrical breakdown occurs. It is a measure of the inherent electrical strength of the insulating material[88]. Dielectric strength is typically quantified as the maximum voltage required to produce a dielectric breakdown through a material of a given thickness, and it is expressed in units of volts per unit thickness.

Importance of Dielectric Strength in Insulation and Preventing Breakdown

The dielectric strength of an insulating material is of paramount importance in ensuring the safety and reliability of electrical systems, especially those operating at high voltages [88]. It dictates the maximum voltage that can be safely applied across the material without causing it to fail and conduct electricity.

48

Insufficient dielectric strength can lead to various issues, including partial discharges within the insulation, which are localized electrical breakdowns in a small part of the insulation system. These partial discharges can gradually degrade the insulating material over time. In capacitors, the dielectric material not only increases capacitance but also prevents the two conductive plates from coming into direct electrical contact, a function that relies on its dielectric strength. A high dielectric strength reduces the risk of sparking or arcing between the plates, especially under high voltage conditions [89].

Factors Affecting Dielectric Strength

The dielectric strength of a material is not a fixed value but can be influenced by a variety of factors, both intrinsic to the material and extrinsic, such as environmental conditions and testing parameters [88].

It can affect the measured dielectric strength, including the shape and sharpness of the electrodes used, the waveform of the applied voltage (AC or DC), the rate at which the voltage is increased, and the duration for which the voltage stress is maintained. Sharp edges or small radii of curvature on electrodes can lead to a concentration of the electric field, resulting in a lower apparent dielectric strength [88].

Intrinsic properties of the material itself also play a significant role. The chemical composition, the presence of impurities, and the crystalline structure of the material can all influence its dielectric strength [90]. Amorphous materials often exhibit higher dielectric strength compared to their crystalline counterparts due to the absence of grain boundaries. Temperature is another crucial factor. The dielectric strength of most materials tends to decrease as the temperature increases [87]. This is attributed to the increased thermal agitation of the molecules at higher temperatures, which reduces the amount of energy required for electrons to gain sufficient energy to cause an avalanche breakdown. At very high temperatures, thermal breakdown can occur, where the heat generated within the dielectric due to leakage currents exceeds the rate at which it can be dissipated, leading to a rapid rise in temperature and eventual material degradation [91].

The thickness of the material can also have an impact on the dielectric strength. The dielectric strength is inversely proportional to the thickness, meaning that thinner samples may exhibit a higher dielectric strength per unit thickness compared to thicker samples of the same material.Environmental factors such as humidity and atmospheric pressure can also affect dielectric strength. High humidity can lead to an increase in the surface conductivity of the material due to the adsorption of water molecules, which can lower the breakdown voltage.[27]

3.4.6 Types of Dielectric Materials

Dielectric materials can be broadly classified into two main categories based on the polarity of their constituent molecules: polar dielectrics and nonpolar dielectrics.
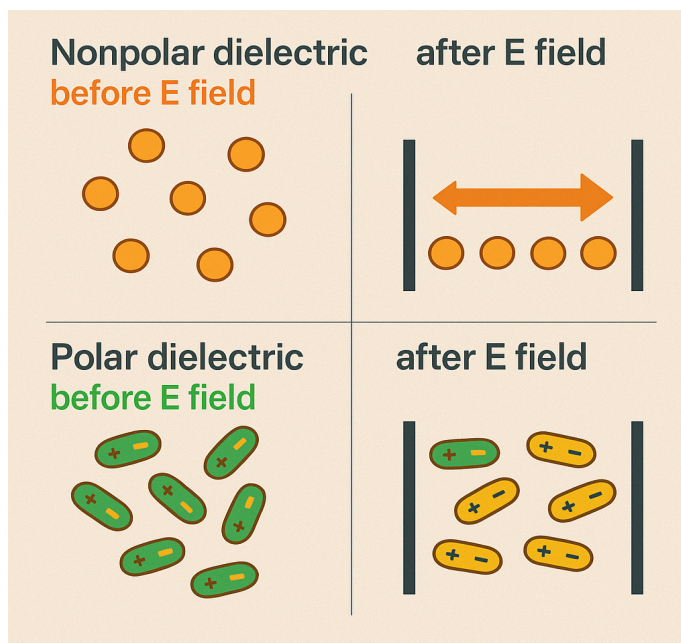

Fig 3.12 Types of Dielectric Materials

Polar Dielectrics

Polar dielectrics are characterized by molecules that possess a permanent dipole moment, meaning there is an inherent separation of positive and negative charges within the molecule even in the absence of an external electric field. These molecules typically have an asymmetric shape that leads to an uneven distribution of charge [92]. Polar dielectrics are polar compounds that do not conduct electricity. When a polar dielectric is placed in an electric field, the permanent dipoles within the molecules experience a torque and tend to align themselves with the direction of the applied field, contributing significantly to the material's polarization, especially at lower frequencies [81].

Nonpolar Dielectrics

Nonpolar dielectrics are composed of molecules that do not have a permanent dipole moment. In these molecules, the distribution of positive and negative charges is symmetric, resulting in no net dipole moment in the absence of an external electric field. Nonpolar molecules typically have a symmetric shape.[28] When a nonpolar dielectric is subjected to an electric field, it induces a temporary dipole moment in the molecules by causing a slight separation of the positive and negative charges, a phenomenon known as electronic polarization [81].

Key Differences Between Polar and Nonpolar Dielectrics

The following table summarizes the key differences between polar and nonpolar dielectrics:

Characteristic	Polar Dielectrics	Nonpolar Dielectrics
Dipole Moment	Permanent	Induced (only in the presence of an electric field)
Molecular Shape	Asymmetric	Symmetric
Polarization	Strong orientational, also electronic and ionic	Primarily electronic
Examples	Water (H_2O), Ammonia (NH_3), HCl	Benzene, Methane, H_2, O_2, N_2

Table 3.5: Difference Between Polar and Non-Polar Dielectrics

3.4.7 Factors Affecting the Dielectric Properties of a Material

The dielectric properties of a material, including its dielectric constant and dielectric strength, are not inherent, fixed values but are influenced by a range of internal and external factors [95].

Temperature

Temperature can have a significant influence on the dielectric properties of a material [87]. The dielectric constant tends to increase with temperature for many materials. This is often attributed to the increased thermal motion of the molecules, which can lead to a greater degree of polarization in response to an applied electric field [87]. Mechanisms like orientational polarization, higher temperatures can increase thermal agitation, making it more difficult for permanent dipoles to align with the electric field, potentially leading to a decrease in the dielectric constant contribution from this mechanism [84]. The

overall temperature dependence of the dielectric constant will therefore depend on which polarization mechanisms are dominant in the material.

Dielectric strength exhibits an inverse relationship with temperature, generally decreasing as the temperature increases[87]. This is because at higher temperatures, the increased thermal energy of the molecules reduces the energy required for electrons to gain enough kinetic energy to cause an avalanche breakdown within the material. At sufficiently high temperatures, a phenomenon known as thermal breakdown can occur, where the heat generated within the dielectric due to leakage currents exceeds the rate at which it can be dissipated, leading to a rapid increase in temperature and ultimately, the degradation or failure of the material [91].

Frequency of the Applied Field

The frequency of the applied electric field is another critical factor that significantly affects the dielectric properties of a material, particularly the dielectric constant and the dielectric loss. The dielectric constant is typically frequency-dependent, often exhibiting higher values at lower frequencies [87]. At lower frequencies, all the polarization mechanisms have sufficient time to contribute to the overall polarization of the material. As the frequency of the applied field increases, the heavier dipoles (those involved in orientational and ionic polarization) may not be able to reorient or displace rapidly enough to keep pace with the oscillating field. This results in a decrease in their contribution to the dielectric constant at higher frequencies [78]. At very high frequencies, only the fast electronic polarization mechanism may remain effective [83]. This frequency-dependent behavior of the permittivity is known as dielectric dispersion. Dielectric loss, which represents the dissipation of energy within the material as heat, generally becomes more pronounced at higher frequencies [94]. The dielectric loss tangent, a measure of this loss, also tends to increase with frequency. This is because at higher frequencies, the polarization processes may lag behind the rapidly changing electric field, leading to energy dissipation through friction-like effects at the molecular level.

Humidity

The presence of moisture in the environment, or the humidity, can significantly affect the dielectric properties of a material, especially its dielectric strength and surface conductivity [91]. Water molecules, being polar, can be adsorbed onto the surface of the dielectric material, forming a thin layer that can increase the surface conductivity [91]. Controlling the humidity and moisture content is often crucial for maintaining the desired dielectric performance of materials in various applications.

3.4.8 Ideal vs Real Dielectrics

Properties of an Ideal Dielectric

An ideal dielectric is a theoretical material that exhibits perfect insulating properties and stores electrical energy without any loss [75]. It would have zero electrical conductivity, meaning no free charges are present to carry current. When an alternating electric field is applied to an ideal dielectric, the polarization within the material would respond instantaneously and perfectly in phase with the field, resulting in a phase difference of exactly 90 degrees between the electric field and the current due to polarization [94]. An ideal dielectric would have a loss angle (δ) of 0 degrees and a loss tangent (tan(δ)) of 0, indicating no dissipation of electromagnetic energy [93]. Such a material would behave like a perfect capacitor, purely storing and returning electrical energy without any conversion to heat or other forms of energy [75]. The response of an ideal dielectric to an electromagnetic field would be purely reactive, with no resistive component.

Dielectric Loss: Explanation of Energy Dissipation in Real Dielectrics

Real dielectric materials inherently exhibit some degree of energy dissipation when subjected to an electromagnetic field, typically in the form of heat [79]. This phenomenon is known as dielectric loss. Dielectric loss in real materials arises because the polarization processes within the material do not respond instantaneously to the applied alternating electric field; there is a certain lag or relaxation time involved [97]. When an AC voltage is applied, the material absorbs some electrical energy, which is then dissipated as heat [98]. Dielectric loss is associated with the resistive components in the material's response to the electromagnetic field, including both the relaxation of bound charges and dipoles, as well as any residual conductivity due to the presence of free charge carriers.

Loss Tangent: Definition and its Significance as a Measure of Dielectric Loss

The dielectric loss in a real material is often quantified using a parameter called the loss tangent, denoted as tan(δ) or D_f, where δ is the loss angle. In the context of a capacitor made with the dielectric material, the loss angle δ represents the angle by which the phase difference between the applied voltage and the resulting current deviates from the ideal 90 degrees [93]. The loss tangent is mathematically defined as the ratio of the imaginary part of the permittivity (ε″), which is associated with energy loss, to the real part of the permittivity (ε′), which is related to energy storage:

$$tan(\delta) \ = \ \frac{\varepsilon''}{\varepsilon'} \qquad\qquad\qquad (3.12)$$

From an electromagnetic field perspective, it can also be expressed as

$$tan\ \delta \ = \ \frac{(\omega\varepsilon'' + \sigma)}{(\omega\varepsilon')} \qquad\qquad\qquad (3.13)$$

where ω is the angular frequency and σ is the conductivity.

The loss tangent is a dimensionless quantity that serves as a measure of the energy dissipation in the dielectric material. A larger value of tan(δ) indicates a greater degree of energy loss, leading to more power consumption and heat generation within the material [94]. The loss tangent is also equivalent to the dissipation factor (DF) and the reciprocal of the quality factor (Q) of a capacitor, where Q is a measure of how efficiently the capacitor stores energy. A low loss tangent is generally desirable for dielectric materials used in applications where energy efficiency is important, such as in high-frequency circuits and energy storage devices.

Factors Contributing to Dielectric Loss

Dielectric loss in real materials arises from several factors at the microscopic level [94]. One major contributor is polarization loss, which occurs due to the relaxation processes of the molecular dipoles within the material. When an alternating electric field is applied, the dipoles attempt to align with the changing field, but their movement is hindered by internal friction or viscosity within the material. This process of polarization and relaxation inevitably consumes electrical energy, which is dissipated as heat[96]. Another source of dielectric loss is conductivity loss, which is associated with the movement of any free charge carriers (such as ions or electrons) present in the dielectric material. Even if the conductivity is very low, any movement of these charge carriers under the influence of the electric field will result in energy dissipation as they overcome the resistance of the material.

3.5 I-V Measurement

3.5.1 Definition and Purpose of I-V Measurement

An I-V measurement, often referred to as a current-voltage characteristic, is the correlation between the voltage applied across an electrical component, device, or material and the resulting current that flows through it [98]. This relationship is visualized as a two-dimensional plot, with the applied voltage represented on the horizontal axis and the measured current on the vertical axis [99]. The fundamental aim of performing an I-V measurement is to gain and understanding of the electrical behavior of the entity under investigation as the voltage conditions are systematically varied [101]. This analysis allows for the determination of critical electrical parameters, such as resistance and conductivity.

3.5.2 Basic Principles (Ohm's Law and the Relationship Between Current and Voltage)

Ohm's law, mathematically expressed as $V = IR$, stands as a basic principle in the study of electricity, defining the relationship between the voltage (V) applied across a conductor, the current (I) flowing through it, and its electrical resistance (R) [102]. This law is particularly applicable to Ohmic materials, where the electrical resistance remains constant regardless of the magnitude or polarity of the applied voltage [100]. When the I-V curve of an Ohmic material is plotted, it results in a straight line that passes through the origin, with the slope of this line being equal to the reciprocal of the resistance (1/R), which is also known as the conductance [100].

3.5.3 Typical Experimental Setup and Instruments Used for I-V Measurements

A more integrated and precise instrument for I-V characterization is the Source Measure Unit (SMU) [99]. An SMU is a versatile device that combines the functionalities of a highly accurate voltage source, a current source, a voltmeter, and an ammeter in a single unit.[2] This integration allows for precise control over either the applied voltage or current and the simultaneous measurement of the other parameter with high accuracy. SMUs are often programmable, enabling automated sweeps of voltage or current to efficiently obtain detailed I-V curves [99]. SMU can be used to measure the current and voltage output of the device as a function of the applied voltage or load [101].

3.5.4 Information Obtained from Analyzing I-V Curves About Material Properties

The graphical representation of an I-V curve serves as a powerful tool for extracting key electrical properties of materials and characterizing the behavior of electronic devices. For materials that obey

Ohm's law, the I-V curve is a straight line passing through the origin. Allowing for a direct determination of the material's resistance (R = V/I) [100]. Once the resistance is known, and if the physical dimensions of the material (length L and cross-sectional area A) are also known, the resistivity (ρ) of the material can be calculated using the relationship :

$$R = \frac{\rho L}{A} \tag{3.14}$$

The conductivity (σ), which is a measure of how well a material conducts electricity, is simply the inverse of the resistivity ($\sigma = 1/\rho$) and can thus be readily obtained from I-V data.

Chapter 4: Results And Discussion

4.1 Synthesis method

Fig 4.1 Sol-Gel Synthesis Process

The synthesis of Cobalt-doped $BaTiO_3$ at both A-site ($Ba_{1-x}Co_xTiO_3$) and B-site ($BaTi_{1-x}Co_xO_3$) was performed using a sol-gel method because it provides better control over the reaction and enables the production of high-purity samples, with dopant concentrations of 0%, 3.125%, 6.25%, 12.5%, and 25% for A-site doping and 0%, 3.125%, 6.25%, 12.5% and 25% for B-site doping. The calculations were based on a target mass of 5 moles, considering the molecular weights of $Ba(NO_3)_2$, $Co(NO_3)_2 \cdot 6H_2O$, and titanium precursor (TALH), ensuring precise stoichiometric ratios. Citric acid and ethylene glycol were used as chelating and polymerizing agents to enhance homogeneity. The precursor solutions were stirred at 80°C to form a stable sol, which was then heated to 100°C to form a gel, followed by drying at 120°C and pre-calcination at 450°C to remove organic residues. The final calcination at 1250°C ensured crystallization, with different doping levels influencing phase formation, as evident in the structural analysis. The selection of specific dopant concentrations was based on solubility limits and expected structural modifications. For dielectric and electrical measurements, pellets were prepared from the synthesized samples. The calcined powders were grind thoroughly with polyvinyl alcohol (PVA), which served as a binder to pellet formation. Approximately 0.5 g of the powder mixture was used to make each pellet using a hydraulic press in a 10 mm die set. All these pellets were then heated at 450°C for 3 hours to remove the PVA binder, whose boiling point is below 400°C. After binder removal, the pellets were sintered at 1250°C for 3 hours.Then silver paste was applied to both surfaces of the sintered pellets to serve as electrodes for dielectric and electrical characterization.
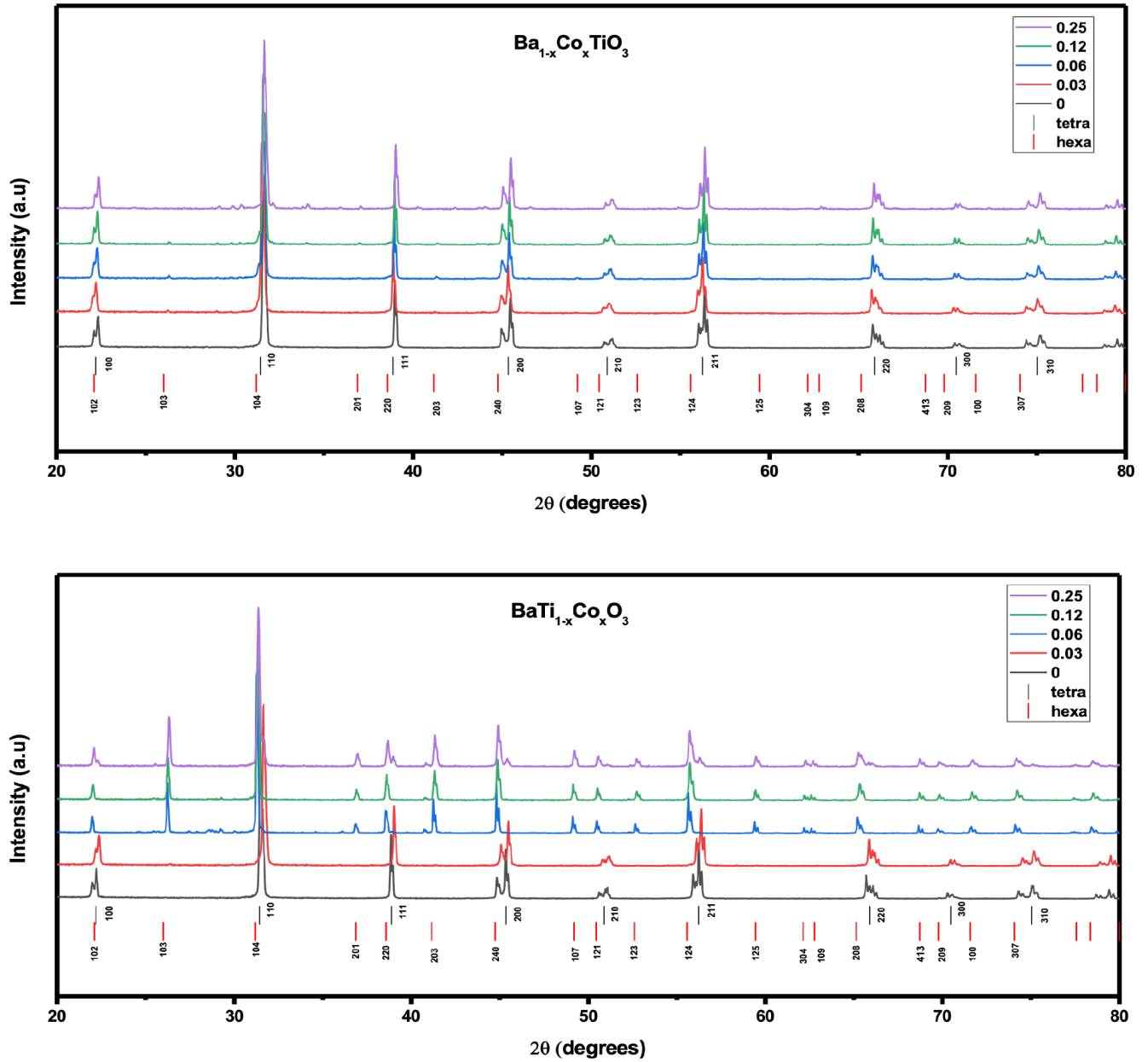
4.2 XRD analysis

Fig 4.2 XRD measurement of Cobalt Doped BaTiO₃ a)A-site (Ba₁₋ₓCoₓTiO₃) b)B-site (BaTi₁₋ₓCoₓO₃)

The X-ray diffraction (XRD) analysis of Cobalt-doped BaTiO₃ at both the A-site (Ba₁₋ₓCoₓTiO₃) and B-site (BaTi₁₋ₓCoₓO₃) reveals distinct structural modifications depending on the dopant concentration and there doping site. In the case of A-site doping, all samples retained their tetragonal structure(space group *P4mm*), impurity phases increased with higher doping concentrations. While the pure BaTiO₃ sample exhibited a single-phase tetragonal structure, minor impurity peaks emerged at 3%, 6%, and

12% doping levels and became more pronounced at 25% doping with no signs of a hexagonal phase. The characteristic peak splitting near $2\theta \approx 45°$ corresponding to the (002)/(200) shows the presence of tetragonal phase in the A-site Cobalt doped Barium Titanate.At high doping levels Cobalt substitution at the A-site ($Ba_{1-x}Co_xTiO_3$) the XRD patterns show a growing number of extra peaks that do not correspond to the primary tetragonal $BaTiO_3$ structure. These are impurity peaks. The tetragonal structure remains the dominant phase, but the increased presence of impurities peaks implies that the lattice has reached its solubility limit for Cobalt ions which means it can't incorporate them into the crystal structure without forming secondary phases. In the B-site doping shows a clear tetragonal-to-hexagonal phase transition as doping increases. The undoped $BaTiO_3$ and the 3.125% doped sample retained the tetragonal P4mm phase, with peak splitting at (002) and (101) slightly reduced, indicating minimal lattice distortion.At 6.25% doping, the emergence of a peak near $2\theta \sim 38°$, corresponding to the (102) reflection of the hexagonal phase, marked the onset of a tetragonal-to-hexagonal phase transition. This transformation became more pronounced at 12.5% doping, where the hexagonal phase dominated, and the absence of tetragonal peak splitting confirmed the structural instability of the ferroelectric tetragonal phase at higher Cobalt concentrations.This transition occurs due to Cobalt ions (Co^{2+}/Co^{3+}) replacing Ti^{4+} at the B-site, introducing lattice strain that destabilizes the ferroelectric tetragonal phase.
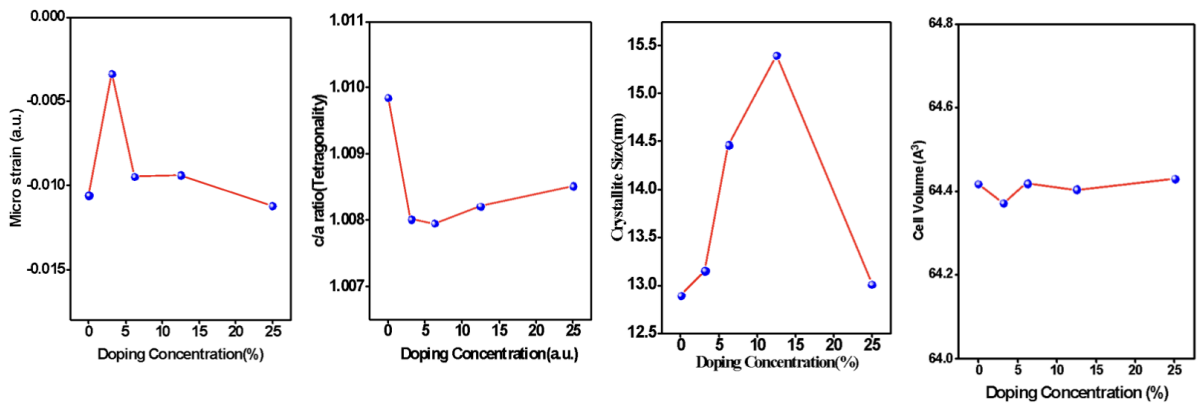

Fig 4.3 Structural Parameter Trends in A-Site Co-Doped BaTiO$_3$

The structural parameters of Cobalt-doped $BaTiO_3$ at the A-site ($Ba_{1-x}Co_xTiO_3$) exhibit variations with increasing Co concentration, indicating a strong influence of doping on the crystal lattice. The microstrain shows a sharp increase at 3.125% Co doping, reflecting significant lattice distortion due to the substitution of larger Ba^{2+} ions with smaller Co^{2+} ions. As the doping level increases, the microstrain decreases due to the formation of impurities or secondary phase. The crystallite size increases with Co doping up to 12.5%, suggesting improved crystallization or grain growth possibly facilitated by

enhanced sintering. At 25% doping, a decline in crystallite size is observed, which may be destabilization of the tetragonal structure and the presence of impurity phases inhibiting grain growth. Cell volume exhibits a non-steady trend, with slight fluctuations that could result from effects of ionic substitution or lattice strain. The c/a ratio, which shows tetragonality, drops sharply at low doping levels, indicating a reduction in ferroelectric distortion and a tendency toward cubic symmetry. A slight increase in c/a at higher doping levels may indicate some partial recovery of distortion. Overall, these trends confirm that A-site Cobalt doping introduces significant structural modifications, with optimal crystallinity at moderate doping levels and signs of lattice destabilization and impurity formation at higher concentrations.
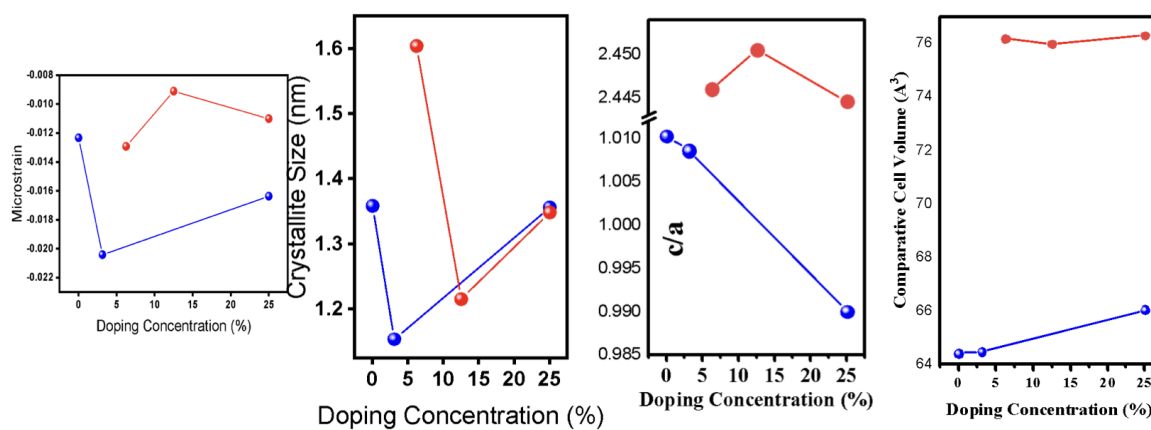

Fig 4.4 Structural Parameter Trends in B-Site Co-Doped BaTiO$_3$

The structural parameters of Cobalt-doped BaTiO$_3$ at the B-site (BaTi$_{1-x}$Co$_x$O$_3$) reveal a more noticeable response to doping compared to A-site substitution. The microstrain initially decreases at 3.125% doping, showing lattice distortion due to the substitution of smaller Ti^{4+} ions (0.605 Å) with slightly larger Co^{2+}/Co^{3+} ions (~0.65–0.75 Å), then relaxes steadily at 12.5% doping concentrations possibly due to the formation of secondary phases and reordering of the lattice. Crystallite size shows a non-steady trend, decreasing at low doping, peaking at 6.25%, and then dropping again indicating that moderate doping supports crystal growth, while higher doping disrupts it. A noticeable change is seen in the cell volume and c/a ratio at 6.25% doping, where both parameters exhibit a sudden jump. This indicates a tetragonal-to-hexagonal phase transition agreeing with the XRD analysis, indicating structural transformation induced by increased Co content. The sharp rise in c/a ratio from ~1.0 to ~2.45 confirms a change in crystal symmetry. Thus indicate that B-site Co doping significantly destabilizes the original tetragonal structure and promotes phase transformation at relatively lower doping levels compared to A-site doping of BaTiO$_3$.
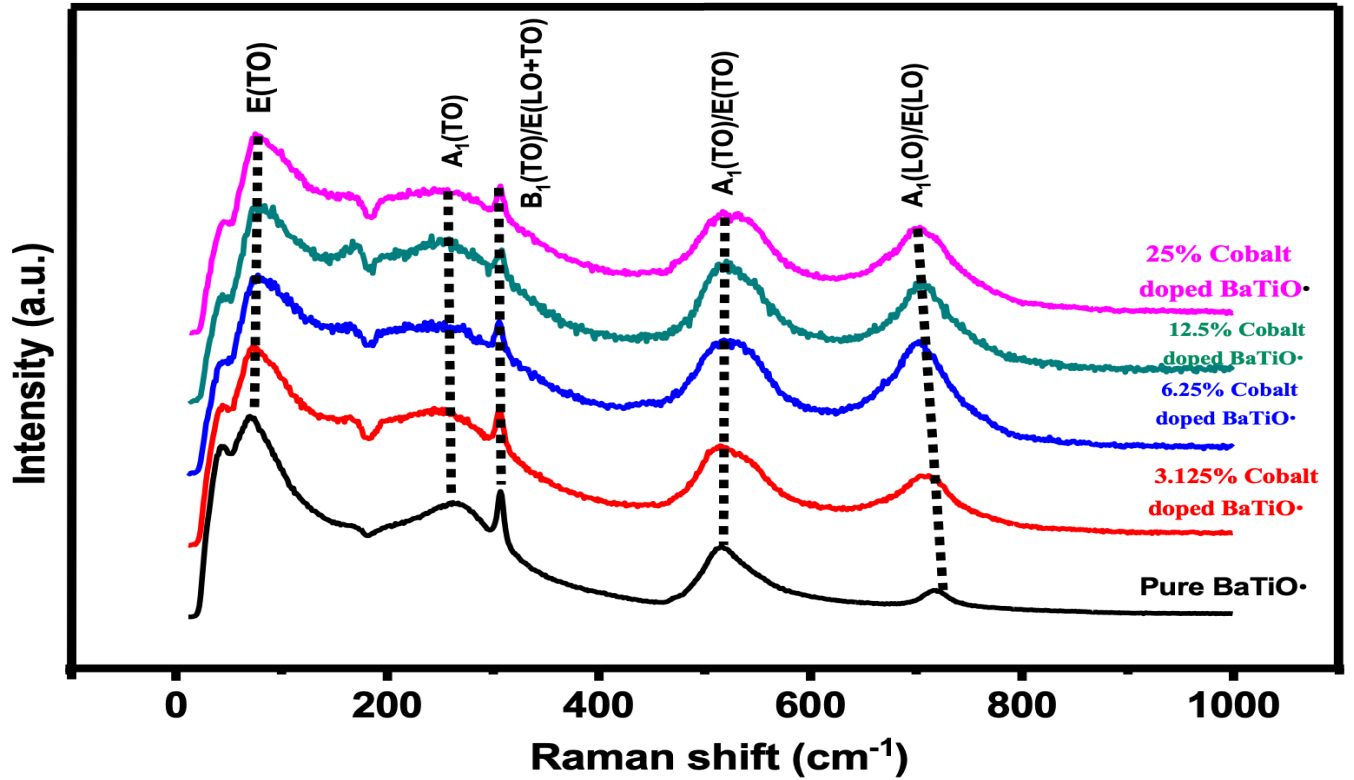
4.3 RAMAN analysis

A-siteCobalt doped BaTiO$_3$

Fig 22. Raman spectra of Cobalt Doped A-site BaTiO$_3$ (Ba$_{1-x}$Co$_x$TiO$_3$)

The Raman spectra of A-site Cobalt-doped BaTiO$_3$ (Ba$_{1-x}$Co$_x$TiO$_3$) reveal systematic changes in vibrational modes with increasing Co concentration, as shown in the figure. The undoped BaTiO$_3$ exhibits well-defined peaks at characteristic Raman shifts corresponding to the tetragonal P4mm phase, including E(TO) (~100 cm^{-1}), A$_1$(TO) (~260 cm^{-1}), B$_1$(TO)/E(LO+TO) (~515 cm^{-1}), and A$_1$(LO)/E(LO) (~720 cm^{-1}). Specifically, the E(TO) mode near 200 cm^{-1} corresponds to oxygen vibrations within the tetragonal phase, while the A$_1$(TO) mode around 520 cm^{-1} is attributed to Ti–O bond vibrations. Additionally, the A$_1$(LO)/E(LO) mode near 720 cm^{-1} signifies strong polar interactions characteristic of the tetragonal ferroelectric phase. As the Co doping concentration increases, peak broadening and intensity reduction are observed, which may indicate increased lattice disorder due to substitutional doping at the A-site. At lower doping concentrations (3.125% and 6.25%), the Raman spectra retain the main tetragonal vibrational features, though slight peak shifts and broadening suggest minor structural distortions. At higher doping levels (12.5% and 25%), the peaks become increasingly diffused, with a more pronounced reduction in intensity. No new peaks corresponding to secondary phases or

significant changes indicative of a phase transition to hexagonal symmetry are observed, confirming the existence of the tetragonal structure. These results align with XRD findings, which showed impurity formation but no complete structural transformation.
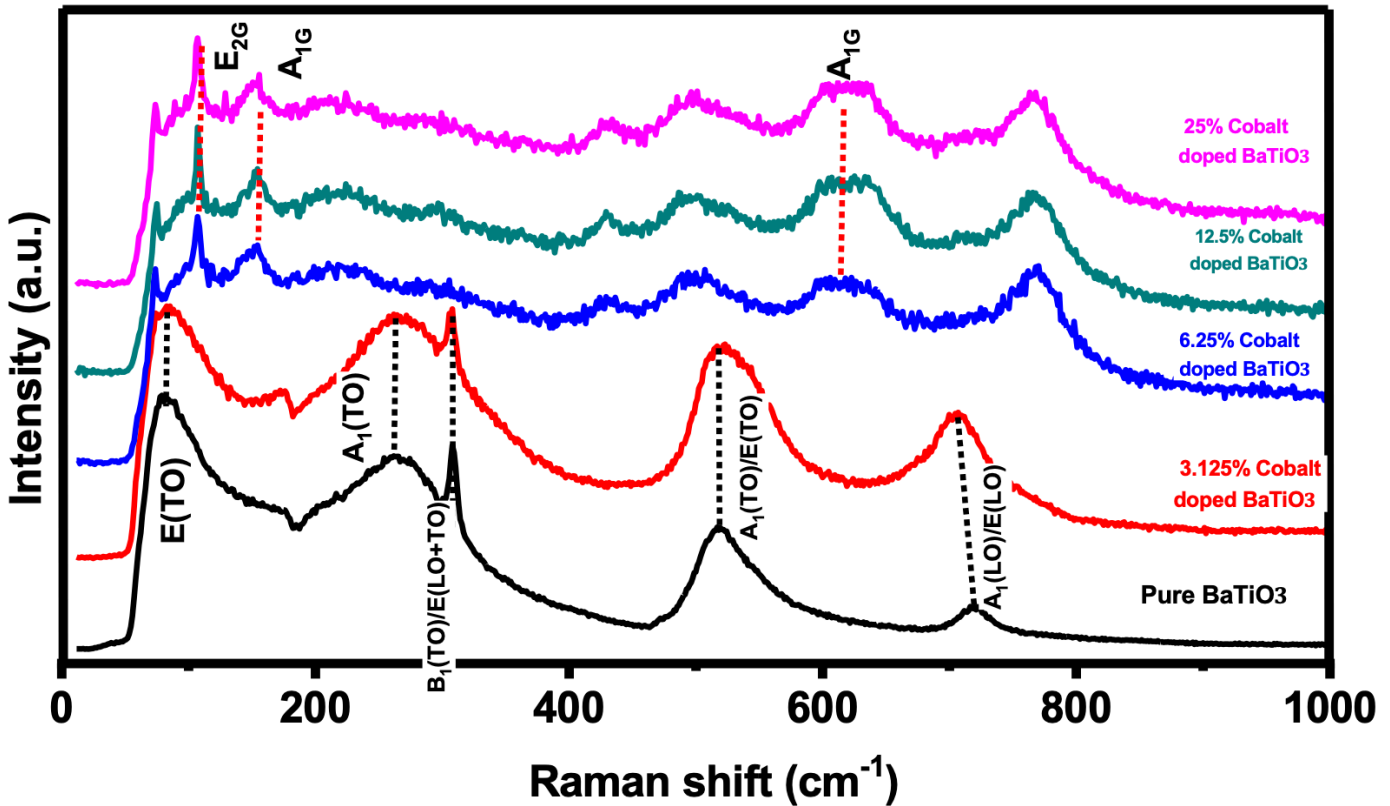
B-site Cobalt doped BaTiO$_3$

Fig 23. Raman spectra of Cobalt Doped B-site BaTiO$_3$ (BaTi$_{1-x}$Co$_x$O$_3$)

The Raman spectra of pure and B-site Cobalt-doped BaTiO$_3$ (3.125%, 6.25%,12.5% and 25%) exhibit notable modifications in vibrational modes, structural distortions, and phase transitions induced by Cobalt doping at site-B. In pure BaTiO$_3$, the sharp and distinct Raman peaks characteristic of the tetragonal. The E(TO) mode (~200 cm^{-1}) corresponds to oxygen vibrations within the tetragonal structure, while the A$_1$(TO) mode (~520 cm^{-1}) is associated with Ti–O bond vibrations. The A$_1$(LO)/E(LO) mode (~720 cm^{-1}) signifies strong polar interactions within the tetragonal phase. The Raman spectrum of 3.125% Co-doped BaTiO$_3$ closely resembles that of pure BaTiO$_3$, with only minor peak broadening, indicating minimal structural disruption and

the persistence of tetragonal symmetry. At 6.25% doping, increased peak broadening is observed, suggesting enhanced lattice strain and a reduction in long-range polar ordering. The slight shifts in the E(TO) mode near 200 cm^{-1} and A$_1$(TO) mode near 520 cm^{-1} imply the onset of a structural transition towards a hexagonal phase. At 12.5% doping, the Raman spectrum further evolves, with peak broadening and a notable reduction in the intensity of tetragonal modes, particularly at A$_1$(TO) (~520 cm^{-1}). Additionally, new vibrational modes emerge near 300 cm^{-1}, which are characteristic of the hexagonal BaTiO$_3$ phase, indicating a significant phase transition. The predominance of the hexagonal phase over the tetragonal structure at higher doping concentration.

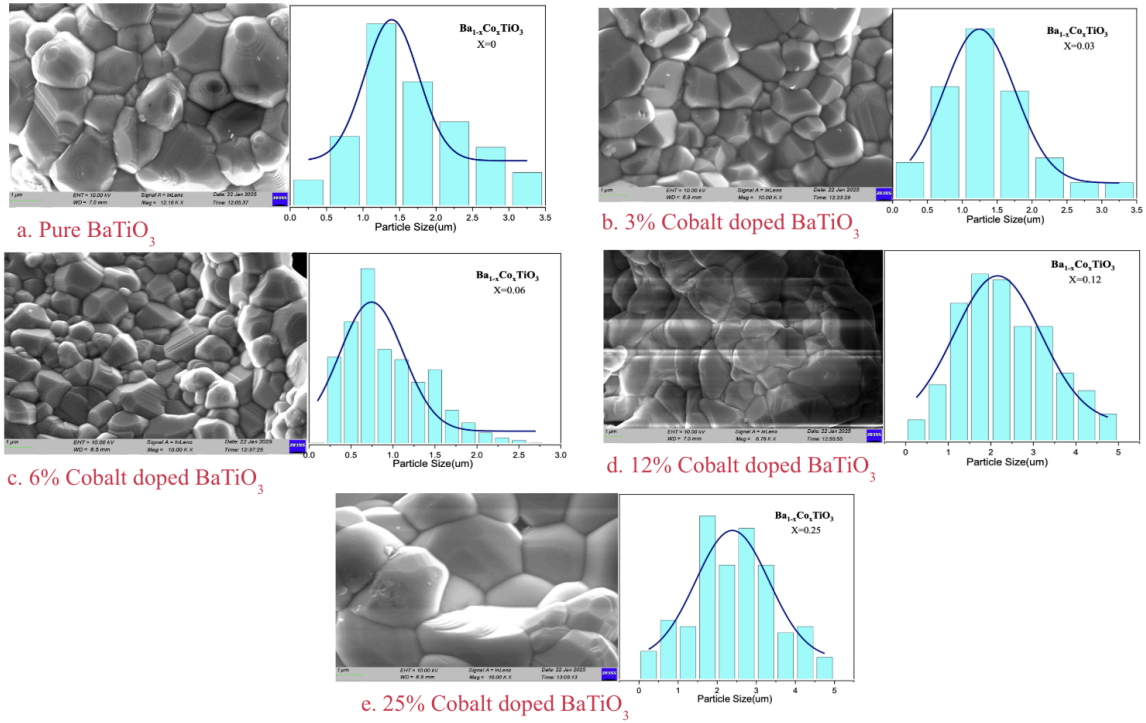## 4.4 FESEM(Field Emission Scanning Electron Microscopy)

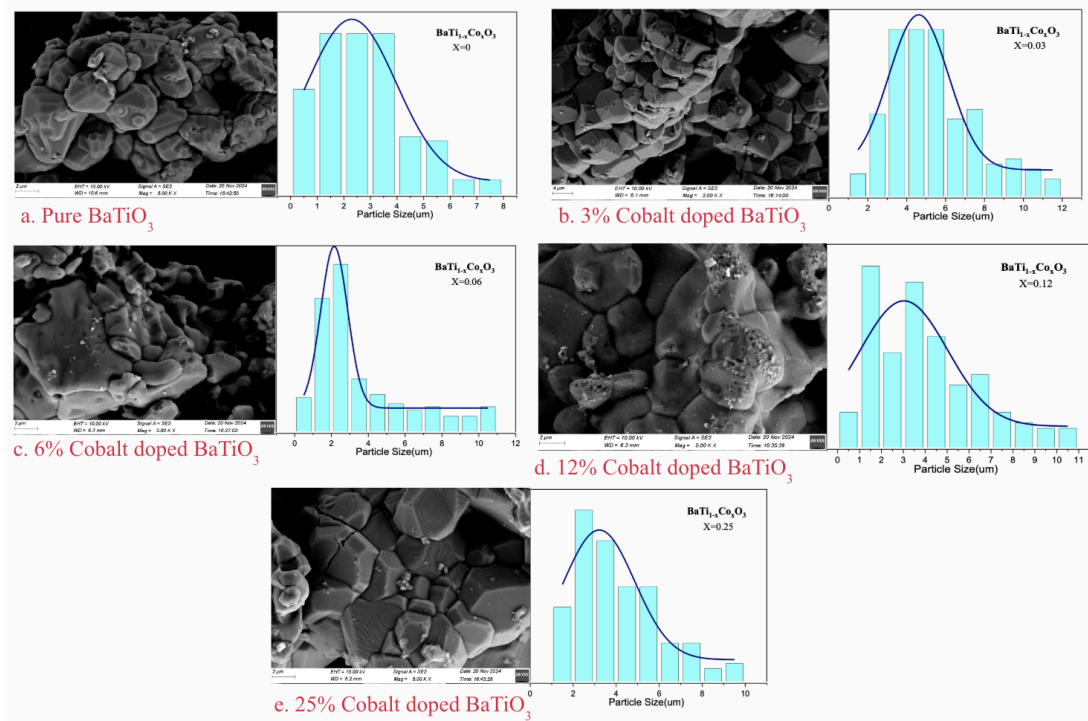Fig 24. FESEM image of Cobalt Doped A-site BaTiO$_3$ (Ba$_{1-x}$Co$_x$TiO$_3$)

Fig 25. FESEM image of Cobalt Doped B-site BaTiO$_3$ (BaTi$_{1-x}$Co$_x$O$_3$)

Field Emission Scanning Electron Microscopy (FESEM) is utilized to investigate the particle size and morphological characteristics of $Ba_{1-x}Co_xTiO_3$ and $Ba\ Ti_{1-x}Co_x\ O_3$ ceramic samples with varying Cobalt doping concentrations (X = 0, 0.03, 0.06, 0.12, and 0.25). Particle size distributions were statistically analyzed from FESEM for each composition, and then results are presented as histograms. The corresponding mean particle size was determined and plotted with a doping concentration of Cobalt. The particle size distribution histograms reveal a significant evolution in the microstructure with increasing Cobalt substitution.
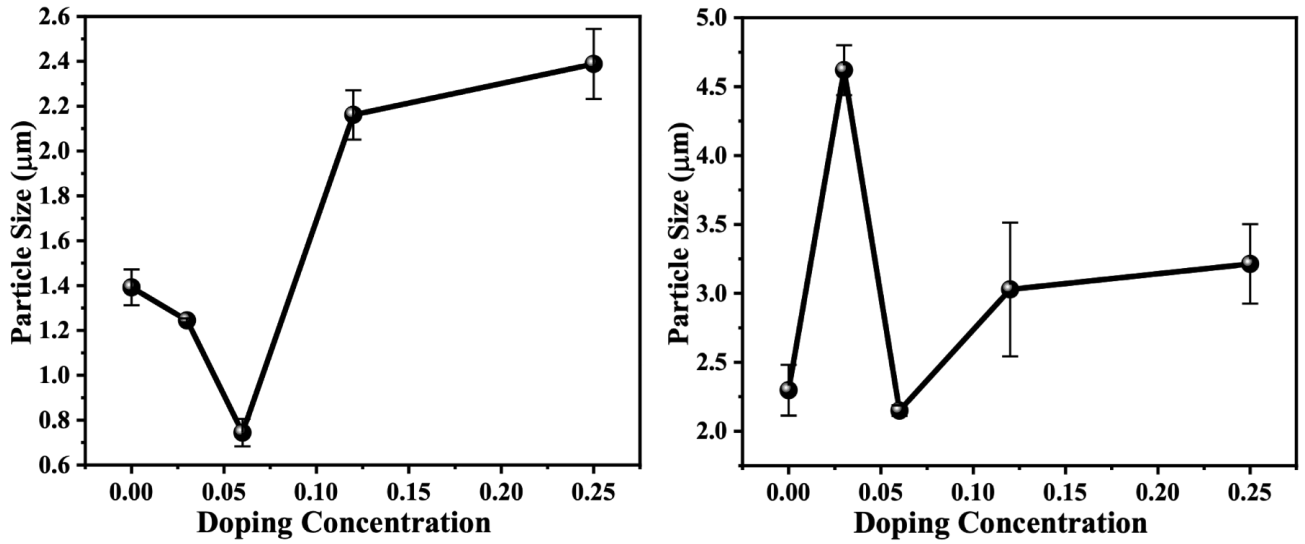

Fig 26. Particle Size Distribution of Cobalt Doped BaTiO₃ a)A-site (Ba₁₋ₓCoₓTiO₃) b)B-site (BaTi₁₋ₓCoₓO₃)

Ba₁₋ₓCoₓTiO₃ ceramics shows a clear shift in how the material's grains grow as more Cobalt is added.For the undoped BaTiO3 (X=0), the histogram shows a relatively broad, unimodal distribution with a mean particle size around 1.4 μm. When we introduce Cobalt in A-site of BaTiO₃, a notable trend in grain size control is observed. At low doping levels (X=0.03), a slight decrease in mean particle size is observed. At doping levels up to X = 0.06 where the mean particle size is significantly reduced to approximately 0.8 μm, Cobalt seems to hold grain growth back, resulting in smaller particles because it may disrupt the structure.This effect is most noticeable at X = 0.06, where the grains are the smallest and the size distribution becomes uneven. But once the Cobalt concentration goes beyond that point (X = 0.12 and 0.25), the distribution becomes wider and more symmetric.It indicates the dominance of abnormal or enhanced grain growth mechanisms, the grains start growing much larger and moreThe particle size vs. doping concentration plot confirms that initial decrease in particle size with slight doping (up to X = 0.06), it may be due to grain growth inhibition.A sharp increase in particle size

65

occurs beyond X = 0.06, indicating activation of mechanisms favoring grain become grow or abnormal growth.When we introduce Cobalt in B-site of $BaTiO_3$,the undoped sample (x = 0) exhibits a relatively broad and most particles in the 1–5 μm range.At a lower doping concentration (X = 0.03),the particle size distribution shifts toward larger values with a peak around 4–6 μm, indicating notable grain growth at low Cobalt concentrations, the grains grow noticeably larger and more evenly, likely because Cobalt helps atoms move around more easily or lowers the energy needed for grain boundaries to grow. But when the doping concentration reaches X = 0.06, with a narrower distribution peaking near 2–3 μm, suggesting that Cobalt incorporation suppresses grain growth at this concentration, possibly due to defect and grain growth suddenly slows down, and the particles become smaller and more uneven and they start disrupting the structure. As the doping concentration increases further (X = 0.12 and 0.25), the distributions become broader again, with peaks near 3–4 μm and the presence of larger grains, though the overall average size remains lower than the peak at x = 0.03 and the grains start to grow again. It shows that Cobalt can both boost and restrict grain growth, depending on how much is added, making its effect quite dynamic and sensitive to doping level.Particle size vs. doping concentration plot confirms the average particle size increases at X = 0.03, but then drops sharply at X = 0.06, followed by a more gradual rise as the Cobalt concentration continues to increase. This pattern suggests that lower doping concentrations help grains grow larger, but when the doping reaches a moderate level, it actually slows down grain growth—likely due to defects introduced by the dopant interfering with the process. As the concentration gets higher, grain growth starts to pick up again, possibly because the effects of those defects begin to balance out with changes.

4.5 I V(Current-Voltage) Measurement
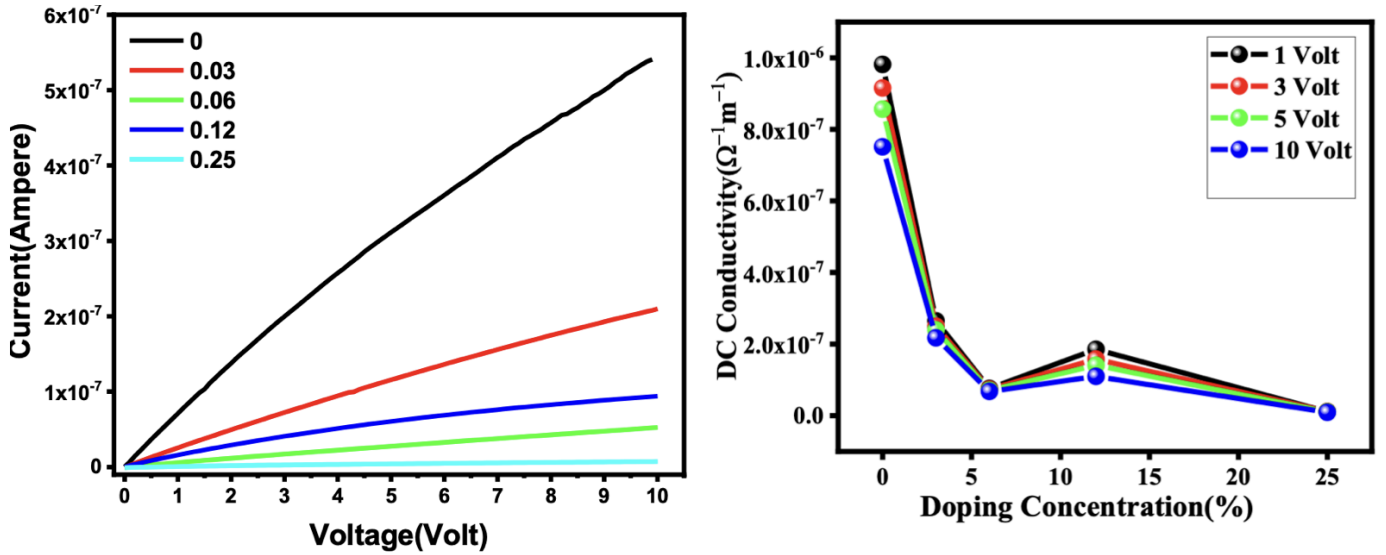
A-site Cobalt doped BaTiO$_3$

Fig 27. IV measurement and Conductivity of Cobalt Doped BaTiO$_3$ a)A-site (Ba$_{1-x}$Co$_x$TiO$_3$)

The IV plot in the positive voltage range (0 V to 10 V) illustrates the current–voltage behavior of pure and Cobalt-doped BaTiO$_3$ samples at the A-site. The undoped sample (black curve) exhibits the highest current, increasing linearly with voltage, indicative of ohmic behavior. As Cobalt concentration increases, the current systematically decreases, and the IV curves become increasingly sublinear. The 3% Co-doped sample (red) maintains relatively high conductivity, but further doping at 6% (green), 12% (blue), and 25% (cyan) significantly suppresses the current, with near-saturation behavior observed at the highest doping levels. This suggests that higher Cobalt concentrations introduce trap states or defect centers, that inhibit charge carrier transport. The corresponding conductivity plots support this observation, showing a marked decrease in conductivity with increasing Co content and confirming that A-site Cobalt doping in BaTiO$_3$ adversely affects electrical transport by creating localized defect states.
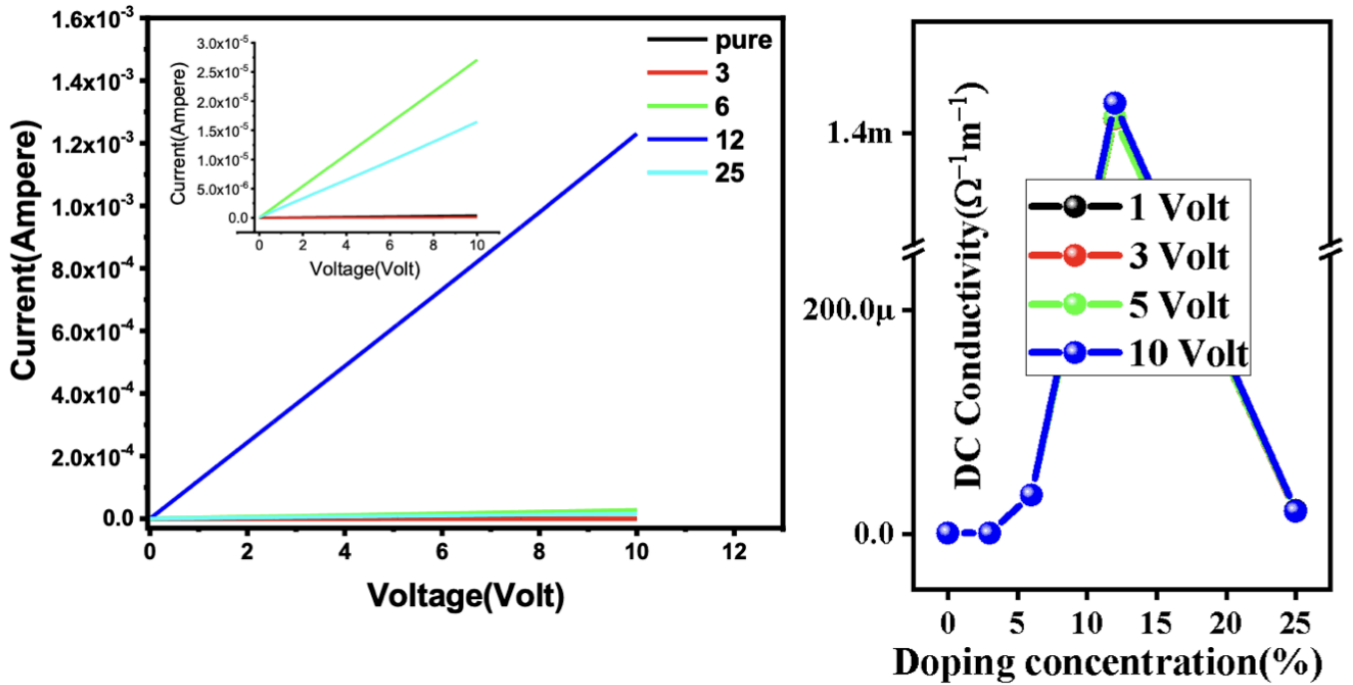
B-site Cobalt doped BaTiO$_3$

Fig 28. IV measurement and Conductivity of Cobalt Doped BaTiO$_3$ B-site (BaTi$_{1-x}$Co$_x$O$_3$)

The IV and conductivity plots for B-site Cobalt-doped BaTiO$_3$ reveal a distinctly different trend compared to A-site doping. The 12% Co-doped sample (dark blue) exhibits the highest current and conductivity, followed by the 6% (green), 25% (cyan), pure (black), and 3% (red) samples. This suggests that moderate B-site Cobalt doping significantly enhances electrical conductivity, likely due to the introduction of additional charge carriers or improved carrier mobility via defect-mediated pathways. Unlike A-site doping, which suppressed conductivity due to the preservation of a tetragonal structure and the introduction of trap states, B-site doping results in enhanced transport, particularly at higher doping levels. A key structural observation further supports this: when Cobalt is doped at the A-site, the BaTiO$_3$ remains tetragonal, leading to suppressed IV and conductivity behavior. Similarly, the 3% B-site Co-doped sample also retains a tetragonal structure, which may explain its lower conductivity relative to other doped samples. In contrast, the 6% and 12% B-site Co-doped samples adopt a hexagonal phase, known for better electrical transport, which correlates with their higher IV and conductivity values. The 25% sample, showing intermediate behavior, likely consists of a mixed tetragonal–hexagonal phase, resulting in moderate conductivity values. Thus, the structural phase transition plays a critical role in modulating the electrical properties upon Co doping in BaTiO$_3$.

4.6 Dielectric Study

4.6.1 Dielectric measurement analysis
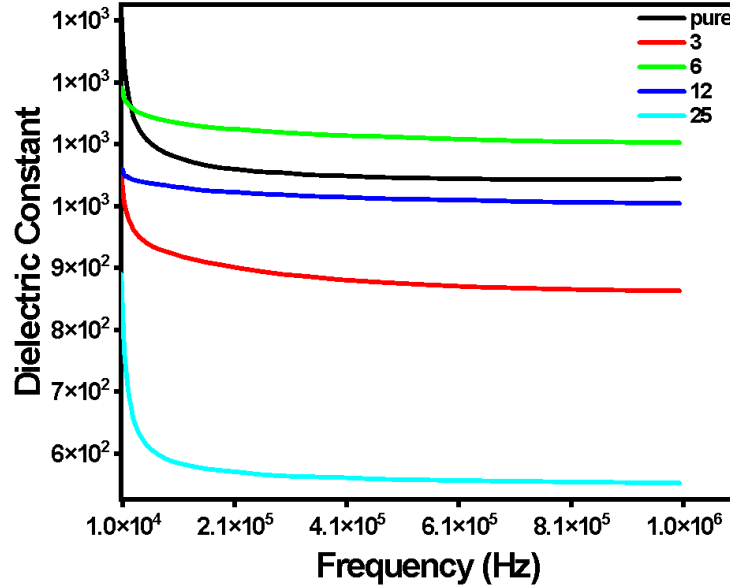
A-site Cobalt doped BaTiO$_3$

Fig 29. Dielectric measurement of Cobalt Doped A-site BaTiO$_3$ (Ba$_{1-x}$Co$_x$TiO$_3$)

The graph illustrates the variation of the dielectric constant (ε') with frequency for pure and A-site Cobalt-doped BaTiO$_3$, with doping concentrations of 0% (black), 3% (red), 6% (green), 12% (dark blue), and 25% (cyan). Across all samples, the dielectric constant slightly decreases with increasing frequency due to reduced interfacial and space charge polarization, which is typical of ferroelectric materials. The 6% Co-doped sample exhibits the highest dielectric constant throughout the frequency range, indicating improved polarizability and ferroelectric stability at this doping level. In contrast, the 25% sample shows the lowest dielectric constant, suggesting that excessive Cobalt incorporation introduces defects that disturb the ferroelectric ordering. The pure BaTiO$_3$ sample falls between these values, with moderate dielectric behavior. Overall, these results indicate that A-site Cobalt doping enhances the dielectric response up to an optimal level (~6%), beyond which dielectric degradation occurs due to defect accumulation.
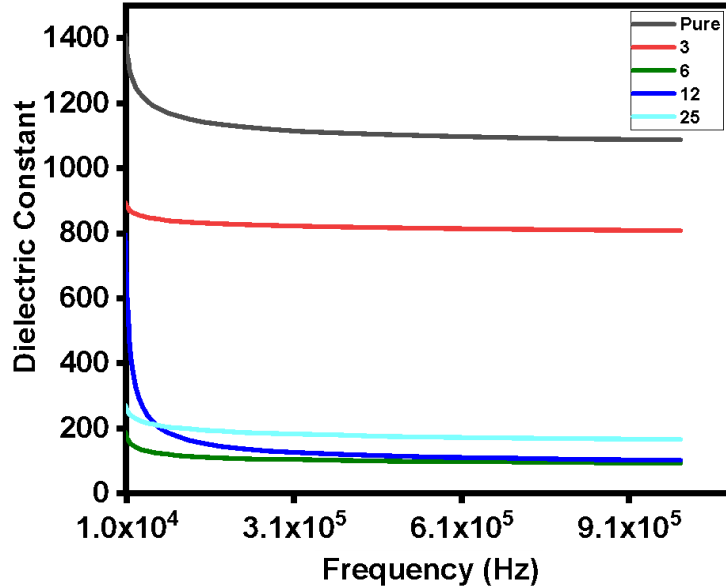
B-site Cobalt doped BaTiO₃

Fig 30. Dielectric measurement of Cobalt Doped B-site BaTiO₃ (BaTi₁₋ₓCoₓO₃)

The dielectric constant behavior of $BaTi_{1-x}Co_xO_3$ ceramics from 10^4 to 10^6 Hz shows a strong dependency on the crystal structure. At 1 MHz, the trend is: Pure > 3% > 25% > 6% > 12%. Pure and 3% Co-doped samples exhibit a tetragonal structure and thus maintain high dielectric constants, reflecting robust ferroelectricity and strong polarizability. In contrast, the 6% and 12% doped samples, which undergo a phase transition to hexagonal structure, show significantly lower dielectric constants because the hexagonal phase is centrosymmetric and non-ferroelectric. The 25% sample, which has a mixed tetragonal + hexagonal phase, shows intermediate dielectric behavior. This dielectric trend supports the IV and DC conductivity results. There is a clear link between the material's phase structure and its dielectric constant at 1 MHz with the tetragonal phases (pure and 3.125% Co-doped) showing higher dielectric values compared to the hexagonal phases (6.25% and 12.5%), this relationship doesn't hold across the entire frequency range from 10^4 to 10^6 Hz. At other frequencies, the dielectric response becomes more scattered, suggesting that other factors, like defect-induced dipolar relaxation or localized charge buildup, might be playing a role. Interestingly, space charge effects are especially noticeable even at higher frequencies, like around 50 kHz for the 12% Co-doped sample. This shows that these extrinsic factors still influence dielectric behavior significantly, even at high frequencies.
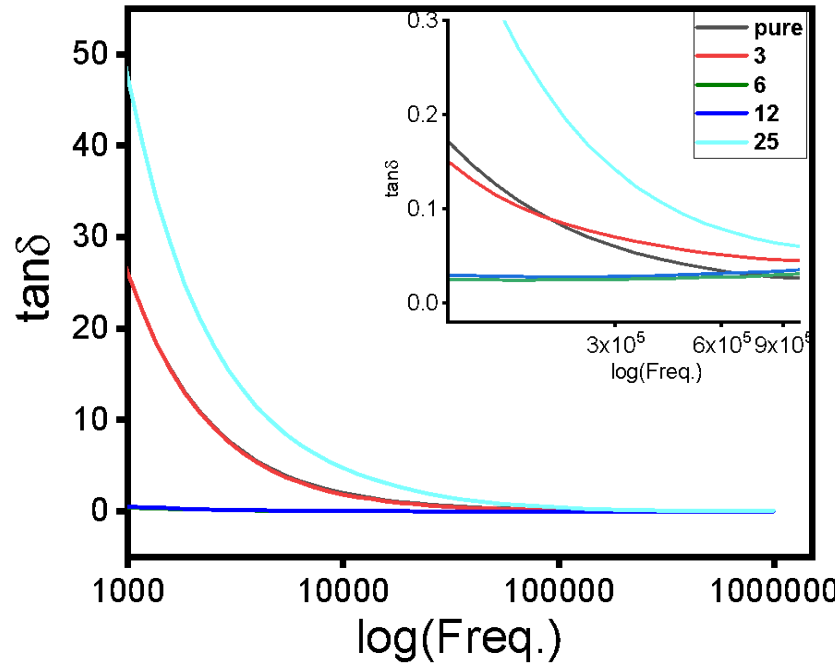
4.6.2 Tan delta

A-site Cobalt doped BaTiO$_3$

Fig 31. Dielectric Loss of Cobalt Doped A-site BaTiO$_3$ (Ba$_{1-x}$Co$_x$TiO$_3$)

The tan δ vs. frequency (log scale) plot for A-site Cobalt-doped BaTiO$_3$ reveals that dielectric loss decreases with increasing frequency across all samples. At lower frequencies (below ~1 kHz), doping significantly increases tan δ, particularly for the 25% sample, which exhibits the highest loss due to enhanced conduction and relaxation losses. Meanwhile, the 6% and 12% doped samples consistently show the lowest dielectric losses, indicating better energy efficiency and less dissipation. As frequency exceeds ~10 kHz, all samples converge to low tan δ values, suggesting that the primary loss mechanisms from doping are most active at lower frequencies and diminish as polarization mechanisms.
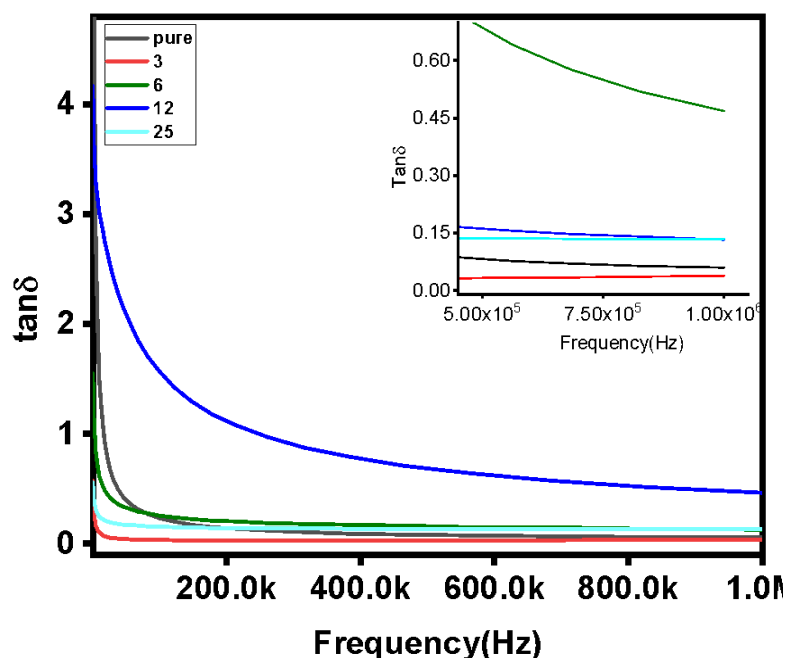
B-site Cobalt doped BaTiO$_3$

Fig 32. Dielectric Loss of Cobalt Doped B-site BaTiO$_3$ (BaTi$_{1-x}$Co$_x$O$_3$)

The graph illustrates how tan delta (dielectric loss) varies with frequency (on a logarithmic scale) for BaTiO$_3$ doped with different concentrations of Cobalt.The dielectric loss (tanδ) is strongly influenced by both the frequency of the applied electric field and the level of Cobalt doping. In the B-site doping case, tan δ generally decreases with increasing frequency. The undoped sample (black) shows the lowest dielectric loss across all frequencies, indicating minimal energy dissipation and the dominance of slower loss mechanisms such as space charge polarization.At 3% doping (red), a small peak appears near ~100 Hz, indicating minor dipolar relaxation. For 6% (green), a broad and significant peak is observed, suggesting enhanced relaxation and conduction losses. The 12% sample (dark blue) exhibits the highest tan δ at low frequencies, primarily due to increased charge carrier motion and defect conductivity. The 25% sample (cyan) shows moderate dielectric loss, lower than 12% and 6% but higher than the pure and 3% samples. The tan δ trend follows: 12 > 6 > 25 > 0 > 3, highlighting the strong link between phase structure and dielectric loss, with hexagonal phases contributing more to dielectric loss due to their intrinsic conduction and relaxation behavior.
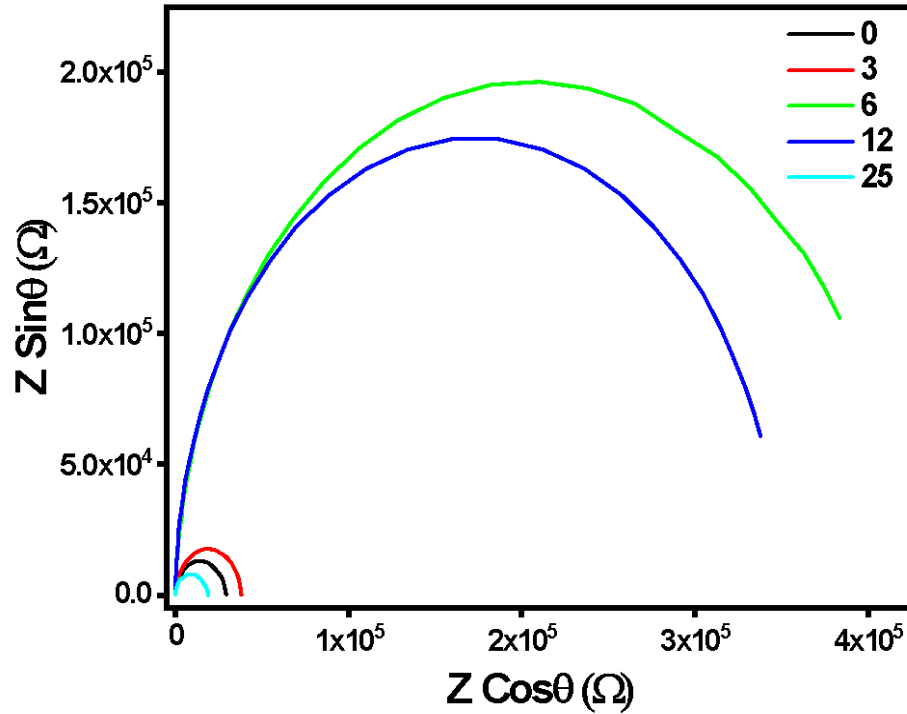
4.6.3 Cole-Cole plot

A-site Cobalt doped BaTiO$_3$

Fig 33. Cole Cole Plot of Cobalt Doped A-site BaTiO$_3$ (Ba$_{1-x}$Co$_x$TiO$_3$)

The Cole-Cole plot, which shows the imaginary part of impedance (Z") versus the real part of impedance (Z') for pure and A-site Cobalt-doped BaTiO$_3$, reveals significant changes in the material's electrical response with doping.The Cole-Cole plots for A-site Cobalt-doped BaTiO$_3$ in all doping concentrations (0%, 3%, 6%, 12%, and 25%), where each sample exhibits a single, depressed semicircle. This indicates the presence of only one dominant relaxation process, typically attributed to grain or grain boundary contributions.The pure (black) and 3% Co (red) samples exhibit small semicircles, indicating low resistance and dominant grain (bulk) contributions. As the Co concentration increases to 6% (green), the semicircle becomes much larger, indicating a sharp rise in resistance, likely due to enhanced grain boundary effects or defect accumulation. The 12% Co-doped sample (dark blue) shows a similarly large arc, maintaining high resistance. Interestingly, at 25% doping, the semicircle becomes smaller again, suggesting reduced resistance—possibly due to the formation of conductive paths or phase mixing effects. The presence of single, depressed semicircles in all cases suggests a distribution of relaxation times within the material, typically associated with grain boundary effects. Each semicircle corresponds to a parallel RC element, where the relaxation behavior is characterized by

the time constant **(τ = RC)**. This trend overall implies that Cobalt doping introduces complex relaxation behavior, marking a transition from resistive to more conductive characteristics.
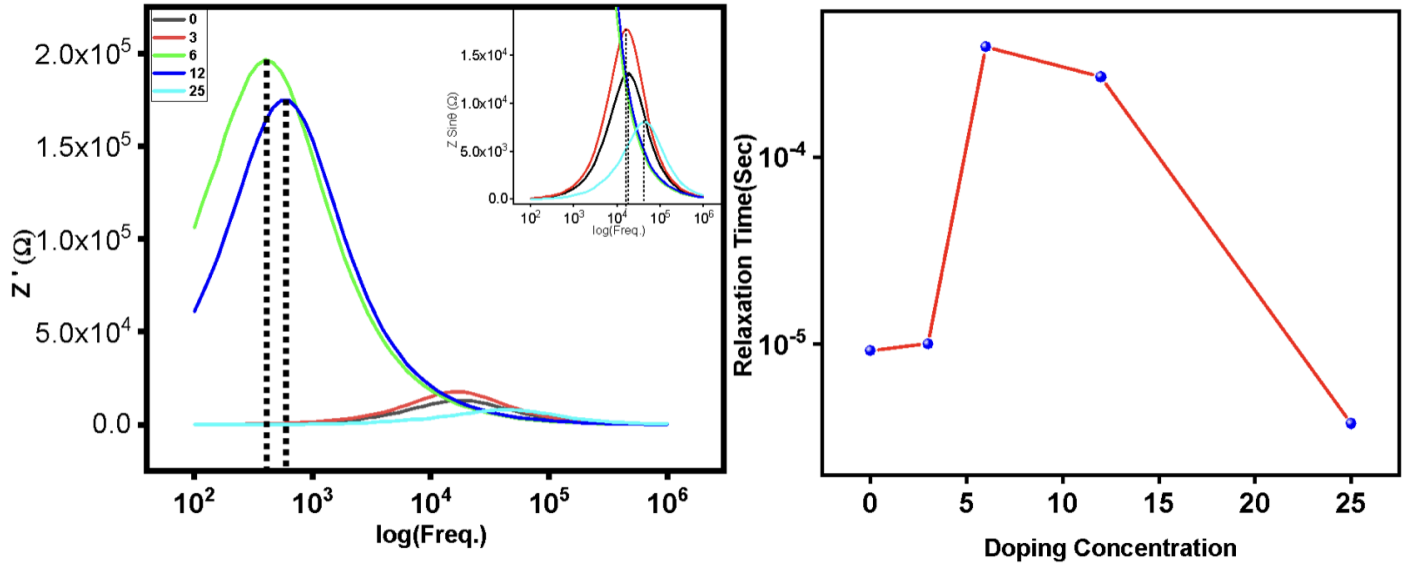

Fig 34. a)Z″ vs. Frequency and b)Relaxation Time Analysis for A-site Co-Doped BaTiO$_3$

These combined plot effectively shows the evolution of electrical relaxation behavior in A-site Cobalt-doped BaTiO$_3$, plot both Z″ (imaginary impedance) at y-axis vs. frequency at x-axis. That reveals a single relaxation peak for each doping level, indicating a dominant relaxation process likely associated with grain boundary effects. The relaxation time (τ) was calculated using the relation

$$\tau = \frac{1}{2\pi f_{\max}}$$

(4.1)

$f_{\max}$ is the frequency at the Z″ peak.

The resulting τ values plotted against Cobalt doping concentration show a non-steady trend.τ increases significantly from pure to 6% and 12% Co doping, indicating increased resistance and delayed relaxation due to enhanced defect density and charge trapping at grain boundaries.At 6% and 12% Co doping, indicating a slowing of the relaxation process likely caused by increased defect concentration. Interestingly, at 25% Co doping, τ decreases again, implying faster relaxation potentially due to the formation of conductive pathways. This behavior reflects a transition from a resistive to a more conductive arrangement.
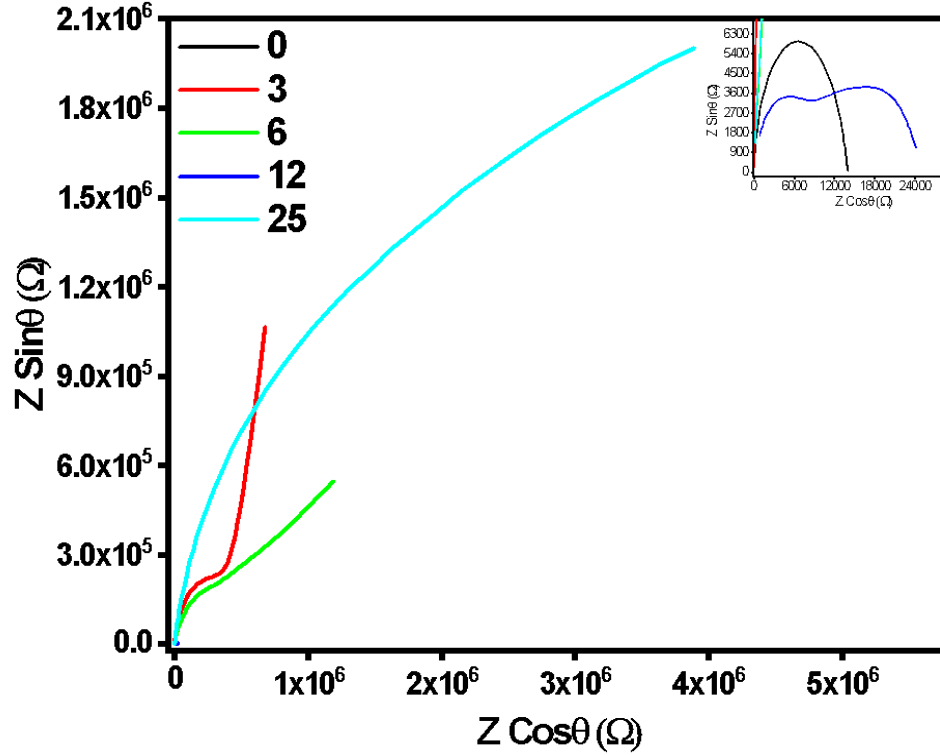
B-site Cobalt doped BaTiO$_3$

Fig 35. Cole Cole Plot of Cobalt Doped B-site BaTiO$_3$ (BaTi$_{1-x}$Co$_x$O$_3$)

The Cole-Cole plots for B-site Co-doped BaTiO$_3$ exhibit more complex impedance behavior. The pure (0%) sample shows a single, well-defined semicircle, indicating one relaxation process primarily due to grain contribution. The 12% Co-doped sample clearly displays multiple arcs, pointing to the presence of more than one relaxation process, likely originating from grain, grain boundary, and possibly interfacial effects. In the 3%, 6%, and 25% Co-doped samples, we can also clearly see the presence of more than one relaxation process; however, the arcs remain incomplete within the measured frequency range (up to 1 MHz). This makes it difficult to fully characterize the relaxation mechanisms, as these arcs likely extend beyond the available data range. Therefore, while multiple relaxations are evident in B-site doping, especially at intermediate concentrations, extended frequency measurements would be necessary to fully capture and resolve the impedance behavior of the 3%, 6%, and 25% samples.
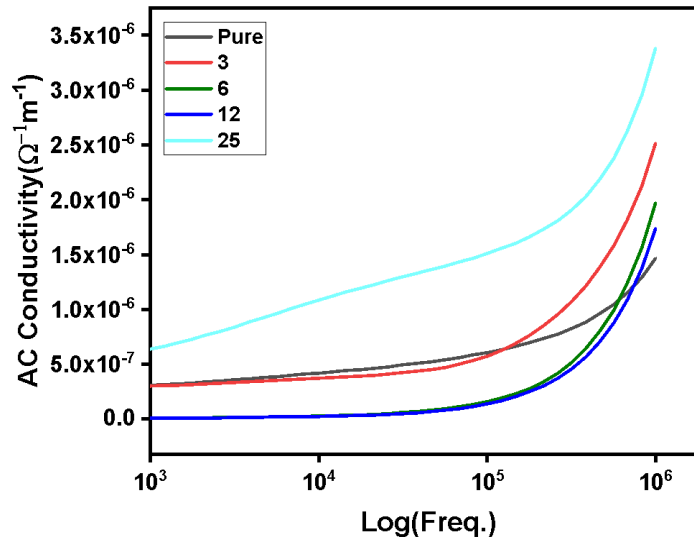
4.6.4 AC- conductivity

A-site Cobalt doped BaTiO$_3$

Fig 36. AC Conductivity of Cobalt Doped A-site BaTiO$_3$ (Ba$_{1-x}$Co$_x$TiO$_3$)

The AC conductivity response of A-site Cobalt-doped BaTiO$_3$ shows a consistent rise in conductivity with increasing Cobalt content. The sample with 25 mol% Co shows the highest conductivity, reaching about 3.4×10^{-6} $\Omega^{-1} \cdot m^{-1}$ at 10^6 Hz. This improvement is likely due to the introduction of charge-compensating defects—such as barium vacancies, oxygen vacancies, and electron holes—created when Co^{2+} or Co^{3+} replaces Ba^{2+} in the lattice.These defects help charge carriers move more easily, especially at higher frequencies where hopping conduction tends to dominate. Interestingly, the 12 mol% Co sample behaves a bit differently, its conductivity is relatively low at lower frequencies, which could be due to charge carriers getting trapped or blocked at grain boundaries. But as frequency increases, its conductivity rises sharply, suggesting that bulk conduction becomes more active and overcomes these barriers.For the pure and lower Cobalt-doped BaTiO$_3$ samples (3% and 6%), the AC conductivity follows a steady upward trend with increasing frequency. The undoped BaTiO$_3$ sample exhibits a relatively low level of conductivity, serving as a reference point for comparison. Introducing a small amount of Cobalt (3%) leads to a slight increase in conductivity, which is likely due to the generation of additional charge carriers, such as oxygen vacancies or electron holes, resulting from the substitution of Ba^{2+} with Co ions. With 6% Cobalt, the effect becomes more noticeable, especially at higher frequencies, where conductivity rises more sharply. This suggests that the added Cobalt is creating more defects in the structure, which in turn help the charges move more freely through the material.
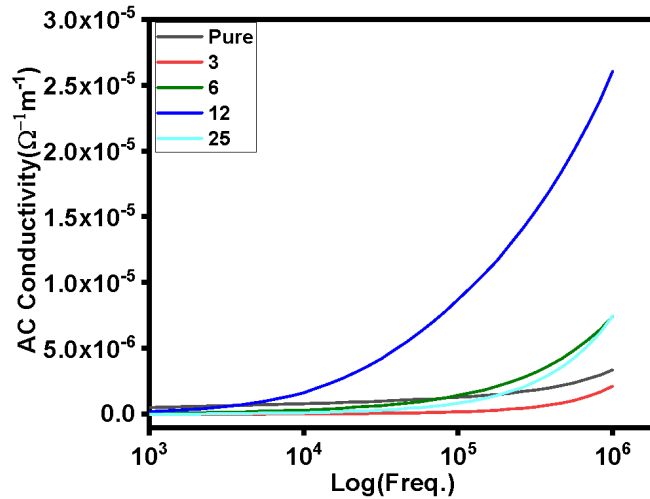
B-site Cobalt doped BaTiO$_3$

Fig 37. AC Conductivity of Cobalt Doped B-site BaTiO$_3$ (BaTi$_{1-x}$Co$_x$O$_3$)

In B-site Co-doped BaTiO$_3$, the AC conductivity shows a distinctly different behavior compared to A-site doping, with clear sensitivity to both frequency and the material's structural phase. At low frequencies (around 10^3 Hz), the conductivity remains fairly consistent across all doping levels. However, as the frequency increases especially beyond 10^5 Hz a significant rise in conductivity is observed, particularly for samples with 6%, 12%, and 25% Co doping. Notably, the conductivity at high frequencies follows the order: 6 > 12 > 25 > pure > 3. This trend aligns well with the structural phase evolution, where the 6% sample, rich in the hexagonal phase, exhibits the highest conductivity, followed by mixed-phase (tetragonal + hexagonal) at 12%, and primarily tetragonal structures (pure and 3%) showing the lowest. The improved conductivity in hexagonal-rich samples may stem from the unique face-sharing TiO$_6$ octahedra in the hexagonal structure, which potentially offer straighter or less hindered pathways for charge movement compared to the more distorted corner-sharing octahedra in the tetragonal phase. When Co^{2+} or Co^{3+} replaces Ti^{4+}, it introduces a charge imbalance that's typically compensated by forming oxygen vacancies (V$_o$••). These vacancies act as charge carriers, enabling hopping conduction especially at higher frequencies, where short-range, localized movement becomes more significant. Since the B-site is central to the octahedral framework of BaTiO$_3$, even small changes here can have a big impact on how electrons and ions move through the material. Interestingly, the fact that 6% doping shows better conductivity than 12% or 25% might indicate that too much doping could cause clustering or other disruptions that actually block conduction paths. This highlights how crucial both the crystal structure and defect landscape are in tuning the high-frequency transport properties of BaTiO$_3$**.**

4.6.5 Temperature Dependent Dielectric Measurement
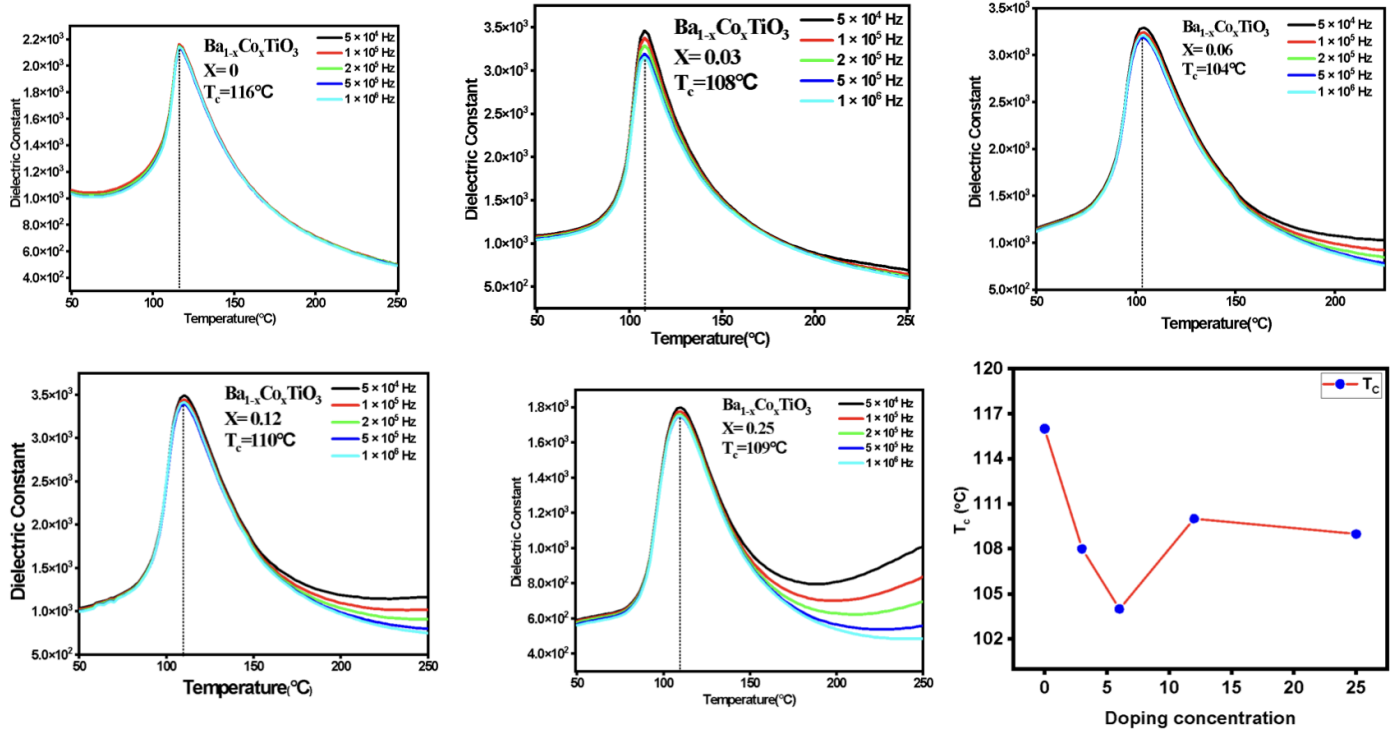
A-site Cobalt doped BaTiO₃

Fig 38. Temp. Dependent Dielectric measurement of Cobalt Doped A-site BaTiO₃ (Ba₁₋ₓCoₓTiO₃)

The temperature-dependent dielectric constant plots for A-site Co-doped BaTiO₃ show how dielectric behavior varies with both temperature and doping concentration. All compositions maintain a tetragonal structure at room temperature. The dielectric constant exhibits a prominent peak near the Curie temperature (T_c), characteristic of a ferroelectric-to-paraelectric phase transition. As doping increases from 0% to 25%, the peak value and position of T_c shift. The undoped sample (x = 0) shows a T_c of 116 °C, while doping to 3% significantly reduces T_c to around 103 °C, indicating suppression of ferroelectric ordering at low doping. As the doping increases to 6% and 12%, Tc slightly improves, reaching 104°C and 110°C, indicating a partial recovery of ferroelectric stability.. However, at 25% doping, T_c again slightly decreases to 108 °C. The frequency dispersion around T_c becomes more evident at higher doping levels, particularly at 12% and 25%, indicating increased relaxation behavior likely due to defect-induced localized polar regions. It is due to the suppression of the Curie temperature (T_C) and a diffuse phase transition, indicating the relaxor-like behavior due to Co-induced lattice disorder and local structural distortions. Additionally, the frequency dispersion of the dielectric

peak and the reduced sharpness of the ferroelectric-to-paraelectric transition in the dielectric plots mirror the relaxor characteristics highlighted in the literature, the A-site Co doping disrupts long-range ferroelectric ordering and enhances polar nano-regions (PNRs), leading to a frequency-dependent and broadened dielectric response .A-site Co doping weakens ferroelectricity by lowering Tc, though a non-monotonic trend suggests a complex interplay between structural distortion, and polarization dynamics.
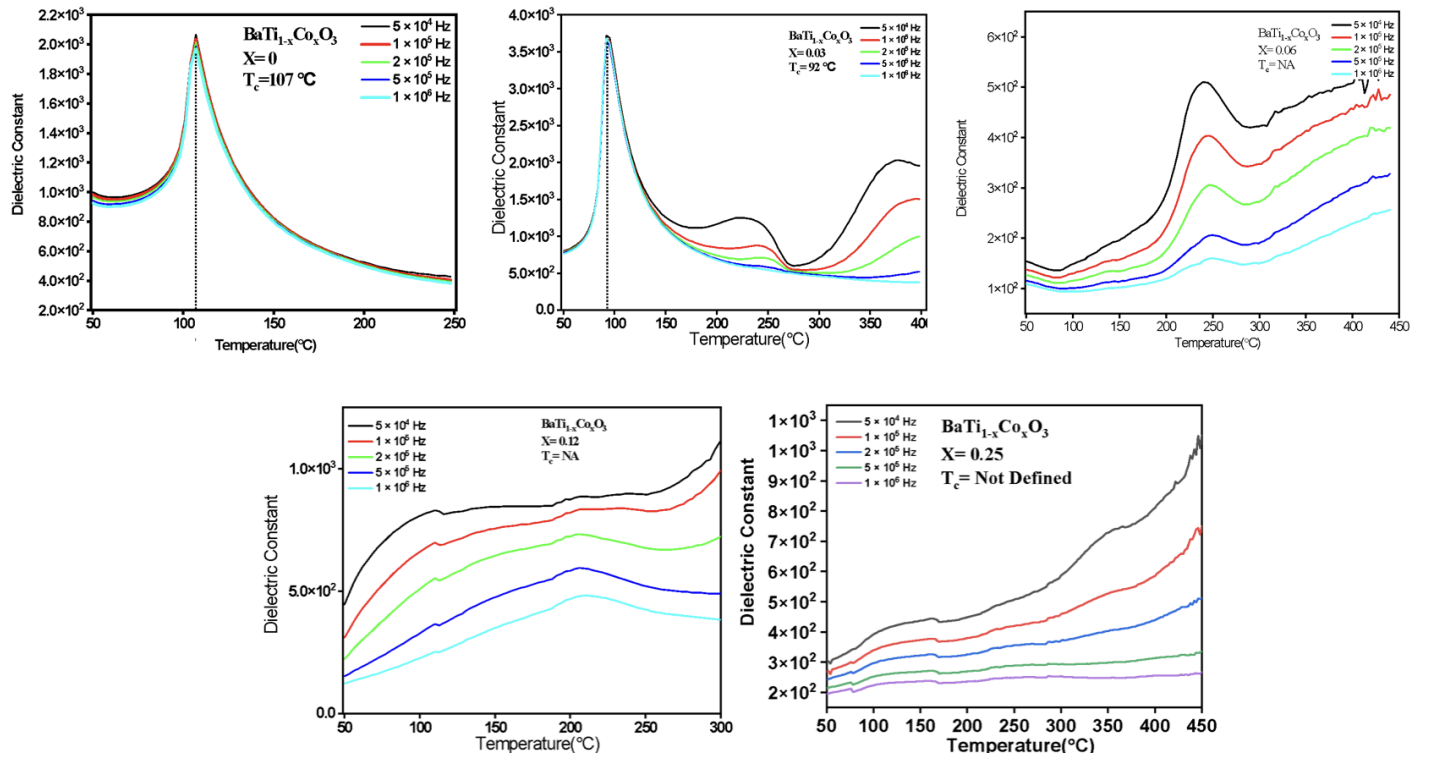
B-site Cobalt doped BaTiO$_3$

Fig 39. Temp. Dependent Dielectric measurement of Cobalt Doped B-site BaTiO$_3$ (BaTi$_{1-x}$Co$_x$O$_3$)
The temperature-dependent dielectric constant plots for B-site Co-doped BaTiO$_3$ reveals a clear structural and ferroelectric behaviour with increasing doping concentration. For the undoped (x = 0) and lower Cobalt doped concentrations (x = 0.03) samples, which maintain a tetragonal phase at room temperature, a sharp dielectric peak is observed near the Curie temperature (Tc), indicating a classic ferroelectric-to-paraelectric transition. The T_c drops from 107 °C in the pure sample to 92 °C at 3% doping, showing that B-site substitution weakens ferroelectric ordering. However, as doping increases to 6%, 12%, and 25%, the crystal structure shifts to hexagonal, and the sharp dielectric peak disappears with the absence of a structural phase transition and T_c in these compositions and indicating the relaxor-like characteristics and a suppression of long-range ferroelectricity. These observations align

with B-site Co doping disrupts the TiO_6 octahedral network more strongly than A-site substitution, stabilizing a non-ferroelectric hexagonal phase that prevents typical phase transitions. The loss of Tc and emergence of broad, diffused dielectric responses reflect how structural distortion, defect chemistry, and local polarization effects dominate the dielectric behavior in heavily doped B-site systems.

Conclusion

Cobalt-doped BaTiO$_3$ samples with varying concentrations (0% to 25%) were synthesized using the sol-gel method to explore the effects of A-site (Ba$_{1-x}$Co$_x$TiO$_3$) and B-site (BaTi$_{1-x}$Co$_x$O$_3$) substitution. Structural analysis via XRD and Raman spectroscopy revealed that A-site doping preserved the tetragonal P4mm phase across all doping levels, though impurity phases and lattice disorder increased with higher Cobalt content, while B-site doping induced a clear tetragonal-to-hexagonal (P6$_3$/mmc) phase transition starting at 6.25%, becoming dominant at 12.5%. FESEM imaging showed that A-site Cobalt initially inhibited grain growth but promoted abnormal grain growth at higher concentrations, whereas B-site doping had a non-linear effect on grain size depending on the level of Cobalt substitution. Electrically, A-site doping decreased conductivity due to defect-induced charge transport hindrance, while B-site doping significantly enhanced conductivity, particularly in hexagonal-rich samples, due to improved transport pathways. Dielectric analysis indicated that A-site doping maintained higher dielectric constants and lower losses around 6%, while B-site doping led to diminished dielectric performance and loss of the ferroelectric transition due to the dominance of the non-ferroelectric hexagonal phase. Overall, the study demonstrates that Cobalt doping at different lattice sites exerts contrasting effects on BaTiO$_3$, with A-site doping preserving ferroelectricity and enabling controlled property tuning via defect engineering, and B-site doping inducing structural transitions that enhance electrical conductivity at the expense of dielectric and ferroelectric performance. The pronounced magnetodielectric response in B-site-doped samples further underscores the crucial role of dopant site selection in tailoring the multifunctional behavior of BaTiO$_3$ ceramics.

Extrawork

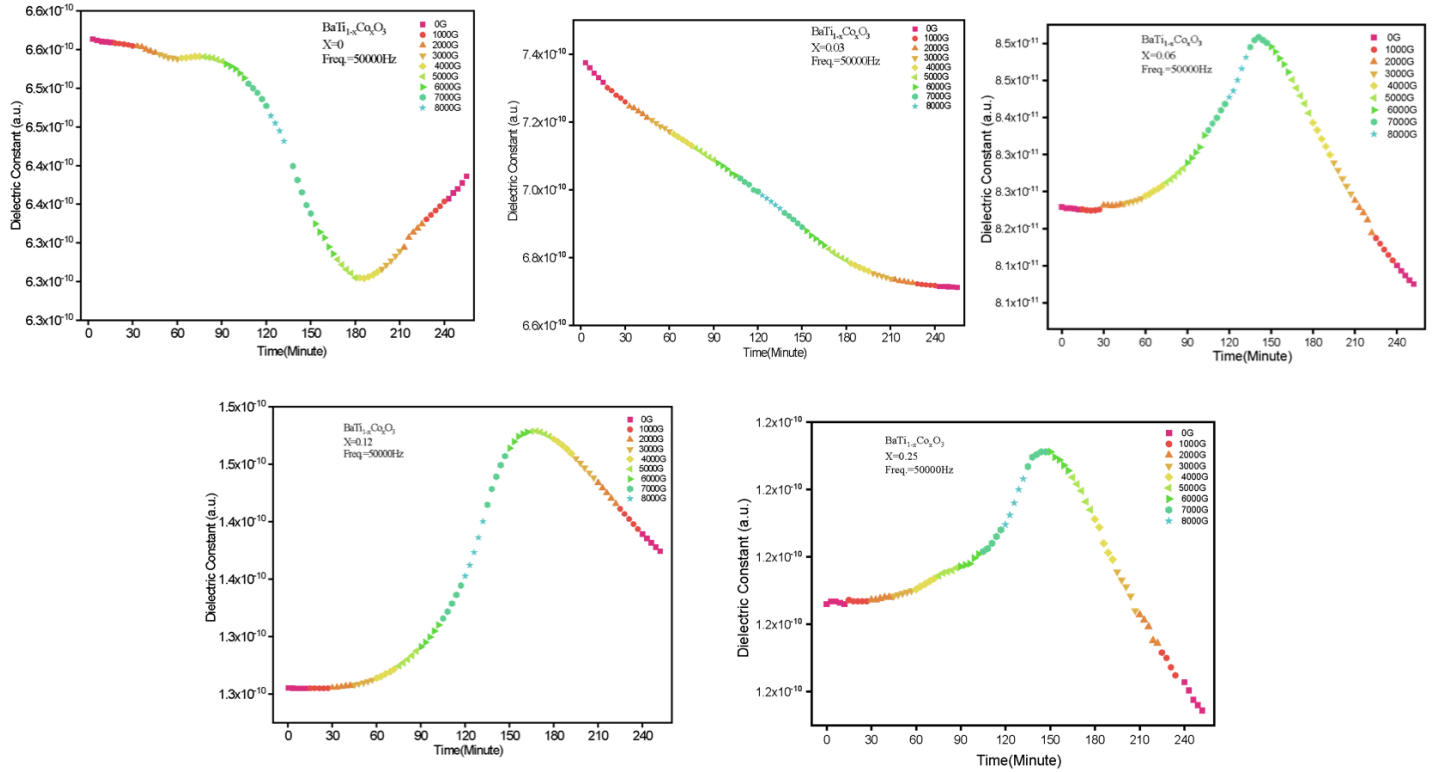## A. Magneto-dielectric measurement of B-site Cobalt doped BaTiO₃

Fig 5.1 Magneto-Dielectric measurement of Cobalt Doped b-site BaTiO₃ (BaTi₁₋ₓCoₓO₃)

The magnetodielectric data of Cobalt-doped BaTiO₃, where Cobalt is substituted at the B-site, was measured by measuring the dielectric constant as a function of time while varying the magnetic field. In this setup, the dielectric response was monitored using an LCR meter as the sample was placed between the poles of an electromagnet. The x-axis represents time, correlating with the gradual change in magnetic field strength, while the y-axis shows the corresponding dielectric constant. This method allows for observing how the dielectric properties evolve under different magnetic fields. In B-site Cobalt-doped BaTiO₃ (BaTi₁₋ₓCoₓO₃), the magnetodielectric response changes noticeably with increasing Co concentration (x = 0 to 0.25). In the lower Cobalt doped samples (x = 0 and 0.03), the dielectric constant gradually decreases with increasing magnetic field, indicating only a weak interaction between magnetic and dielectric behavior. As the Co content increases to x = 0.06 and beyond, a clear peak appears in the dielectric constant, revealing a stronger magnetodielectric effect. This indicates that the magnetic field begins to significantly influence dielectric polarization, which is known as magnetoelectric coupling. This enhancement is directly linked to Cobalt doping at the B-site

(replacing Ti^{4+}), which introduces unpaired d-electrons and local magnetic moments into the lattice. Unlike Ti^{4+}, Co^{2+}/Co^{3+} ions possess magnetic spins, leading to the magnetization in non-magnetic $BaTiO_3$ matrix. These magnetic ions interact with the crystal lattice, resulting in spin-lattice coupling that affects dielectric properties under a magnetic field. Together, the dielectric and spectroscopy data confirm that B-site Cobalt doping not only introduces magnetism into $BaTiO_3$ but also strengthens the interplay between its magnetic and electric properties, giving rise to a magnetodielectric effect.
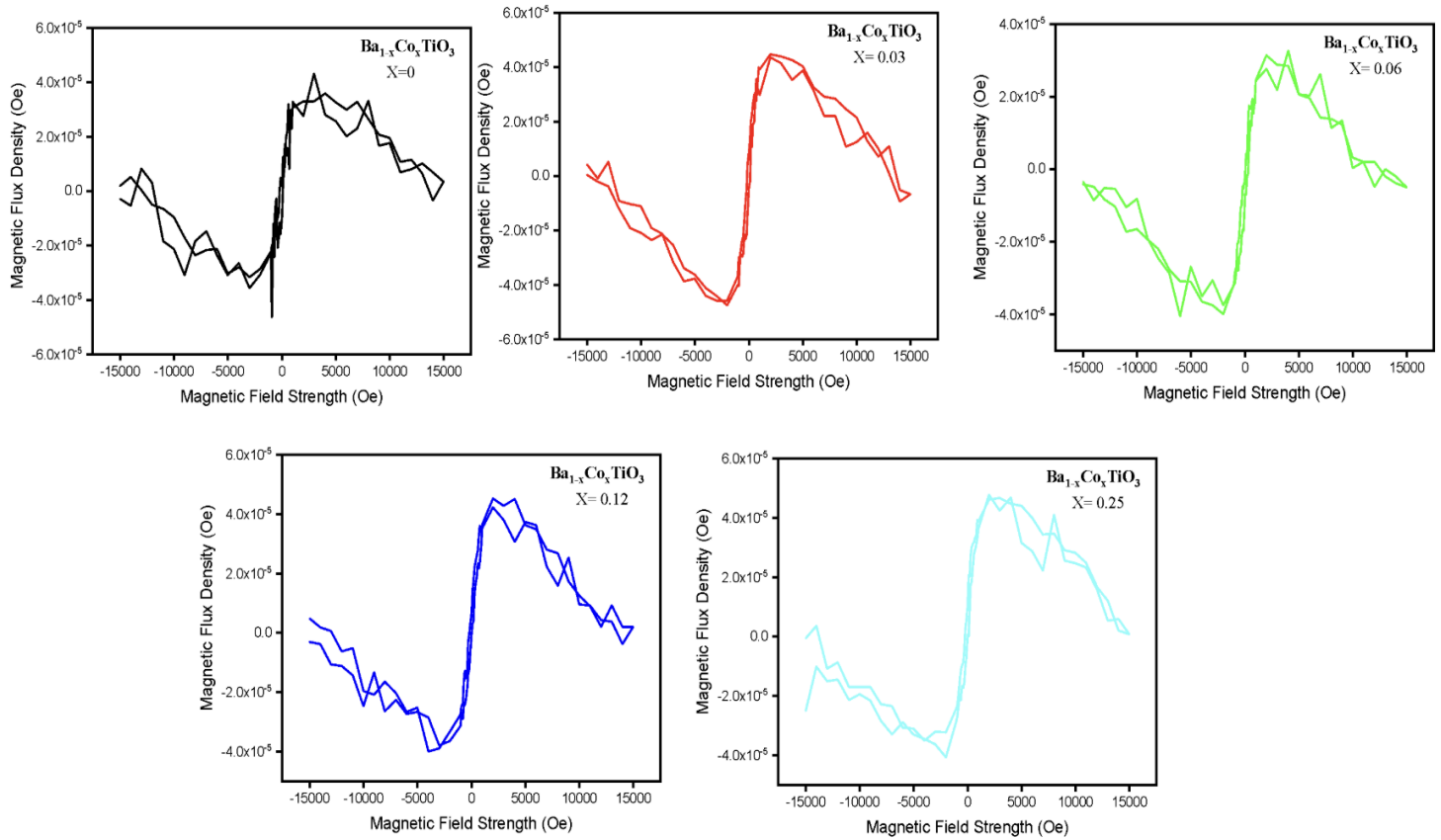
B. Hysteresis Loop or BH Measurement

Fig 5.2 BH measurement of Cobalt Doped A-site BaTiO$_3$ (Ba$_{1-x}$Co$_x$TiO$_3$)

The B–H hysteresis loops of A-site Cobalt-doped BaTiO$_3$ (Ba$_{1-x}$Co$_x$TiO$_3$) shows magnetic behavior with increasing Co concentration. The undoped sample (x = 0) exhibits no magnetic hysteresis, confirming its inherently non-magnetic nature. At low doping levels (x = 0.03 and 0.06), the loops remain nearly linear and closed, indicating no magnetism or extremely weak magnetic interactions, possibly due to minor paramagnetic contributions. As the doping level increases to x = 0.12 and x = 0.25, the loops show observable openings with finite remnant magnetization and coercivity, indicating the emergence of weak ferromagnetic behavior. This weak magnetism is likely induced by Co^{2+} substitution at the A-site, which, through indirect exchange interactions with nearby Ti^{4+}–O^{2-}–Co^{2+} pathways or oxygen vacancy-mediated coupling, introduces localized magnetic moments into the otherwise non-magnetic perovskite lattice.The asymmetry and shape of the loops suggest **weak ferromagnetism** or **canted antiferromagnetism** rather than strong ferromagnetism, which is common in diluted magnetic systems.

C. Piezoelectric Measurement of PVDF-BTO composite using IC 555 timer (Astble Multivibrator).
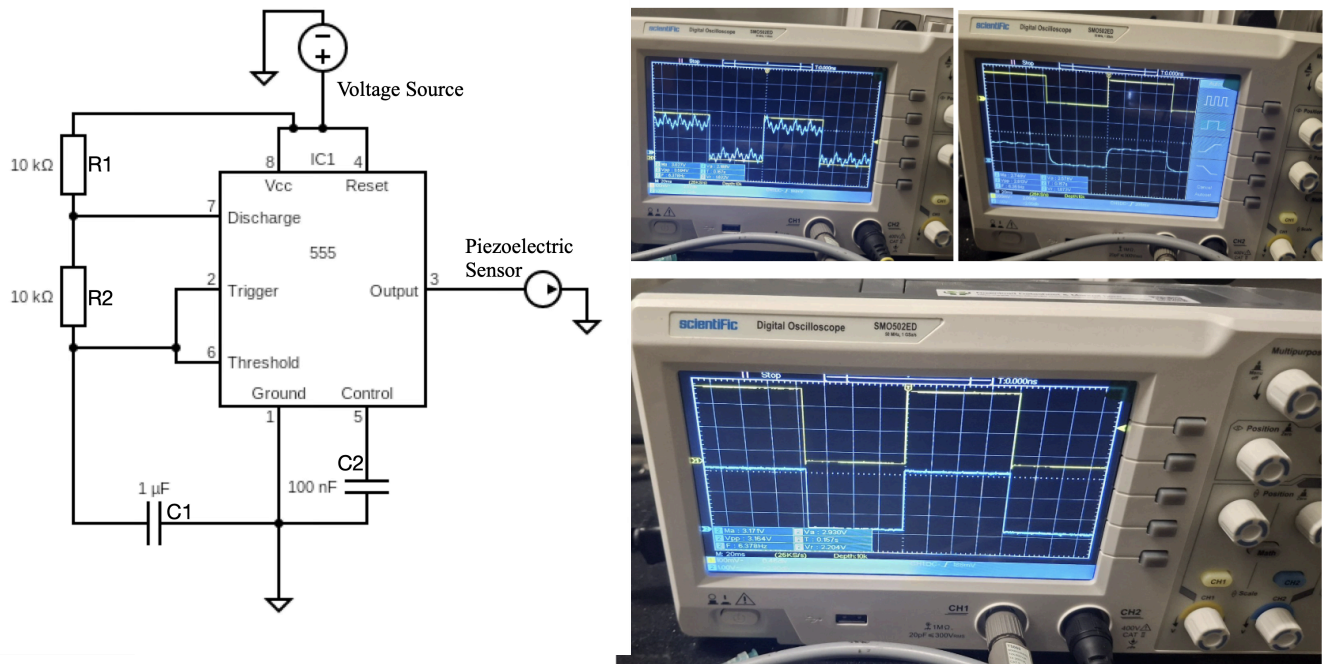

Fig 5.3 a)Circuit Diagram of Astable Multivibrator using IC555 b)Piezoelectric Response of PVDF-BTO Composite

I investigated the piezoelectric behavior of pure polyvinylidene fluoride and PVDF–BaTiO₃ (BTO) composite films, with the objective of understanding how the incorporation of ferroelectric BaTiO₃ nanoparticles affects the piezoelectric response of the polymer matrix. The films were fabricated using the solution casting technique, and during sample preparation, the PVDF and PVDF–BaTiO₃ composite pastes were applied onto copper strips to serve as the bottom electrode, while a layer of silver foil was placed on the top surface of the films to act as the top electrode. This electrode arrangement enabled the measurement of output piezoelectric voltage when the samples were subjected to mechanical stress. The testing was performed using a custom-built setup where electrical excitation and mechanical response were carefully coordinated. To drive this system, I constructed a square wave generator circuit using the IC 555 timer configured as an astable multivibrator, which continuously outputs a square wave without external triggering. In this mode, the IC 555 operates as an oscillator by cyclically charging and discharging a timing capacitor through two resistors (R1 and R2), creating a repetitive square wave signal at output pin 3. The timing characteristics are governed by the relations :

- $T_1 = 0.693 \times (R1 + R2) \times C,$

$$\bullet \quad T_2 = 0.693 \times R2 \times C,$$

$$\bullet \quad T = T_1 + T_2,$$
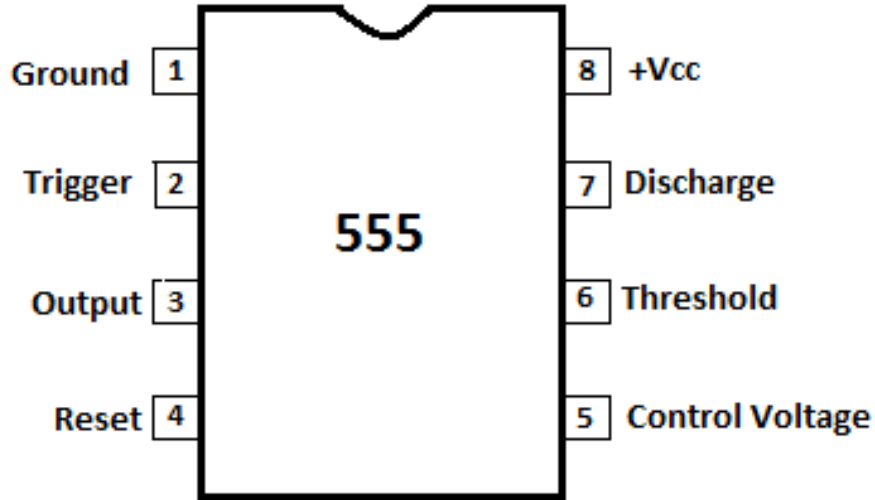
$$\bullet \quad f = \frac{1}{T}$$

Fig 5.4 Pin diagram of IC 555

where T_1 is the high time, T_2 is the low time, T= total time period, f= frequency and C is the capacitor. The pin configuration involved connecting pins 6 and 2 (threshold and trigger) together, tying pin 4 (reset) to Vcc, and using a capacitor at pin 5 for stability. The output square wave was used to electrically excite a commercial piezoelectric actuator, which, via the **inverse piezoelectric effect**, converted the electrical signal into mechanical deformation. This actuator was placed in physical contact with the PVDF and PVDF–$BaTiO_3$ composite films, transferring the mechanical stress to them. The samples responded to this mechanical input through the **direct piezoelectric effect**, generating voltage outputs that were recorded using a Digital Storage Oscilloscope (DSO). The PVDF–$BaTiO_3$ composites demonstrated significantly higher voltage responses compared to pure PVDF, confirming that the inclusion of $BaTiO_3$ nanoparticles enhances the piezoelectric behavior of the material. This setup and result can be better appreciated by understanding the fundamental principles of **piezoelectricity**, which refers to the property of certain materials to generate an electric charge when subjected to mechanical stress (direct effect), and conversely, to deform mechanically when an electric field is applied (inverse effect). Common piezoelectric materials include crystalline substances like quartz, ceramics such as $BaTiO_3$ and PZT, and polymers like PVDF. A **piezoelectric sensor** is a device that harnesses the direct piezoelectric effect to convert mechanical forces such as pressure, vibration, or strain into measurable electrical signals. When force is applied, the material inside the sensor deforms,

86

leading to a separation of charge and the generation of a voltage that can be detected using instruments like a DSO. In my project, the piezoelectric actuator acted as a mechanical driver, stimulating the composite samples, which then produced electrical signals proportional to the mechanical stress, thereby demonstrating their piezoelectric activity.

D. DC square wave perturbed by AC Signal Using Synchronized DC Bias Switching via Multiplexer-Controlled Analog Integration
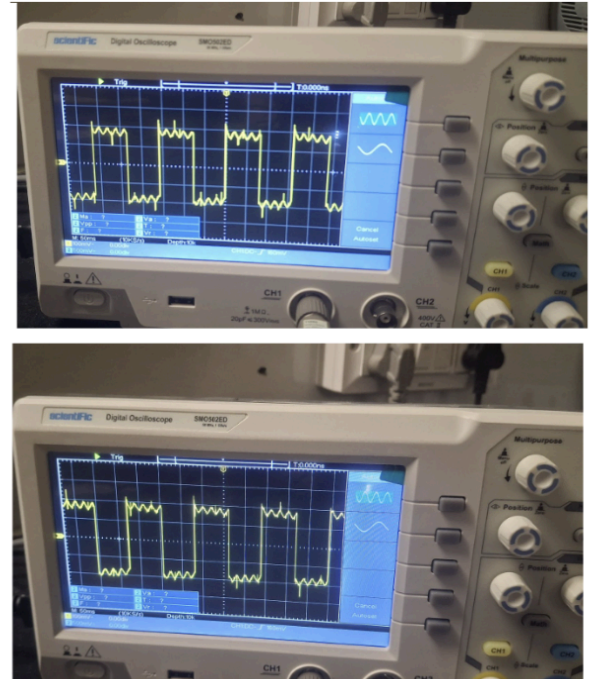
AC perturbed DC square wave
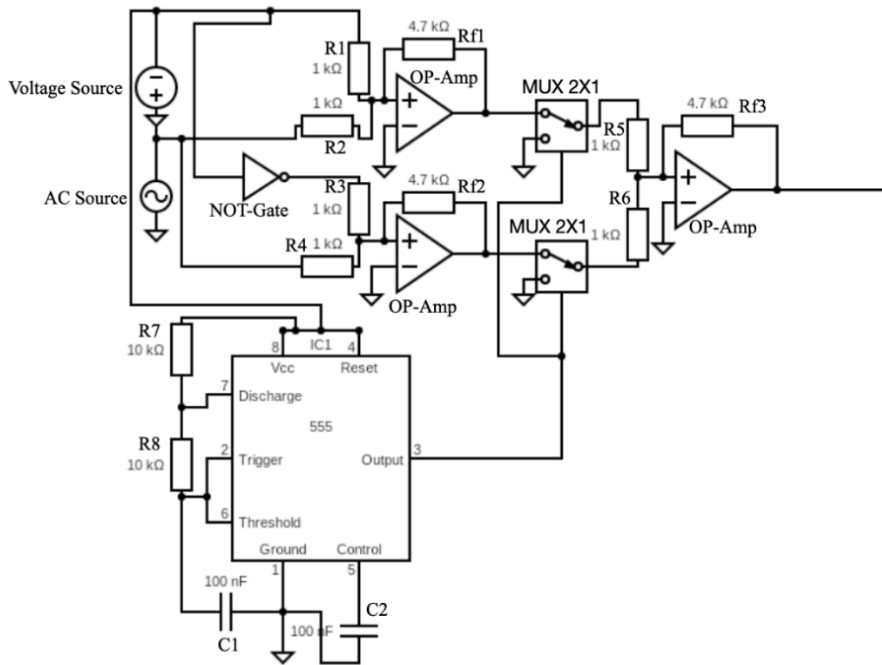
Fig 5.5 a)Circuit Diagram of AC Perturbed DC Square wave b)Output Waveform

In this experiment, a circuit was developed to perturb an AC signal within a DC square wave using a combination of digital and analog ICs: NOT gate (IC 7404), operational amplifiers (IC 741), 2×1 multiplexers (IC 74HC157), and a 555 timer. A positive DC voltage was sourced from a regulated supply, and its negative equivalent was generated using a NOT gate from IC 7404. The IC 7404 is a hex inverter containing six independent NOT gates, each outputting the logical complement of its input using internal transistor inverters. This inverted voltage was then used in conjunction with the original DC voltage.

Fig 5.6 a)Pin Diagram of IC741(OpAmp) b)Block diagram of 2x1 MUX c)Pin Diagram of IC74157

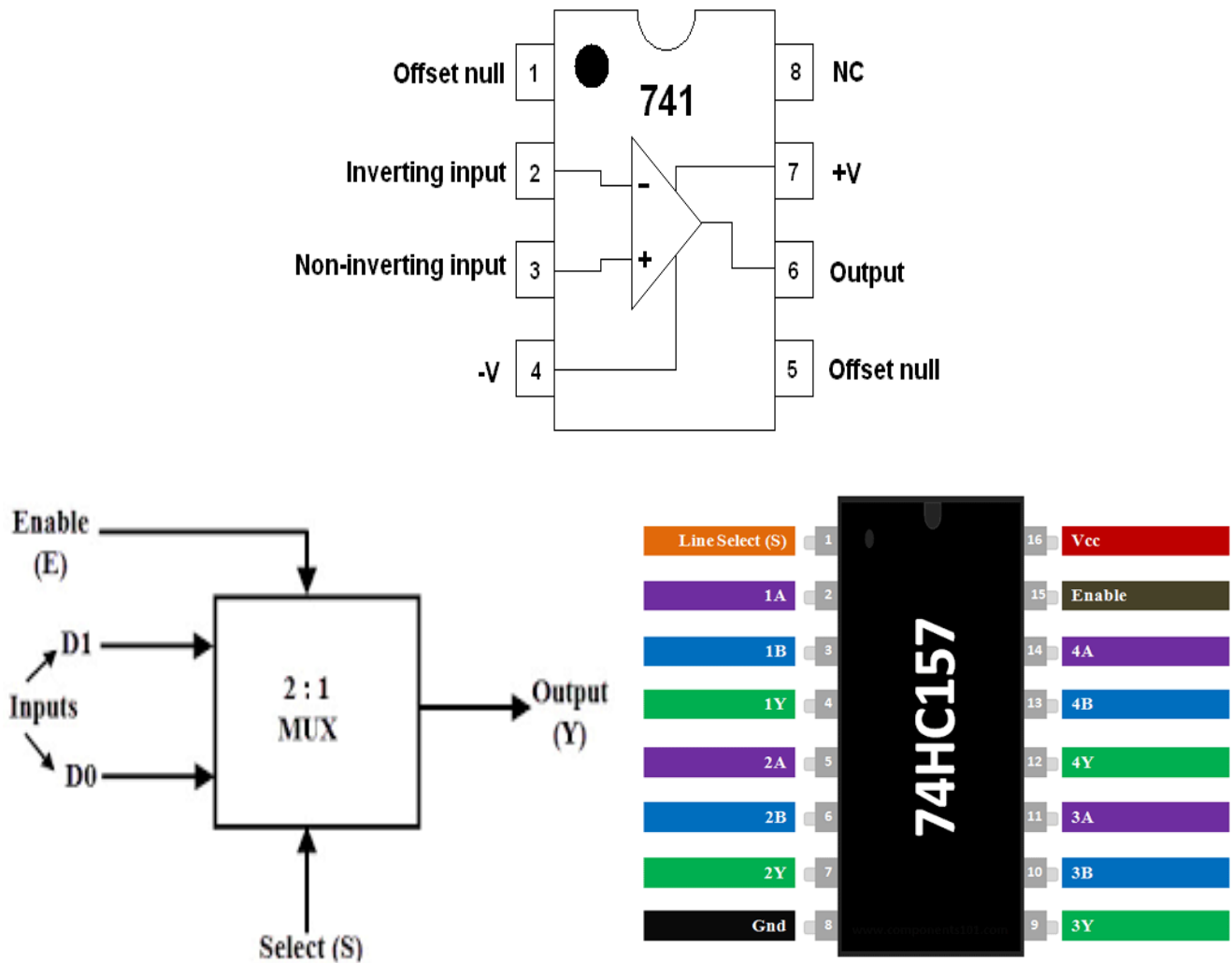Two operational amplifiers (IC 741) were used in adder configurations: one added the AC signal to the positive DC voltage, and the other added it to the negative DC voltage. The IC 741 is a general-purpose op-amp with a differential amplifier input stage, internal gain stages, and output buffer, capable of amplifying the voltage difference between its inputs with external resistor-based gain control. The resulting two signals (AC + +Vdc) and (AC + -Vdc) were fed into two separate 2×1 multiplexers (IC 74HC157). The IC 74HC157 is a quad 2×1 multiplexer in which each channel selects between two input lines (A and B) based on a select input (S) and an active-low enable line ($\overline{G}$), using internal transmission gates. The select lines of both multiplexers were connected to a square wave signal generated from a 555 timer configured in astable mode. A 555 timer in astable configuration is a self-oscillating circuit that uses two resistors (R1 and R2) and a capacitor (C1) connected between pins

89

6, 7, and 2. Capacitor C1 charges through both R1 and R2 and discharges through R2 alone via pin 7, causing the output on pin 3 to toggle continuously. The output frequency is given by ($f=1.44/((R1+2R2) \cdot C$).
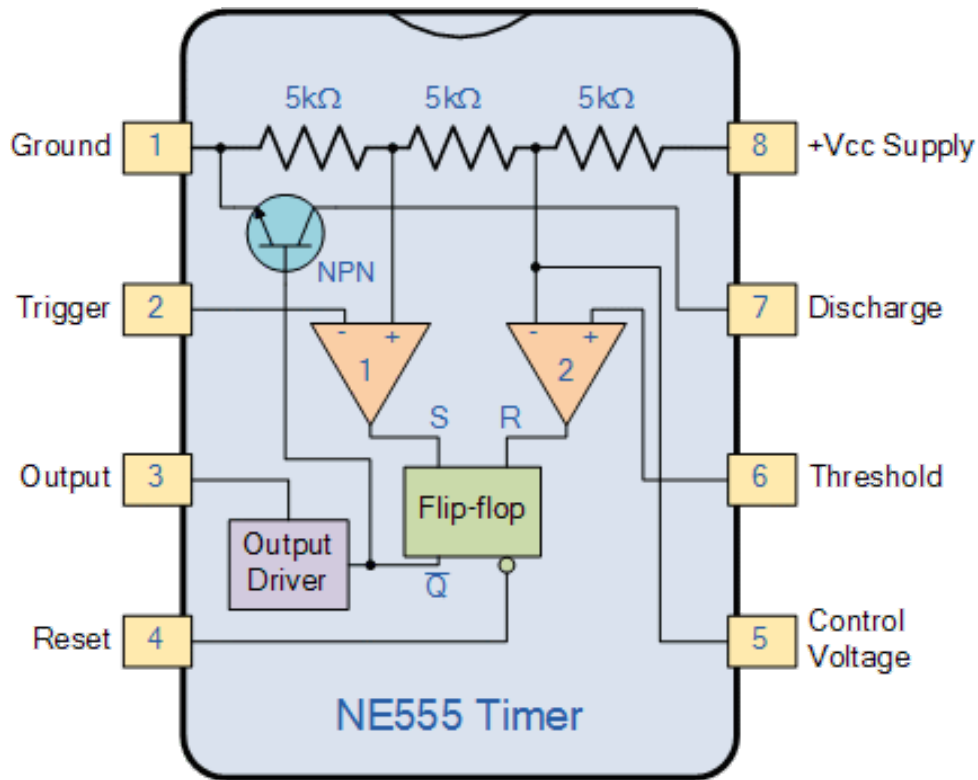
Fig 5.7 Functional Diagram of IC 555

with the duty cycle controlled by the resistor values. Internally, the 555 contains two comparators, an SR flip-flop, and a discharge transistor, along with a voltage divider that establishes reference levels at **($\frac{1}{3}$)V$_{cc}$=Lower threshold for the trigger comparator**

($\frac{2}{3}$)V$_{cc}$=Upper threshold for the trigger comparator

These determine the charging and discharging thresholds of the capacitor, allowing automatic oscillation between HIGH and LOW outputs. The outputs of both multiplexers were finally combined using another op-amp (IC 741) in adder mode, producing the final output waveform. This waveform represents an AC signal perturbed by a DC square wave, where the polarity of the DC bias alternates with the 555-generated timing, resulting in dynamic switching and modulation effectively demonstrating signal manipulation through synchronized analog and digital integration.

REFERENCES

1.	Perovskite (structure) - Wikipedia, https://en.wikipedia.org/wiki/Perovskite_(structure)

2.	An introduction to Perovskites, https://www.perovskite-info.com/introduction

3.	S. Piskunov a,*, E. Heifets b, R.I. Eglitis a, G. Borstel a,Computational Materials Science 29 (2004) 165–178 ,www.elsevier.com/locate/commatsci, "Bulk properties and electronic structure of SrTiO3, BaTiO3, PbTiO3 perovskites: an ab initio" HF/DFT study,doi:10.1016/j.commatsci.2003.08.036

4.	Annette Bussmann-Holdera,*, Krystian Rolederb, Jae-Hyeon Ko,Journal of Physics and Chemistry of Solids,journal homepage: www.elsevier.com/locate/jpcs,What makes the difference in perovskite titanates?

5.	M. A. Pen˜a and J. L. G. Fierro*,Chemical Reviews, 2001, Vol. 101, No. 7,Chemical Structures and Performance of Perovskite Oxides

6.	Juan-Pablo Correa-Baena,1,2* Michael Saliba,2 Tonio Buonassisi,1 Michael Grätzel,2 Antonio Abate,3 Wolfgang Tress,2 Anders Hagfeldt2 * ,Correa-Baena et al., Science 358, 739–744 (2017) , Promises and challenges of perovskite solar cells

Chuantian Zuo, Henk J. Bolink, Hongwei Han, Jinsong Huang, David Cahen, Liming Ding,www.advancedscience.comAdv. Sci. 2016, 3, 1500324,www.MaterialsViews.com Advances in Perovskite Solar Cells

7.	What are perovskite materials? - Articles & Publications - Blog - Quantum Solutions,, https://quantum-solutions.com/blog/what-are-perovskite-materials/

8.	Mats Johnsson a and Peter Lemmens b, Crystallography and Chemistry of Perovskites - arXivhttps://arxiv.org/pdf/cond-mat/0506606

9.	Balasubramanian Viswanathan,V Suryakumar,B Venugopal,Hariprasad NarayananPEROVSKITE MATERIALS-AN INTRODUCTION - ResearchGate, accessed April 16, 2025,https://www.researchgate.net/publication/370100194_PEROVSKITE_MATERIALS-AN_INTRODUCTION

10.	Perovskite Materials | For Perovskite Solar Cells - Ossila,https://www.ossila.com/collections/perovskite-materials

11.	Afnan Alhashmi 1, Mohammed Benali Kanoun 2, Souraya Goumri-Said3 ,Materials (Basel)*Machine Learning for Halide Perovskite Materials ABX3 (B = Pb, X = I, Br, Cl) Assessment of Structural Properties and Band Gap Engineering for Solar Energy - PMC - PubMed Central,, https://pmc.ncbi.nlm.nih.gov/articles/PMC10095675/

12.	S Pradhan1 , G S Roy2* ,Researcher 2013;5(3) http://www.sciencepub.net/researcher,Study the Crystal Structure and Phase Transition of BaTiO3 – A Pervoskite, https://www.sciencepub.net/researcher/research0503/010_16289research0503_63_67.pdf

13.	Yuanbing Mao1, Hongjun Zhou1, Stanislaus S. Wong1, 2,www.sigmaaldrich.com, ,https://www.sigmaaldrich.com/US/en/technical-documents/technical-article/materials-science-and-engineering/photovoltaics-and-solar-cells/synthesis-properties#:~:text=Perovskite%2Dphase%20metal%20oxides%20exhibit,%2C%20pyroelectric%2C%20and%20piezoelectric%20behavior.&text=Specifically%2C%20linear%20dielectric%20materials%20exhibit,a%20function%20of%20applied%20field.

14.	Yuanbing Mao1, Hongjun Zhou1, Stanislaus S. Wong1, 2,Synthesis, Properties, and Applications of Perovskite-Phase Metal Oxide Nanostructures, accessed https://www.sigmaaldrich.com/US/en/technical-documents/technical-article/materials-science-and-engineering/photovoltaics-and-solar-cells/synthesis-properties

15.	Sushmita Gupta1*,SamarveerSingh1, Ritu Rani Chaudhary 2, DeepShikha 1and Vikky,Singh ,international Journal of Mechanical Engineering.,Review: Perovskite Materials, Properties, and their Multifunctional Applications, https://www.researchgate.net/publication/362347600_Review_Perovskite_Materials_Properties_and_their_Multifunctional_Applications

16.	 Faouzia Tayari,Silvia Soreto Teixeira,Manuel Pedro F. Graca andKais Iben Nassar,Inorganics, 2025,A Comprehensive Review of Recent Advances in Perovskite Materials: Electrical, Dielectric, and Magnetic Properties - MDPI, https://www.mdpi.com/2304-6740/13/3/67

17.	Optical properties of two-dimensional perovskites - Frontiers Journals of Higher Education Press,https://journal.hep.com.cn/fop/EN/10.1007/s11467-023-1256-8

18.	Eman Abdul Rahman Assirey "Perovskite synthesis, properties and their related biochemical and biomedical applications," *Biomed. Res. Int.*, vol. 2019, Article ID 3410872, 2019. [Online]. Available: https://pmc.ncbi.nlm.nih.gov/articles/PMC6733782/

19.	The Essential Guide to Understanding Barium Titanate and Its ..., https://www.preciseceramic.com/blog/the-essential-guide-to-understanding-barium-titanate-and-its-applications.html

20.	Barium titanate - Wikipedia,https://en.wikipedia.org/wiki/Barium_titanate

21.	Burcu Ertuğ1,American Journal of Engineering Research (AJER),The Overview of The Electrical Properties of Barium Titanate - ajer.org 2025, https://www.ajer.org/papers/v2(8)/A0280107.pdf

22.	S. A. LOKARE,International Journal of Chemical and Physical Sciences, ISSN:2319-6602 IJCPS Vol. 4 Special Issue ETP – 2015 www.ijcps.org ,Structural and Electrical Properties of BaTiO3 prepared by Solid State Route - International Journal of Chemical and Physical Sciences,https://www.ijcps.org/0Site/SP5/P25.pdf

23.	Rakesh A. andDiego Pugliese 2,. (2025). Innovations in perovskite solar cell technology. *Micromachines*, *15*(2), 192. https://doi.org/10.3390/mi15020192

24.	Christian Ludt 1,2,*Dirk C. Meyer 1,2 andMatthias Zschornak 1,2,3. Development of lead-free perovskite materials. *Materials*, *17*(5), 1023. https://doi.org/10.3390/ma17051023

25.	S. Ram; A. Jana; T. K. Kundu,J. Appl. Phys. 102, 054107 (2007),© 2007 American Institute of Physics,Ferroelectric BaTiO3 phase of orthorhombic crystal structure contained in nanoparticles - AIP Publishing, accessed April 16, 2025, https://pubs.aip.org/aip/jap/article-pdf/doi/10.1063/1.2759865/14072753/054107_1_online.pdf © 2007 American Institute of Physics

26.	Balasubramanian Viswanathan,V Suryakumar,B Venugopal,Hariprasad Narayanan Perovskite materials: An introduction. *ResearchGate*. https://www.researchgate.net/publication/370100194_PEROVSKITE_MATERIALS-AN_INTRODUCTION

27.	A. W. Hewat,Gordon and Breach Science Publishers Ltd. ,Ferroelectrics 1974,Vol. 6, pp.

215-218 Structure of rhombohedral ferroelectric barium titanate - Taylor & Francis Online,, https://www.tandfonline.com/doi/abs/10.1080/00150197408243970

28.   Jinghui Gao1,*ID , Dezhen Xue1, Wenfeng Liu1,Chao Zhou1and Xiaobing Ren1,2,* www.researchgate.net, Recent Progress on BaTiO3-Based Piezoelectric Ceramics for Actuator Applicationshttps://www.researchgate.net/figure/Piezoelectric-coefficients-for-BaTiO3-single-crystal-a nd-ceramic_tbl2_318814857#:~:text=View-,...,coefficient%20of%20191%20pC%2FN.

29.   Hiroshi Maiwa,Journal of the Ceramic Society of Japan 121 [8] 655-658 2013,Research gate, Piezoelectric properties of BaTiO3 ceramics prepared by hot isostatic pressing, https://www.researchgate.net/publication/259764426_Piezoelectric_properties_of_BaTiO3_ceramics_p repared_by_hot_isostatic_pressing

30.   Jinghui Gao 1,*,Dezhen Xue 1,*Actuators*,Wenfeng Liu 1,Chao Zhou 1 andXiaobing Ren 1,2,*Recent Progress on BaTiO3-Based Piezoelectric Ceramics for...https://www.mdpi.com/2076-0825/6/3/24

31.   M. Acosta ; N. Novak; V. Rojas; S. Patel; R. Vaish; J. Koruza ; G. A. Rossetti, Jr.; J. Rödel ,*Appl. Phys. Rev.* 4, 041305 (2017),BaTiO3-based piezoelectrics: Fundamentals, current status, and ..., https://pubs.aip.org/aip/apr/article/4/4/041305/123894/BaTiO3-based-piezoelectrics-Fundamentals-curr ent https://doi.org/10.1063/1.4990046

32.   Caozhuang Deng,Yi Zhang,Dan Yang,Advanced Sensor Research,Recent Progress on Barium Titanate‑Based Ferroelectrics for ...,https://www.researchgate.net/publication/378286303_Recent_Progress_on_Barium_Titanate-Based_ Ferroelectrics_for_Sensor_Applications

33.   X-ray Powder Diffraction (XRD) - SERC, https://serc.carleton.edu/msu_nanotech/methods/XRD.html

34.   X-ray Diffraction (XRD), https://web.pdx.edu/~pmoeck/phy381/Topic5a-XRD.pdf

35.   A. S. Bhalla *et al.*, "Bandgap Narrowing of BaTiO₃-Based Ferroelectric Oxides," *Nanomaterials*, vol. 13, no. 1, p. 115, Jan. 2023. [Online]. Available: https://pmc.ncbi.nlm.nih.gov/articles/PMC10745005/

36.   S. K. Jha *et al.*, "Effect of Cobalt Substitution on BaTiO₃," *ResearchGate*, [Online]. Available: https://www.researchgate.net/publication/282122398_Effect_of_Cobalt_Substitution_on_the_Structure _and_Dielectric_Properties_of_BaTiO3_Ceramics

37.   A. Shrivastava and S. Thakur, "Synthesis and Structural Analysis of Co-doped BaTiO₃," *ResearchGate*, [Online]. Available: https://www.researchgate.net/publication/281874818_Synthesis_and_structural_analysis_of_Co-doped _BaTiO3

38.   S. Hussain *et al.*, "Cr-Doped BaTiO₃ Nanocatalysts for Photocatalytic Hydrogen Production," *Inorg. Chem.*, vol. 55, no. 7, pp. 3404–3412, 2016. [Online]. Available: https://pubs.acs.org/doi/10.1021/acs.inorgchem.6b00240

39.   A. R. Tripathi and M. S. Chauhan, "Examination of the Influence of Cobalt Substitution on BaTiO₃," *ResearchGate*, [Online]. Available: https://www.researchgate.net/publication/356002623_Examination_of_the_Influence_of_Cobalt_Subst

itution_on_the_Structure_and_Dielectric_Properties_of_BaTiO3

40.	A. S. Ramanujam and R. K. Sahu, "Phase Segregation in BaTiO$_3$ Using Rietveld Refinement," *AIP Conf. Proc.*, vol. 1953, no. 1, p. 030179, 2018. https://colab.ws/articles/10.1063%2F1.5032632

41.	X-Ray Diffraction Basics | Chemical Instrumentation Facility - Iowa StateUniversity,https://www.cif.iastate.edu/services/acide/xrd-tutorial/xrd

42.	I. R. Lewis and H. G. M. Edwards, "Raman spectroscopy in art and archaeology," *Philos. Trans. R. Soc. A Math. Phys. Eng. Sci.*, vol. 374, no. 2080, p. 20160078, Nov. 2016. https://pmc.ncbi.nlm.nih.gov/articles/PMC5095529/

43.	C. R. Yuen, M. S. Smith, and D. Pestov, "Coherent anti-Stokes Raman spectroscopy (CARS)," *Commun. Biol.*, vol. 5, no. 1, pp. 1–10, Oct. 2022. https://pmc.ncbi.nlm.nih.gov/articles/PMC9484306/

44.	R. W. Egan, M. W. Lee, and J.-X. Cheng, "Quantitative, Comparable Coherent Anti-Stokes Raman Scattering," *Sci. Rep.*, vol. 7, no. 1, Aug. 2017. https://pmc.ncbi.nlm.nih.gov/articles/PMC5557306/

45.	A. K. Sahoo and M. S. Dresselhaus, "Quantum Mechanical Description of Raman Scattering," *ACS Nano*, vol. 10, no. 9, pp. 8376–8384, 2016. https://pubs.acs.org/doi/10.1021/acsnano.6b02484

46.	Y. Luo *et al.*, "Digital colloid-enhanced Raman spectroscopy," *Chem. Sci.*, 2024. https://pubs.rsc.org/en/content/articlelanding/2024/sc/d4sc02553a

47.	K. Kneipp, Y. Wang, H. Kneipp, L. T. Perelman, I. Itzkan, R. R. Dasari, and M. S. Feld, "Surface-enhanced Raman spectroscopy," *Chem. Soc. Rev.*, 2025. https://pubs.rsc.org/en/content/articlelanding/2025/cs/d4cs00883a

48.	A. Campion and P. Kambhampati, "Quantitative analytical surface-enhanced Raman spectroscopy," *Chem. Soc. Rev.*, 2025. https://pubs.rsc.org/en/content/articlelanding/2025/cs/d4cs00861h

49.	D. Zhang *et al.*, "Raman Spectroscopy for Chemical Biology Research," *J. Am. Chem. Soc.*, vol. 144, no. 35, pp. 15969–15986, 2022. https://pubs.acs.org/doi/10.1021/jacs.2c05359

50.	M. R. Otto, C. B. Mendel, and T. B. Huffman, "Electronic-Resonance CARS," *ACS Photonics*, vol. 11, no. 1, pp. 103–112, 2024. https://pubs.acs.org/doi/10.1021/acsphotonics.4c01187

51.	S. Suzuki, "Kramers-Heisenberg formula for Rayleigh and Raman Scattering," https://bingweb.binghamton.edu/~suzuki/QM_Graduate/Kramers-Heisenberg_formula_for_Rayleigh_and_Raman.pdf

52.	Z. Hyamani, "Classical Theory of Rayleigh and Raman Scattering," KFUPM Lecture Note. https://faculty.kfupm.edu.sa/phys/zhyamani/teaching/Coupled_Oscillations/lectures/lecture_8/Raman%20study%20material/Classical-Theory-of-Rayleigh-and-Raman-Scattering-18p.pdf

53.	Japan Science and Technology Agency, "1-nm resolution Raman microscopy: A world first," Press Release, 2022. https://www.jst.go.jp/pr/info/info1386/index_e.html

54.	HORIBA Scientific, "Practical Group Theory and Raman Spectroscopy – Part I," https://www.horiba.com/fileadmin/uploads/Scientific/Documents/Raman/Specy_Workbench-DT-Practical_Group_Theory__Raman_Spectroscopy-part_1.pdf

55.	T. R. Cundari, "Understanding Raman Spectroscopy," University of Toronto Scarborough,: https://www.utsc.utoronto.ca/~traceslab/PDFs/raman_understanding.pdf

56.	M. Diem, "Raman Crystallography and the Effect of Raman Polarizability Tensor Element Values," *Spectroscopy* https://www.spectroscopyonline.com/view/raman-crystallography-and-the-effect-of-raman-polarizabilit

y-tensor-element-values
57.   "Raman   Thermometry,"   *Spectroscopy* https://www.spectroscopyonline.com/view/raman-thermometry

58.   Nicolet   CZ,   "Fundamentals   of   Raman   Polarization   Microscopy," https://nicoletcz.cz/app/uploads/2021/08/7b72326b.pdf

59.   G. Breit and E. Teller, "Intensity and Maxwell-Boltzmann Distribution," *Phys. Rev.*, vol. 34, no. 5, pp. 720–730, 1929. [Online]. Available: https://link.aps.org/doi/10.1103/PhysRev.34.720

60.   "Lecture   Note   –   Docenti.unina.it,": https://www.docenti.unina.it/webdocenti-be/allegati/materiale-didattico/471485

61. A. Alyamani and O. M. Lemine,FE-SEM Characterization of Some Nanomaterial,DOI: 10.5772/34361

62. P. Gnanamoorthy • V. Karthikeyan • V. Ashok Prabu,J Porous Mater (2014) 21:225–233, springer,Field Emission Scanning Electron Microscopy (FESEM) characterisation of the porous silica nanoparticulate structure of marine diatomsDOI 10.1007/s10934-013-9767-2

63. Xianming Shi a,b, *, Laura Fay a , Marijean M. Peterson a , Michael Berry b , Matthew Mooney b,Construction and Building Material,journal homepage: www.elsevier.com/locate/conbuildmat,A FESEM/EDX investigation into how continuous deicer exposure affects the chemistry of Portland cement concrete,doi:10.1016/j.conbuildmat.2010.06.086

64. M. Abd Mutalib, M.A. Rahman, M.H.D. Othman, A.F. Ismail, J. Jaafar,Membrane Characterization,elsevier,Scanning Electron Microscopy (SEM) and Energy-Dispersive X-Ray (EDX) Spectroscopy,https://doi.org/10.1016/B978-0-444-63776-5.00009-7

65. Science direct,https://www.sciencedirect.com/topics/materials-science/field-emission-scanning-electron-micro scopy#:~:text=Field%20emission%20scanning%20electron%20microscopy%20(FESEM)%20is%20 used%20to%20study,electrons%20rather%20than%20light%20sources.

66. Bogdan Lewczuk 1,, Natalia Szyryńska,Field-Emission Scanning Electron Microscope as a Tool for Large-Area and Large-Volume Ultrastructural Studies 1https://pmc.ncbi.nlm.nih.gov/articles/PMC8698110/

67. B. C. Ang, I. I. Yaacob, Irwan Nurdin,Journal of nano material,Investigation of Fe2O3/SiO2 Nanocomposite by FESEM and TEM, https://doi.org/10.1155/2013/980390

68. Information on the FESEM (Field-emission Scanning Electron Microscope) Radboud University Nijmegen ,https://vcbio.science.ru.nl/public/pdf/fesem_info_eng.pdf

69. I.V. Blonskaya, N.S. Kirilkin, O.V. Kristavchuk, N.E. Lizunov, S.A. Mityukhin, O.L. Orlovich, O.A. Polezhaeva,elsevier,Nuclear Instruments and Methods in Physics Research Section B: Beam Interactions with Materials and AtomsVolume 542, September 2023, Pages 66-73, Visualization andcharacterization of ion latent tracks in semicrystalline polymers by FESEM,

70. KL Bunker, D McAllister, KA Allison, K Wagner, K Rickabaugh, AM Levine, BR Strohmeier, RJ Lee,Microsc Microanal 14(Suppl 2), 2008,TEM and FESEM: The Right Combination for Enhanced Particle Characterization,DOI: 10.1017/S1431927608083682

71. Overview of the FESEM system, https://www.iitk.ac.in/meesa/SEM/tutorial/SEM_MS.pdf

72. https://www.iitk.ac.in/meesa/SEM/SEM_manual.pdf

73. Cik Rohaida Che Hak1,Foo, C.T.1 Nor Azillah Fatimah Othman1,Field Emission Scanning Electron Microscope (FESEM) Facility in BTI,https://inis.iaea.org/records/46aek-2dr87

74. Dielectric - Wikipedia, https://en.wikipedia.org/wiki/Dielectric

75. Dielectric | Definition, Properties, & Polarization | Britannica https://www.britannica.com/science/dielectric

76. Basics of Measuring the Dielectric Properties of Materials https://www.cmc.ca/wp-content/uploads/2019/08/Basics_Of_MeasuringDielectrics_5989-2589EN.pdf

77. Dielectric Materials, https://www.doitpoms.ac.uk/tlplib/dielectrics/printall.php

78. John G. Kirkwood,J. Chem. Phys. 4, 592–601 (1936),AIP Publishing,On the Theory of Dielectric Polarization,https://doi.org/10.1063/1.1749911

79. Dielectric Material - Properties, Examples and Applications - ElProCus, https://www.elprocus.com/what-is-dielectric-material-properties-applications/

80. A. Schönhals & F. Kremer ,Chapter-3 pp 59–98 Analysis of Dielectric Spectra

81. A. K. Jonscher ,© *1977 Nature Publishing Group*,The 'universal' dielectric response,https://www.nature.com/articles/267673a0

82. Mechanisms of Polarization - Module 4: Dielectric Ceramics: Basic Principles Objectives_templatehttps://archive.nptel.ac.in/content/storage2/courses/113104005/lecture18a/18_2.htm

83. 6.1.1: Dielectric Polarization - Engineering LibreTexts, https://eng.libretexts.org/Workbench/Materials_Science_for_Electrical_Engineering/06%3A_Thermal_Optical/6.01%3A_Optical_Properties/6.1.01%3A_Dielectric_Polarization

84. Dielectric Constant and its Effects on the Properties of a Capacitor - https://passive-components.eu/the-dielectric-constant-and-its-effects-on-the-properties-of-a-capacitor/

85. Dielectric constant | Definition, Formula, Units, & Facts | Britannica, https://www.britannica.com/science/dielectric-constant

86. Bunget, I., & Popescu, M. (1984). *Physics of solid dielectrics*. Amsterdam: Elsevier.

87. Kao, K. (2004). *Dielectric phenomena in solids with emphasis on physical concepts of electronic processes*. Amsterdam: Academic Press.

88. Andrew K Jonscher,© 1999 IOP Publishing Ltd,J. Phys. D: Appl. Phys. 32 (1999) R57–R70. Printed in the UK,Dielectric relaxation in solids DOI 10.1088/0022-3727/32/14/201

89. S.J. Fiedziuszko; I.C. Hunter; T. Itoh; Y. Kobayashi; T. Nishikawa;, Publisher: IEEE ,IEEE TRANSACTIONS ON MICROWAVE THEORY AND TECHNIQUES

90. Dielectric strength | Principles of Physics ,,IIhttps://fiveable.me/principles-physics-ii/unit-3/dielectric-strength/study-guide/jEOQJBlCH56cWkbz

91. Willi Volksen†,Robert D. Miller†,Geraud Dubois*†‡,Low Dielectric Constant Materials, 2010 American Chemical SocietyPublished on Web 12/04/2009

92. 【Thorough Explanation】What are transmission loss, dielectric loss .., https://www.resonac.com/solution/tech/transmission-loss.html

93. Ahmed A. Al-Ghamdi1, Omar A. Al-Hartomy1, Falleh R. Al-Solamy2, Nikolay Dishovsky3*, Diana Zaimova3,Materials Sciences and Applications, 2016, 7, 108-118 Published Online February 2016 in SciRes. http://www.scirp.org/journal/msa,Some Factors Influencing the Dielectric Properties of Natural Rubber Composites Containing Different Carbon Nanostructures - Scientific Research Publishing, accessed on April 13, 2025,

https://www.scirp.org/journal/paperinformation?paperid=64056 DOI: 10.4236/msa.2016.72011

94. Quan Wang 1,Junbo Che 1,Weifei Wu 1,Zhendong Hu 1,Xueqing Liu 2,Tianli Ren 3,Yuwei Chen 1,*Polymers* 2023, *15*(3), 590; https://doi.org/10.3390/polym15030590,Contributing Factors of Dielectric Properties for Polymer Matrix ..., accessed on April 13, 2025, https://www.mdpi.com/2073-4360/15/3/590

95. Kasap, S. (2006). *Principles of electronic materials and devices* (3rd ed.). Boston: McGraw-Hill.

96. Zulkifli Ahmad,Polymer Dielectric Materials,DOI: 10.5772/50638

97. sciencetech-inc.com, accessed on April 17, 2025, https://sciencetech-inc.com/page/i-v-measurement#:~:text=source%2Dmeasure%20unit%3F-,What%20is%20an%20I%2DV%20Measurement%3F,specific%20irradiance%20and%20temperature%20conditions.

98. IV Characterization https://www.tek.com/en/solutions/industry/power-semiconductor/iv-characterization

99. Current–voltage characteristichttps://en.wikipedia.org/wiki/Current%E2%80%93voltage_characteristic

100. Understanding Current-Voltage Curves - Technical Articles - All About Circuits, accessed on April 17, 2025, https://www.allaboutcircuits.com/technical-articles/understanding-i-v-curves-part-i/

101. Ohm's law https://en.wikipedia.org/wiki/Ohm%27s_law

102. Gustavo Mata Osoro a,b, Damien Bregirouxa,n, Mai Pham Thi c, Franck Levassort d Structural and piezoelectric properties evolution induced by Cobalt doping and Cobalt/niobium co-doping in BaTiO3 Materials Letters journal homepage: www.elsevier.com/locate/matlet

103. L. Padilla-Campos a, *, D.E. Diaz-Droguett b, R. Lavín c, e, S. Fuentes d, e, ** Synthesis and structural analysis of Co-doped BaTiO3 Journal of Molecular Structure journal homepage: http://www.elsevier.com/locate/molstruc

104. Rémy Ul,* Pascal Marchet, Mai Pham-Thi, and Louis-Pascal Tran-Huu-Hue Improved Properties of Doped BaTiO3 Piezoelectric Ceramics DOI: 10.1002/pssa.201900413

105. The-Long Phan; P. D. Thang; T. A. Ho; T. V. Manh; Tran Dang Thanh; V. D. Lam; N. T. Dang; S. C. Yu Local geometric and electronic structures and origin of magnetism in Co-doped BaTiO3 multiferroics JOURNAL OF APPLIED PHYSICS https://doi.org/10.1063/1.4907182

106. Yuan-Hua Lin; Songyin Zhang; Chaoyong Deng; Yi Zhang; Xiaohui Wang; Ce-Wen Nan Magnetic behavior and thickness dependence in Co-doped BaTiO3 thin films JOURNAL OF APPLIED PHYSICS

107. Dhiren K. Pradhan, *ab Hari Sankar Mohanty, ‡c Shalini Kumari, de Krishnamayee Bhoi,c Nan Tang,a Ravikant,§f M. M. Rahaman, g
Dillip K. Pradhan, c Ashok Kumar,f Dustin A. Gilbertah and Philip D. Rack *ab Ferroic phase transitions and magnetoelectric coupling in Cobalt doped BaTiO3 Journal of Materials Chemistry C This journal is © The Royal Society of Chemistry

108. H. Lemziouka, R. Moubah, F.Z. Rachid, Y. Jouane, E.K. Hlil, M. Abid, H. Lassri Extrinsic magnetism in Co-doped BaTiO3 powders prepared by sol-gel route Ceramics International http://dx.doi.org/10.1016/j.ceramint.2016.08.143 CERI13595

109. Shau-Wei Yu, Wang-Chi Vincent Yeh, Jya-Ler Jou & Chien-Ming Lei Synthesis and Characterization the Dielectric Properties of Cobalt Doping Hexagonal BaTiO3 https://doi.org/10.1080/00150193.2013.846190 Taylor & Francis Group

110.   D.I. Khomskii Multiferroics: Different ways to combine magnetism and ferroelectricity Journal of Magnetism and Magnetic Materials 306 www.elsevier.com/locate/jmmm

111.   Jae-Hyeon Cho and Wook Jo A Brief Review on Magnetoelectric Multiferroic Oxides DOI: https://doi.org/10.4313/JKEM.2021.34.3.149

112.   Manish Kumar1,* , S. Shankar1,2,3, Arvind Kumar1, Avneesh Anshul4, M. Jayasimhadri2, and O. P. Thakur3 Progress in multiferroic and magnetoelectric materials: applications, opportunities and challenges https://doi.org/10.1007/s10854-020-04574-2 Springer

113.   Irfan Hussain Lone1* , Jeenat Aslam1, Nagi R. E. Radwan1, Ali Habib Bashal2, Amin F. A. Ajlouni1 and Arifa Akhter3 Multiferroic ABO3 Transition Metal Oxides: a
Rare Interaction of Ferroelectricity and Magnetism ttps://doi.org/10.1186/s11671-019-2961-7 Nanoscale Research Letters Springer

114.   BAS B. VAN AKEN*1, THOMAS T. M. PALSTRA1, ALESSIO FILIPPETTI†2 AND NICOLA A. SPALDIN‡2 The origin of ferroelectricity in magnetoelectric YMnO3 doi:10.1038/nmat1080 ©2004 NaturePublishingGroup

115.   Burtrand Lee , Jianping Zhang Preparation, structure evolution and dielectric properties of BaTiO3 thin films and powders by an aqueous solgel process 0040-609001$ - see front matter 2001 Elsevier Science

116.   Baorang Li , Xiaohui Wang, Longtu Li Synthesis and sintering behavior of BaTiO prepared by different chemical method Materials Chemistry and Physics 78 (2002) 292–298 journal homepage: www.elsevier.com/locate/matlet

117.   Junsoo Shin; Amit Goyal; Stephen Jesse; Dae Ho Kim Single-crystal-like, -axis oriented thin films with high-performance on flexible metal templates for

118.   Junsoo Shin; Amit Goyal; Stephen Jesse; Dae Ho Kim ferroelectric applications APPLIED PHYSICS LETTERS https://doi.org/10.1063/1.3158955

119.   M.   Cernea   METHODSFORPREPARATIONOFBaTiO   THINFILMS   3   Journal   of Opotoelectronics and Advanced Materials Vol. 6, No. 4, December 2004, p. 1349 - 1356

120.   Detlev F. K. Hennings,* B. Seriyati Schreinemacher, and Herbert Schreinemacher Solid-State Preparation of BaTiO3-Based Dielectrics, Using Ultrafine Raw Materials *J. Am. Ceram. Soc.,* 84 [12] 2777–82 (2001)

121.   BY H. F. KAY Preparation and Properties of Crystals of Barium Titanate, BaTiO3 Avta Cryst. (1948)

122.   Xia Zhao, Wenfeng Liun, Wei Chen, Shengtao Li Preparation and properties of BaTiO3 ceramics from the ne ceramic powder CERAMICS INTERNATIONAL Published by Elsevier Ltd and Techna Group S.r.l.

123.   S.K. Das a,b, R.N. Mishra b, B.K. Roul a,n Magnetic and ferroelectric properties of Ni doped BaTiO3 Solid State Communications Published by Elsevier Ltd and Techna Group S.r.l.

124.   ANDRZEJKOLE˙ ZY´ NSKI AND KATARZYNATKACZ-´ SMIECH, "From the Molecular Picture to the Band Structure of Cubic and Tetragonal Barium Titanate".   DOI: 10.1080/00150190590926300

125.   Katarzyna Tkacz-S ´miech, Andrzej Kolez˙yn ´ski*, W.S. Ptak, Crystal-chemical aspects of phase transitions in barium titanate, PERGAMON. Solid State Communications 127 (2003) 557–562.